A Study on Spatial and Temporal Variabilities in the Martian Thermosphere

A thesis submitted to

Indian Institute of Space Science and Technology
Thiruvananthapuram, INDIA

in the partial fulfillment for the award of the degree of

Doctor of Philosophy

by

Neha Gupta

National Atmospheric Research Laboratory
Gadanki, INDIA

March, 2022

Certificate

This is to certify that the thesis titled ***A Study on Spatial and Temporal Variabilities in the Martian Thermosphere*** submitted by **Neha Gupta**, to the Indian Institute of Space Science and Technology, Thiruvananthapuram, in partial fulfillment for the award of the degree of **Doctor of Philosophy** is a bona fide record of the original work carried out by her under our supervision. The contents of this thesis, in full or in parts, have not been submitted to any other Institute or University for the award of any degree or diploma.

Narukull Venkateswara Rao
Scientist/Engineer-SE
Ionosphere and Space Physics Group
National Atmospheric Research Laboratory, Gadanki

Umesh R. Kadhane
Professor/Head
Department of Physics
Indian Institute of Space Science and Technology, Thiruvananthapuram

Place: Thiruvananthapuram
Date:

Declaration

I declare that this thesis titled ***A Study on Spatial and Temporal Variabilities in the Martian Thermosphere*** submitted in partial fulfillment for the award of the degree of **Doctor of Philosophy** is a record of the original work carried out by me under the supervision of Dr. **Narukull Venkateswara Rao** and Prof. **Umesh R. Kadhane**, and has not formed the basis for the award of any degree, diploma, associateship, fellowship, or other titles in this or any other Institution or University of higher learning. In keeping with the ethical practice in reporting scientific information, due acknowledgments have been made wherever the findings of others have been cited.

Place: Thiruvananthapuram
Date: March, 2022

Neha Gupta
(SC18D021)

To my family & women in science...

Acknowledgements

First, I wish to thank both my PhD supervisors, Dr. Narukull Venkateswara Rao at the National Atmospheric Research Laboratory (NARL), and Professor Umesh K. Kadhane at the Indian Institute of Space Science and Technology (IIST). Their tireless efforts and mutual understanding helped me navigate the choppy waters of a PhD involving two institutes located about 1000 kms apart. I owe my deepest gratitude to Dr. Narukull Venkateswara Rao for finding the time out for guiding me from his often-taxing responsibilities as a Scientists at NARL. I appreciate the pains he took to secure funding, to help with problem formulation and to always maintain a positive and patient attitude. His ability to maintain a healthy mix of hands-on intervention when its needed and a hands-off approach at other times has given me ample space to learn from his as well as express my own ideas. I found his passion for work and motivation contagious, and I could not have completed my PhD in time without his unwavering support throughout the time of the covid-19 pandemic.

I wish to express my sincere gratitude to my co-supervisor and doctoral committee chair, Professor Umesh k Kadhane who has always been a beacon of support and source of endless energy throughout my PhD. His unique ability to make students discover a spirit of adventure in pursuits of academic research helped me immensely to stay positive and excited in the midst of often grueling work. His crucial interventions by leveraging personal and professional connections in various ISRO centers has helped me cross what often felt like brick walls at the time. Without his guidance and persistent help this dissertation would not have materialized. I also would like to thank my dissertation committee members, Dr. Tarun Kumar Pant at Space Physics Laboratory (SPL), Professor C.S. Narayanamurthy, IIST and Dr. Sourin Mukhopadhyay, IIST for sharing knowledge, their comments and suggestions pertaining to my research work. A great deal of thanks also goes to all the past and present members of Planetary and Space science group at NARL- Mr. Yashwant, Scientist/Engineer-D, Leelavathi, Pavan D. Gramapurohit and Dr. Manasa for supporting me in academic matters as well as providing a supportive and friendly environment.

This dissertation would not have been possible without the financial support of the Department of Space, Government of India through the MOM AO Project. Many thanks to MENCA team members- Dr. Anil Bhardwaj at Physical Research Laboratory (PRL), Dr. Smitha V. Thampi, Dr. M.B. Dhanya, Dr. T.P Das, Dr. R. Satheesh Thampi and Mr.

Abhishek J. K. at Space Physics Laboratory (SPL) for helping with MENCA data analysis, a pivotal step in the project completion. I also sincerely thank Dr. Stephen Bougher at University of Michigan, and Dr. Meredith Elrod of GSFC, NASA for their timely support with Mars Global Ionosphere Thermosphere Model (MGITM).

I would also like to thank and acknowledge many current and past scholars from NARL and IIST that I have had the incredible joy and pleasure of working with over the course of my PhD.

Finally, it would be remiss of me if I did not thank my parents and my brother for putting up with an absentee daughter and sister during this process. My brother, Anshul Gupta has been unfailingly supportive and a well of infinite strength that I often draw from. Thank you all. ...

Neha Gupta

Abstract

The primary focus of the present thesis is to investigate and compare the local time, latitudinal, seasonal, and altitudinal variability of heavy (e.g., Ar, CO_2) and light mass species (e.g., He), in the Thermosphere of Mars. The work covered in this thesis starts with a study of the local time variations in heavier species like Ar and CO_2, using measurements from Neutral Gas Ion Mass Spectrometer (NGIMS) aboard the Mars Atmosphere and Volatile Evolution (MAVEN) spacecraft. The results show a persistent local time asymmetry in Ar densities and scale heights (temperatures), wherein the densities during the dusk hours are larger than those in the dawn hours at all altitudes. Ar being a heavy species and small in scale height is mostly affected by the dynamical heating and cooling of the atmosphere. Since the observations used in this study are from two different seasons, to validate these results, we further investigated the dawn-dusk asymmetry by using the measurements from same season. This constitutes the second study in this thesis. This was done using simultaneous measurements from Mars Exosphere Neutral Composition Analyser (MENCA) aboard the Mars Orbiter Mission (MOM) observing dusk side and NGIMS observing the dawn side of Mars. Moreover, these measurements fall during the growth phase of a Planet Encircling Dust Event (PEDE) in June 2018, which helped us to understand the effect of lower atmospheric processes on the steady-state of the upper atmosphere and hence the coupling between the lower and upper atmosphere. The results of the study show that not only do the dawn-dusk asymmetries persist in the same season, but they are enhanced due the radiative heating in the lower atmosphere and by the subsequent expansion of the thermosphere associated with the PEDE–2018.

In the third work, we focus on understanding the spatial and temporal distribution of the lighter species in the Mars thermosphere, using Helium (He) measurements from NGIMS. The accumulation of He in nightside winter polar and the equinoctial southern high latitude regions indicates that the lighter species are primarily controlled by the global circulation at the thermospheric altitudes on Mars. A comparative picture of spatial and temporal variations in different mass species is further presented in the fourth work, where diurnal and latitudinal variations in the mixing ratio of He, N_2, Ar with respect to the dominant species (i.e., CO_2) are studied. In addition, we investigated the response of mixing ratios to the dust storm season of MY 33 and 34 (PEDE-2018). During PEDE-2018, mixing

ratios show strong depletion compared to the dust storm season of MY 33. In addition, the variability in mixing ratios shows an anti-correlation with the trend in CDOD. The depletion factor is found to vary with the varying masses of mixing ratios. While on the day side variability in mixing ratios seems to be controlled by the seasonal variation in homopause altitude, a weak correlation on night side suggests the contribution of different processes. Changes in the atmospheric circulation during dust storm season combined with mass-dependent behavior of thermospheric species are most likely to affect the nightside variability of Mars.

Contents

List of Figures **xv**

List of Tables **xxiii**

1 Introduction to Mars atmosphere **1**

1.1 A Brief Introduction to Mars 1
1.2 Seasons on Mars 4
1.3 Atmosphere of Mars 5
1.4 Dynamics 11
1.4.1 Gravity Waves 11
1.4.2 Circulation 13
1.5 Seasonal Cycles 14
1.5.1 CO_2 cycle 14
1.5.2 Dust cycle 16
1.6 Thermosphere of Mars 17
1.6.1 Thermal structure 18
1.6.2 Vertical structure 18
1.6.3 Thermospheric variabilities 19
1.7 Motivation for this Thesis 22
1.8 Outline of This Dessertation 23

2 Instruments, Data and Methodology **25**

2.1 Introduction 25
2.2 Mars Missions 27
2.2.1 MAVEN 27
2.2.2 MOM 29
2.3 Instruments 29

2.3.1 NGIMS . . . 29
2.3.2 MENCA . . . 31
2.4 Observations from NGIMS and MENCA . . . 32
2.5 Parameter extraction from NGIMS . . . 33
2.5.1 Derivation of scale heights and temperatures . . . 33
2.5.2 Derivation of Homopause altitudes . . . 34
2.6 Data retrieval from MENCA . . . 34
2.7 Mars Global Ionosphere Thermosphere Model (M-GITM) . . . 38
2.8 Solar and Dust Indices . . . 40
2.9 Uncertainity and Errors . . . 41

3 Dawn-Dusk Asymmetries in the Martian Upper Atmosphere 42
3.1 Background . . . 42
3.2 Data . . . 43
3.3 Results . . . 44
3.3.1 Mass dependent variability . . . 44
3.3.2 Local time Vs altitude variability . . . 45
3.3.3 Diurnal variation . . . 46
3.3.4 Seasonal and Latitudinal variability . . . 49
3.3.5 Scale Heights and Temperatures variability . . . 51
3.4 Discussion . . . 53

4 Enhanced densities in the Martian thermosphere associated with the 2018 planet encircling dust event: Results from MENCA/ MOM and NGIMS/ MAVEN 58
4.1 Background . . . 59
4.2 MENCA and NGIMS measurements . . . 59
4.3 Results . . . 60
4.3.1 Altitude variation of Ar densities . . . 60
4.3.2 Seasonal and Local time variability . . . 63
4.3.3 Role of Global Dust Storm (PEDE-2018) . . . 64
4.3.4 O/CO_2 . . . 68
4.4 Discussion . . . 69

5 Latitudinal and Seasonal Asymmetries of the Helium Bulge in the Martian Upper Atmosphere **73**
5.1 Background . . . 74
5.2 He densities from observations and model . . . 75
5.3 Results . . . 76
5.3.1 Local time and latitude variability . . . 77
5.3.2 Comparison of observations with model outputs . . . 79
5.4 Discussion . . . 80

6 Local time and Latitudinal variation of Mixing Ratios in the Martian Upper Atmosphere **85**
6.1 Abstract . . . 85
6.2 Background . . . 86
6.3 Results . . . 87
6.3.1 Seasonal Vs Local time variability . . . 87
6.3.2 Local time Vs latitude variability . . . 89
6.3.3 Dust Storm induced variability . . . 90
6.4 Discussion . . . 92

7 Summary, Conclusions and Implications **97**

Bibliography **100**

List of Publications **131**

List of Figures

1.1 a) Olympus Mons' 3D view derived from Mars Orbiter Laser Altimeter's (MOLA) topographic data superimposed with the Mars Orbiter Camera' (MOC) wide-angle image mosaic, b) Valles Marineris, seen at an angle of 45° from Mars Express (ESA, 2009), and c) Hellas basin as seen by Exomars Trace Gas Orbitor's Colour and Stereo Surface Imaging System, CaSSIS on 29 May 2018 4

1.2 Map of surface topography of Mars as observed by MGS-MOLA. The elevation of topography is presented by the color scale. (Courtesy: NASA) . . 5

1.3 Schematic of seasons on Mars. Dashed lines represent the perihelion and aphelion approaches of Mars to the Sun. Solid radial lines represent the beginning of each "month". Color coding indicates surface temperature in each season and the local time shown for each image (indicating which portion of the planet is facing the Sun in each position). From http://www-mars.lmd.jussieu.fr/ mars/time/solar_longitude-html 6

1.4 Variation in atmospheric pressure with seasons on Mars, as measured by Viking Lander 1 (green colors), Viking Lander 2 (gray colors), Mars Pathfinder (black), Mars Phoenix Lander (purple), and Mars Science Laboratory (red/orange colors). This figure is: modified from Figure 3 of [1] . . 7

1.5 A comparison of the vertical structure of the atmosphere of Mars and Earth from [2] 10

1.6 Images of the CO_2 ice Cap in the Northern Polar region, captured by the Hubble Space Tele scope. This Figure shows sublimation of CO_2 Ice as the season changes from winter (far left) to northern spring (far right). Image credit: Phil James, Todd Clancy, Steve Lee, and NASA (http://hubblesite.org/gallery/album/entire/pr1997015b/) 15

1.7 (left) Temperature profiles of Mars upper atmosphere using Ar (blue), N_2 (green) measurements from NGIM and modeled using M-GITM simulations (Red) [3]. (Right) Density profiles of atmospheric neutrals as observed by NGIMS [4] 19

1.8 Latitude versus Longitude/local time variation of a) Temperature, b) Zonal Winds, c) [O] and d) [CO_2], at 200km, for Ls = 180 [5] 20

2.1 Schematic block diagram of a mass spectrometer (top) and a sample mass spectrum (bottom) generated during lab calibrations of MENCA 26

2.2 Location of Instruments on the MAVEN Spacecraft and Articulated Payload Platform (APP) [6] 27

2.3 Schematic of sampling process of NGIMS [7] 31

2.4 Altitude profiles of N_2 (left), Ar (middle) and CO_2 (right). The blue dots represents the densities measured by NGIMS and black lines represents the linear fit to the densities. 33

2.5 Represents the methodology followed to derive the homopause altitudes. Here, the red dots represent the altitude variation of N_2/Ar ratio and black line represents the linear fit to the ratio which is extrapolated towards the lower altitudes. Blue dashed lines mark the value where N_2/Ar = 1. Pink line represents the derived Exobase altitude and green line is shown to represent the derived homopause altitude derived by taking the crossing point of N_2/Ar=1 and linear fitted line. The data presented in the Figure corresponds to the MAVEN orbit number #713 35

2.6 Raw Spectrum obtained by MENCA on 05 June, 2018 for the mass range of 33 amu – 42 amu, at ˜165 km 36

2.7 (top) An example of the mass spectrum observed by MENCA on 05 June 2018 that shows all important neutral species between 1-50 amu. (bottom) Same as above, but shown only for amu between 33 and 42 to highlight Ar peak (amu 40). 37

2.8 (top) Temporal variation of the partial pressure of Ar observed by MENCA on 05 June 2015 (Ls=187.8º). The time in the x-axis is given in hours with respect to the time of periapsis crossing. The grey circles represent the amu 40 spectral data points. The red stars represent the data points after a smoothing using a 5-point running average. The dashed black lines represent the mean background levels in the inbound and outbound legs and the dashed blue lines represent the 2σ standard deviation of the original background data points of the inbound segment. 38

3.1 Latitude, SZA, Ls, and local time distribution of the NGIMS data coverage between periapsis and 300 km. The distributions are shown between (a) latitude and Ls, (b) local solar time and Ls, (c) latitude and local solar time, and (d) SZA and altitude. The three colors correspond to MY 32, MY 33, and MY 34. 44

3.2 a) F10.7 solar flux output corrected for martian orbit. (bottom) solar irradiance measurements from EUVM/MAVEN for spectral band b) 0.1-7 nm c) 17-22 nm d) Lyman-α 45

3.3 Variability of (a) CO_2, (b) Ar, (c) O, and (d) He densities as a function of SZA and altitude. These Figures were constructed using all of the data shown in Figure 3.1, which cover several latitudes, longitudes, and Ls values. The densities are averaged over a grid of 5° SZA $\times$ 5 km altitude. . . . 46

3.4 Local time and altitude variation of the mean Ar densities for MY 33. The mean densities were calculated by averaging all of the data in a 1-hr local time and 5-km altitude grid. 47

3.5 Local time variation of the Ar densities for (a) 160 km, (b) 200 km, and (c) 240 km for MY 33. The top panels display the original densities (open circles with blue lines) and a quadratic fit (black lines). The bottom panels show the residual densities obtained after the quadratic fit is removed from the original densities. 48

3.6 Mean and 1σ standard deviation of the Ar densities for the dawn side (midnight to noon through the morning terminator; shown for 0–12 hr on the bottom of each panel) and duskside (midnight to noon through the evening terminator; shown for 24–14 hr on the top of each panel) at three different altitudes for MY 33. 49

3.7 Altitude and local time variation of the ratios of the dusk to dawn densities at conjugate local times for MY 33. 50
3.8 Altitude and local time variations of the Ar densities for the NH (left panels) and SH (right panels). The top panels represent the variation over an Ls range of 90°–160°, and the bottom panels represent the variations for 210°–300° Ls. 51
3.9 (a) Latitude and local time variations of the Ar densities for 160 km. All of the data shown in Figure 3.1 were used to construct this Figure. (b) Ls and local time variation of the Ar densities at 160 km for (left to right) MY32, MY33, and MY34. 52
3.10 SZA variation of the Ar (top panel) scale heights and (bottom panel) temperatures for (blue closed circles) MY 32, (red stars) MY 33, and (black open circles) MY 34. 53
3.11 Local time and Ls variation in Ar (a) scale heights and (b) temperatures for (left to right) MY 32, MY 33, and MY 34. 54
3.12 Local time variation of the O/CO_2 ratio for (top to bottom) 170, 165, 160, and 155 km, based on observations for MY 33. 56

4.1 MAVEN (closed circles) and MOM (crosses) "along-track" (a) latitude versus longitude and (b) latitude versus local solar time coverage of the inbound trajectories. The inbound trajectories start at an altitude of 220 km at north-of/near the equator and their periapses end at south of the equator. . 60
4.2 Altitude profiles of Ar densities measured by (open circles) MENCA/MOM and (closed circles) NGIMS/MAVEN on (a-f) 05, 08, 10, 13, 16 and 29 June, 2018. The NGIMS observations for each day are color coded. Note that on each day MOM has only one inbound segment and hence the orbit numbers are not provided. 61
4.3 Altitude profiles of Ar densities observed in the inbound segments on 05 June 2018 by (a) MENCA and (b) NGIMS. The open black circles represent the original data points and the red closed circles represent the points with 5 km resolution. The 5 km resolution points for MENCA observations are obtained by linear interpolation and for NGIMS by averaging within 5 km altitude range. 62
4.4 Mean and standard deviation of Ar density profiles measured by (red) NGIMS/MAVEN and (blue) MENCA/MOM. 63

4.5 Solar longitude versus local solar time variations of Ar (a) densities at 170 km, (b) scale heights below the exobase, and (c) scale height temperatures measured by NGIMS and MENCA in MY34. Horizontal arrows in all panels point to the MENCA observations. 66

4.6 Solar longitude (Ls) variation of Ar densities at 170 km measured by (a) NGIMS/MAVEN and (b) MENCA/MOM spacecraft. In panel 'a', the dots represent the individual measurements and the solid line represents the ten-orbit smoothing average. Dashed red line in panels 'a' and 'b' represent the SZA (mentioned on the right ordinate). (c) Ls variation of CDOD at 610 Pa. Vertical line at the bottom panel indicates the time of onset of the PEDE-2018. 67

4.7 SZA variation of the (blue squares) seasonal mean and (closed red circles) PEDE-2018 Ar densities for 170 km observed (a) on the dawn side, and (b) on the dusk side. Note that the dates of MENCA measurements are also shown. The seasonal mean is computed by averaging the densities measured in MY 33 and those measured between Ls=0° and Ls=120° in MY 34. 68

4.8 Solar longitude (Ls) variation of residual Ar densities at 170 km measured by (a) NGIMS/MAVEN and (b) MENCA/MOM spacecraft. The residual densities are obtained by removing the seasonal mean densities at each SZA from those measured during PEDE-2018. The dotted grey lines represent the dates when MENCA measurements were made. (c) Ls variation of CDOD at 610 Pa. Vertical line at the bottom panel indicates the time of onset of the PEDE-2018. 69

4.9 Ratios between O and CO_2 densities (a) on the dawn side measured by NGIMS/MAVEN and (b) at the dusk terminator measured by MENCA/MOM on 05, 08, 10, 13, 16 and 29 June 2018. The dotted vertical line in the left panel is plotted where the O/CO_2 ratio is one. 70

5.1 Local Solar Time (LST) versus altitude variability of (top panels) He densities and (bottom panels) He/CO_2 ratios during (a) MY 33, (b) MY 34, (c) MY 35 and (d) Average of MY 32 – 35. The data are averaged within an altitude and local time grid of 5 km × 0.33 hr. 76

5.2 Temporal (as a function of Solar Longitude (Ls)) variation of (a) He/CO_2 ratios, (b) He density and (c) MAVEN latitude, for 200 km and color coded according to the season. Each season covers ±45° Ls. Bottom panel is color coded according to the LST. In the top panel, horizontal red dashed lines are drawn to highlight the highest and lowest values of He/CO_2 ratios. Dominant He bulges are indicated by E1 to E5 78

5.3 a) Latitude versus LST variation of He density for (a – d) Ls 0°, 90°, 180°, and 270° as observed by NGIMS at 200 km. The data are averaged on a latitude and local time grid of 5° × 0.33 hr. 79

5.4 Similar to Figure 5.3, but for He/CO_2 ratios. 80

5.5 Similar to Figure 5.3, but the He densities shown are from M-GITM simulations for nominal dust conditions. The arrows show the modeled horizontal winds. 81

5.6 Similar to Figure 5.3 but shows the ratios of the observed and modelled He densities (shown by colorbar). The green and yellow arrows represent the winds observed by NGIMS and modelled by M-GITM, respectively. Tails of the arrows show the location of the winds, length of the arrows show the magnitude (reference magnitude is shown by red arrow in panel c) and heads of the arrows point to the direction of the winds. 82

6.1 Local solar time (LST) versus solar longitude (Ls) variability of densities of a) He, b) N_2, c) Ar, d) CO_2, and e) latitude coverage of MAVEN spacecraft. The data are averaged over a grid of 1 hr in LST and 10° in Ls. 87

6.2 Similar to Figure 1, but color coded with mixing ratios- a) He/CO_2, b) N_2/CO_2, and c) Ar/CO_2. Panel d) represents the latitude coverage by MAVEN spacecraft. Here, green shaded boxes are used to highlight the dust storm season (Ls 180°-270°) in MY 33 and MY 34 89

6.3 Latitude versus local solar time variation of Ar/CO_2 for (a–d) Ls=0°, Ls=90°, Ls=180°, and Ls=270° for 200 km. The data are averaged over a latitude and local time grid of 5° × 0.33 hr. 90

6.4 Temporal (as a function of solar longitude (Ls)) variation of, during MY 33 (left column) and MY 34 (right column) (a) He/CO_2 ratios, (b) N_2/CO_2 ratios (c) Ar/CO_2 ratios, (d) MAVEN latitude, for 200 km e) latitude versus Ls variation of CDOD values, and f) CDOD values averages over latitudes 50N to 50S. The solid vertical lines are drawn to highlight the enhancements in the mixing ratios- He/CO_2 ratios. Dashed vertical lines are drawn to highlight dust storm peaks 91
6.5 a) Variability (as a function of homopause altitudes) in Ar/CO_2 ratios, and b) CO_2 density. The data points are color coded with the Local Solar Time. 95

List of Tables

1.1 Comparison of Important orbital and Physical Parameters of Mars and Earth. Source https://nssdc.gsfc.nasa.gov/planetary/factsheet/Marsfact.html 2

1.2 Comparison of Atmospheric Properties of Mars and Earth. Source https://nssdc.gsfc.nasa.gov/planetary/factsheet/Marsfact.html 8

1.3 Comparison of Atmospheric Composition of Mars and Earth. Source https://nssdc.gsfc.nasa.gov/planetary/factsheet/Marsfact.html 9

2.1 Packages and instruments onboard MAVEN 28

4.1 Summary of MOM orbital parameters at the periapsis and scale heights and derived temperatures for Ar (with 1σ error) measured by MENCA on six days in June 2018 64

4.2 Summary of MAVEN orbital parameters at the periapsis and scale heights and derived temperatures of Ar measured by NGIMS for selected days in June 2018 65

Chapter 1

Introduction to Mars atmosphere

1.1 A Brief Introduction to Mars

'Mars' is a bright red-tinted planet, often visible to naked eyes, that has intrigued space enthusiasts and astronomers around the globe. It is the fourth planet from the Sun in terms of radial distance and the seventh-largest planet in the solar system in terms of size. For nearly five decades the planet has been the primary focus of the international planetary science community and several space agencies such as the National Aeronautics and Space Administration (NASA), the European Space Agency (ESA) and the Indian Space Research Organization (ISRO) have been sending spacecraft to explore several aspects of its surface, subsurface, and atmosphere. The beginning of the Mars exploration era dates back to the year 1965 when NASA's Mariner 4 successfully flew past the planet and captured its first close-up images. Since then, observations from several planetary missions have been significantly refining our knowledge about the Mars environment. Data from these missions showed striking features on the surface of Mars that can undoubtedly be associated with flowing liquids and branching streams in the past. It is also likely that Mars once had a thick atmosphere and climate conditions that could sustain liquid water on its surface. The present-day Mars, however, is cold and dry with a thin atmosphere. Spacecraft observations and model simulations suggest that Mars probably lost most of its atmosphere to outer space and continues to do so even today (e.g., [8]). This escape process to outer space depends on several underlying factors, in which the thermosphere (˜100-200 km) plays a central role. Thus to quantify the escaping processes, planetary scientists have been proactively characterizing the Martian thermosphere using spacecraft observations and model simulations.

The discussion on the Mars atmosphere must be contextualised in the broader orbital and physical, topographical and climatological understanding about the planet ([9, 10, 11]),

an understanding developed through painstaking scientific investigation. Mars and Earth share several similarities as well as dissimilarities in terms of their orbital and physical parameters. A comparison of these parameters of Mars and Earth is summarized in Table 1.1. The length of a day on Mars (rotation period) is only 37 minutes longer than that on Earth. The season driving parameter, known as obliquity, of Mars (25.19°) and Earth (23.5°) are also similar. However, the orbital period of Mars around the sun is almost twice (686 days) as that of Earth's (365 days) orbital period around sun. Further, Mars's orbit is more eccentric (0.09) than Earth's (0.01) with a perihelion of 1.38 Astronomical Units (AU) and aphelion of 1.68 AU. As a consequence, seasons are more extreme on Mars and there is a large seasonal variability in its atmospheric composition. A 45% low insolation received on Mars, which is due to its 1.5 times larger orbital radius than of Earth, leads to very low temperatures in the Mars atmosphere. The first measurement of surface temperature (recorded at Viking 1 landing site) showed a value of - 68°C [12]. The equatorial diameter of Mars is roughly half of that of the Earth. Owing to its lesser mass than of Earth, the acceleration due to gravity (g) on Mars is 3.7 m/s^2, nearly half of that of Earth's 9.8 m/s^2. As a consequence, the velocity required by the atmospheric species to escape Mars is also much less (5.2 m/s on Mars vs. 11.2 m/s on Earth). Thus, the orbital and physical parameters play an important role in structuring the atmosphere of Mars.

Table 1.1: Comparison of Important orbital and Physical Parameters of Mars and Earth. Source https://nssdc.gsfc.nasa.gov/planetary/factsheet/Marsfact.html

Orbital and Physical parameters	**Mars**	**Earth**
Orbit period (days)	686.98	365.26
Perihelion distance (10^6 km)	206.62	147.09
Mean orbital velocity (km/s)	24.07	29.78
Orbit eccentricity	0.093	0.017
Rotation period (hrs)	24.62	23.93
Orbital Radius (AU)	1.50	1.00
Obliquity (deg)	25.19	23.44
Solar irradiance (W/m^2)	586.20	1361.00
Mass (Kg)	6.42e+23	5.97e+24
Equatorial radius (km)	3389.50	6378.00
Gravitational acceleration (m/s^2)	3.72	9.81
Escape velocity, V_{esc} (km/s)	5.03	11.19
Equilibrium temperature, T_e (K)	210	256
Mean density (kg/m^3)	3933	5515
Solar irradiance (W/m^2)	586.20	1361.00
Average surface albedo	0.25	0.31

The atmosphere of Mars is also influenced by its surface properties. Although there is evidence which shows signatures of flowing liquids and water bodies in the past [13, 14, 15], at present there is no evidence of flowing water or bio-signatures on the surface of Mars. As a matter of fact, the surface of Mars is barren and dusty. This contributes to a large difference in the climate of Mars and Earth. For example, the absence of liquid water lowers specific heat and average albedo on Mars (see Table 1.1). The surface albedo is an important physical parameter for a planet because it determines how much of the incident radiation is reflected. The reflected far infrared wavelengths (3-50 μm) from the surface get absorbed in the atmosphere and influence the global temperature of the planet. The surface conditions together with the seasonal cycle of carbon dioxide CO_2 (discussed further and in section 1.5.1) give Mars an environment where the dust storms and dust devils are very common and these storms are one of the major driving engines of the planets' climatology.

Mars' mountain *Olympus mons* (shown in Figure 1.1), 25 km high and about three times the height of mount Everest on Earth, is the second highest mountain in the solar system, next only to the *Rheasilvia* mountain on the asteroid *Vesta*. Its edifice is a massive volcano with a diameter of 600 km. Mars also houses the deepest and longest valley in the solar system. Mariner 9 probe discovered a system of canyons know as *Valles Mareneris*, nearly 10 km deep and 4,000 km in length. The layered sediments in these canyons suggest that there was once flowing water. Unlike other terrestrial planets, Mars exhibits a dichotomous geology. The low-lying northern plains have relatively few craters, whereas the elevated southern hemisphere is covered with large number of craters (including the 2,300 km wide *Hellas Planatia*, the largest crater on Mars) indicative of its older age. The northern plains are some of the flattest and smoothest regions in the solar system (Figure 1.2).

Another important and distinctive surface feature found on Mars (and not on Earth) is seasonal polar ice caps (shown in Figure 1.6). The temperatures at the polar regions, particularly during southern polar winter of Mars, are low enough to freeze the atmospheric carbon dioxide to form a thin layer of CO_2 ice. However, as the seasons progress, the condensed CO_2 sublimate and replenish the atmosphere. The sublimation of CO_2 ice begins in early spring in northern hemisphere and completely sublimes by the end of the season. This seasonal cycle of CO_2 (discussed in detail in section 1.5.1) determines the spatial and temporal variations in compositional and dynamical state of Mars. Thus, CO_2 cycle is a dominant force and a critical aspect of martian climate.

Unlike Earth, Mars does not possess an internal dynamo that could generate a large global magnetic field. The magnetometer measurements from MGS mission, however, showed that Mars possess a remanent crustal magnetic field, a remnant of its once active

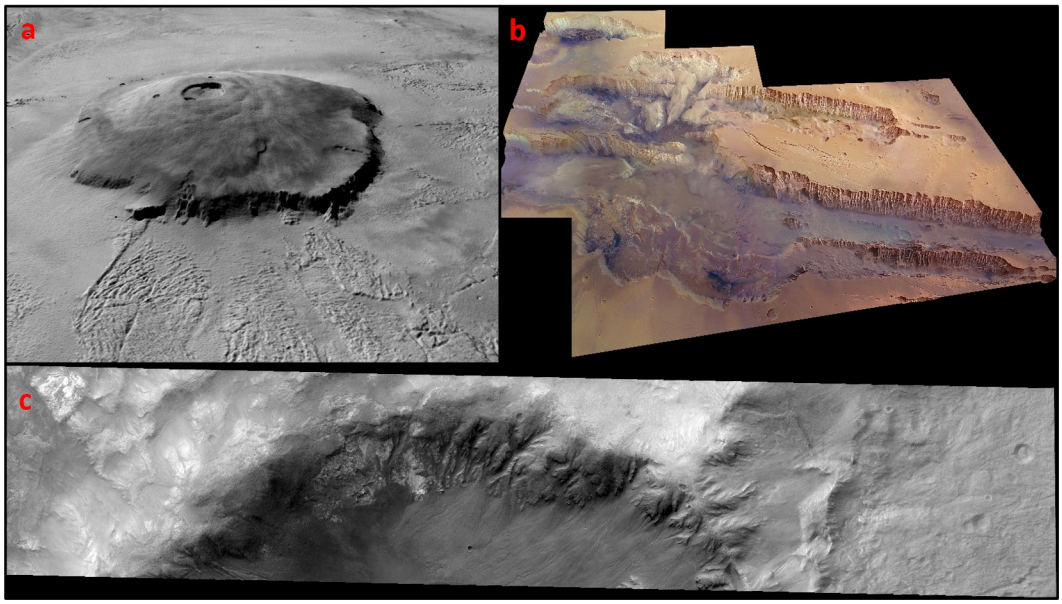

Figure 1.1: a) Olympus Mons' 3D view derived from Mars Orbiter Laser Altimeter's (MOLA) topographic data superimposed with the Mars Orbiter Camera' (MOC) wide-angle image mosaic, b) Valles Marineris, seen at an angle of 45° from Mars Express (ESA, 2009), and c) Hellas basin as seen by Exomars Trace Gas Orbitor's Colour and Stereo Surface Imaging System, CaSSIS on 29 May 2018

global magnetic field, in the southern high lands [16]. These magnetic fields are present in the rocks on the surface and form localised magnetospheres. The magnetic field lines from these magnetospheres determine the interaction of the atmosphere with incoming solar wind. There are regions where the magnitude of the crustal magnetic field at certain altitudes is stronger than the magnetic field of Earth at that altitude. The "cusp" regions, where these magnetic field lines are vertical, allow the solar wind particles to enter the atmosphere and ionize its neutral constituents and facilitate the escape of high energy atmospheric ions to space. Thus, the crustal magnetic field play an important role in altering the atmosphere of Mars.

1.2 Seasons on Mars

Mars has four distinct seasons similar to Earth. However due to higher elliptical orbit and larger orbital period of Mars as compared with Earth, the duration of seasons is nearly twice as long as on Earth. Martian seasons are defined by "Solar Longitude (Ls)", which is an angle between the sun and Mars measured with respect to the northern hemisphere spring equinox or Ls = 0°. Thus, Ls = 90° corresponds to the northern summer solstice,

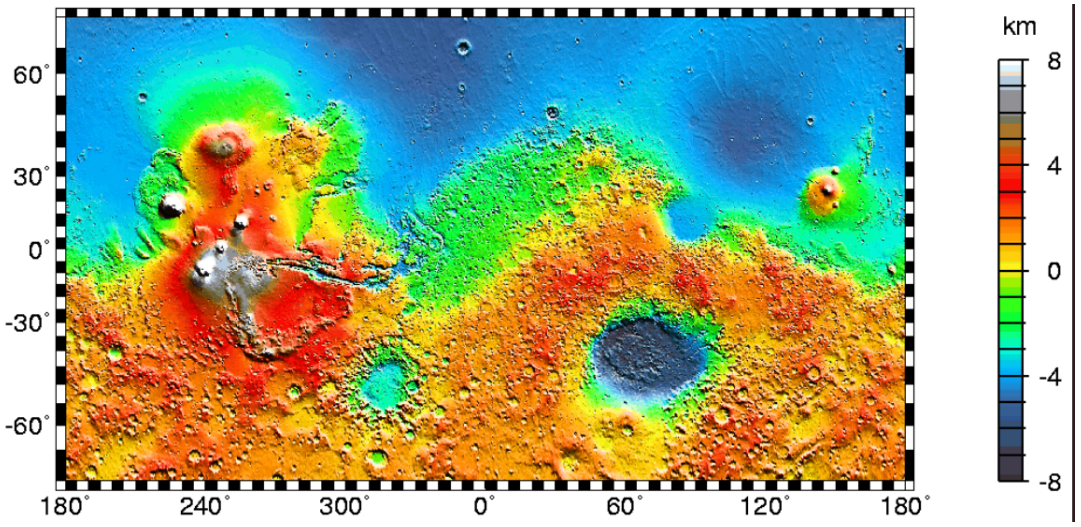

Figure 1.2: Map of surface topography of Mars as observed by MGS-MOLA. The elevation of topography is presented by the color scale. (Courtesy: NASA)

Ls = 180°, corresponds to the northern autumnal equinox and Ls = 270° marks northern winter solstice (Figure 1.3).

Mars orbits farthest from the Sun when its northern hemisphere is tilted towards the sun. Thus, Ls = 90°, in addition to northern summer season, falls in the period of aphelion time for Mars. Similarly, Mars is closest to the sun during Ls = 250°, hence in addition to southern summer, it is perihelion time for Mars. Thus, there is a strong temperature difference between southern summer and northern summer such that atmospheric temperatures during southern summer are larger than those in the northern summer. The combination of southern summer during Ls = 270° and perihelion time for Mars, causes extra heating of the southern hemisphere leading to strong disturbances and intensified wind circulations in the martian atmosphere. This in turn gives rise to strong local, regional, and global dust storms. The large seasonal temperature variation also causes the strong atmospheric CO_2 cycle as discussed in section 1.1 and 1.5.1 and spatial and temporal variations in the atmospheric composition and circulation as well.

1.3 Atmosphere of Mars

Atmosphere is defined as a layer of gases and aerosols that envelopes a planet. It is held in place by the gravitational pull of the planetary body. Mars atmosphere is very tenuous compared to Earth's atmosphere. Mars may have started off with an atmospheric pressure a little above 1 bar, however, enormous amount of its atmosphere (>99%) has escaped

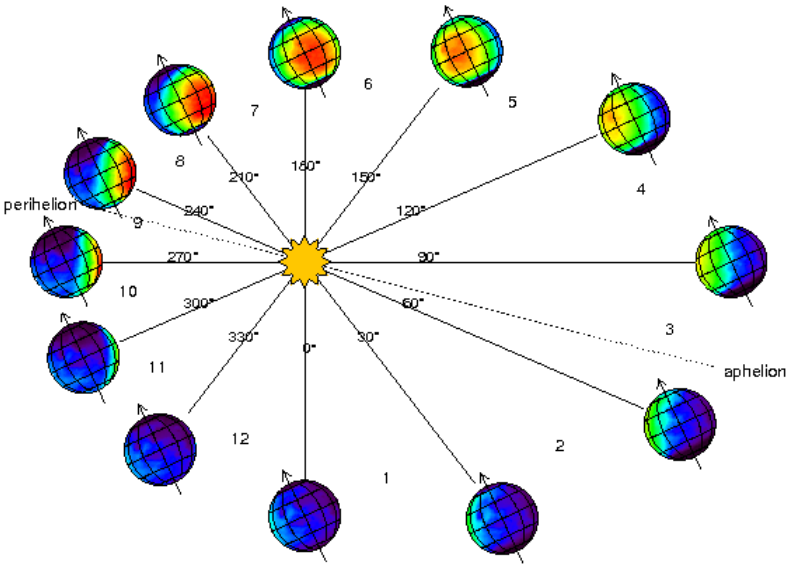

Figure 1.3: Schematic of seasons on Mars. Dashed lines represent the perihelion and aphelion approaches of Mars to the Sun. Solid radial lines represent the beginning of each "month". Color coding indicates surface temperature in each season and the local time shown for each image (indicating which portion of the planet is facing the Sun in each position). From http://www-mars.lmd.jussieu.fr/ mars/time/solar_longitude-html

the relatively low gravitational attraction (see Table 1.1) of the planet [17]. The tenous atmosphere of Mars exerts a surface pressure which is one-hundredth of that on Earth (Table 1.1). The pressure decreases with increase in altitude and fluctuates with martian seasons. The seasonal variation in atmospheric pressure is mostly due to the seasonal variation in polar ice caps [18, 19]. In addition, crustal dichotomy of Mars and geostrophic balance between pressure gradient and coriolis forces have been observed to contribute to the observed variability of atmospheric pressure [20, 21]. As shown in Figure 1.4, the maximum pressure occurs when Mars is near the perihelion (Ls = 251°, northern winter) and the minimum pressure is recorded near the aphelion (Ls = 71°, southern winter).

All stable atmospheres require a hydrostatic balance or equilibrium between the upward directed pressure gradient force and the force of gravity in the downward direction.

$$dp = -\rho g dz \tag{1.1}$$

Here, z is height, g is acceleration due to gravity on the surface. Further, the neutral atmospheric gas assumes ideal gas law,

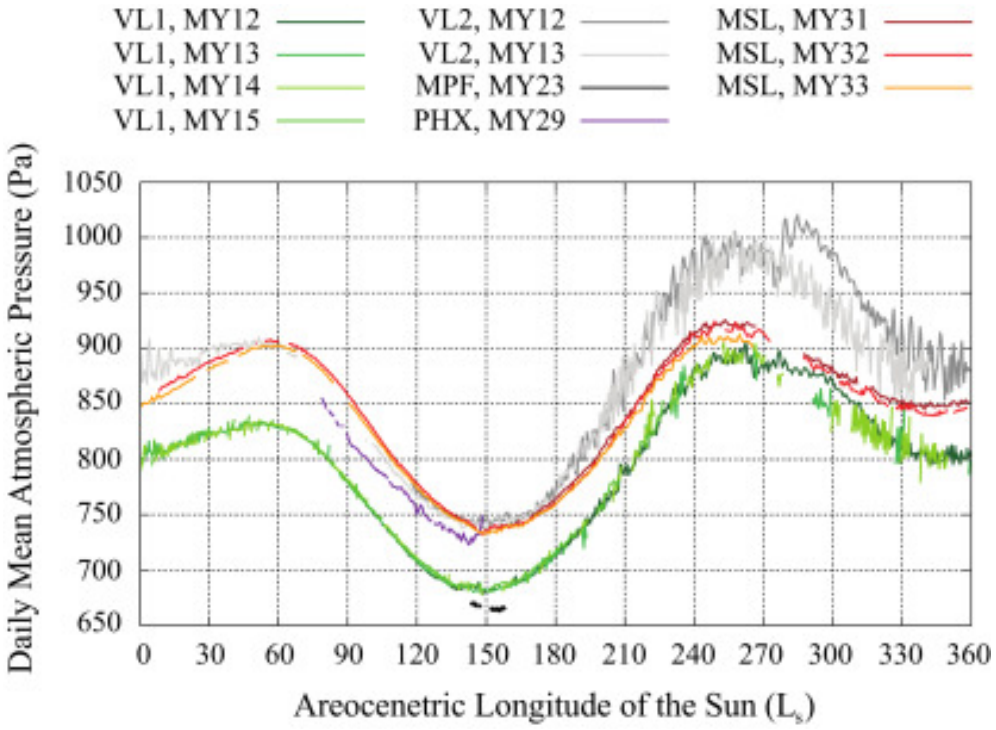

Figure 1.4: Variation in atmospheric pressure with seasons on Mars, as measured by Viking Lander 1 (green colors), Viking Lander 2 (gray colors), Mars Pathfinder (black), Mars Phoenix Lander (purple), and Mars Science Laboratory (red/orange colors). This figure is: modified from Figure 3 of [1]

$$P = \rho RT \tag{1.2}$$

where, $R = 8.314 J/K/mol$ is universal gas constant. By combining and solving the above equations, we find that atmospheric pressure decreases exponentially with the increase in height.

$$p = P_o exp(\frac{-z}{H}) \tag{1.3}$$

In the above equation, P_o is the pressure at a reference height and H is the scale height of atmospheric pressure given by,

$$H = \frac{kT}{\mu g} \tag{1.4}$$

Here, $k = 1.38 \times 10^{-23} J/K$ is the Boltzmann constant and μ is mean molecular mass of the atmosphere. The scale height is defined as the vertical distance at which the atmospheric

pressure (and density) reduces to the 1/eth times of the pressure at the reference altitude (P_o). For Mars, the average value of scale height is 10.8 km which is lesser than that on the Earth (Table 2). As a result, the rate of decrease in temperature with height, also called lapse rate, is much slower than that on Earth.

$$\tau = -\frac{dT}{dz} \tag{1.5}$$

Table 1.2: Comparison of Atmospheric Properties of Mars and Earth. Source https://nssdc.gsfc.nasa.gov/planetary/factsheet/Marsfact.html

Property	**Mars**	**Earth**
Surface pressure, (Pa)	600	101350
Pressure scale height (H, km)	10.80	8.00
Mean lapse rate, $\tau(-K/km)$	2.50	6.50
Equilibrium temperature, Te (K)	210	256
Surface temperature (K)	140-300	230-315

The atmospheric composition of Mars differs greatly from that of Earth. The comparison of composition of both planetary bodies is shown in Table 1.3. The homogeneous/well mixed region of Mars atmosphere is composed of carbon dioxide CO_2 (95% by volume), nitrogen (2.7%), argon (1.6%) and traces of helium, oxygen, carbon monoxide, water vapour, methane and dust. Whereas, Earth's atmosphere is composed of nitrogen (N_2, 78%), oxygen (O_2, 21%), argon (Ar, 0.9%) and traces of other gases. Water vapour content in Martian atmosphere is only 0.13% by volume, much less than that on Earth. As a result, Mars atmosphere is very dry with very less cloud formation. Unlike the primary species N_2 on Earth, CO_2 on Mars is a condensable gas. During polar winter seasons, approximately 25% - 30% of the atmospheric CO_2 condenses out in the form of CO_2 ice in the polar regions of Mars [22, 23]. This leads to huge latitudinal gradients in atmospheric pressure which influences the large-scale wind circulation in the atmosphere of Mars. The seasonal cycle of CO_2 is further discussed in section 1.5.1

Following the altitude and temperature dependent division of the atmosphere of Earth, the atmosphere of the Mars is divided into Troposphere, Mesosphere and Thermosphere (as shown in Figure 5). The troposphere of Mars extends from surface to 60 km, whereas on Earth it is only 12 km deep. In the troposphere, the atmospheric temperature decreases with the increase in height. The rate of decrease of temperature in the troposphere is ˜2.5 k/km on Mars and ˜6.5 K/km on Earth. However, measurements from MGS radio occultation have shown temperature inversion in troposphere below 10 km [24] which is similar to

Table 1.3: Comparison of Atmospheric Composition of Mars and Earth. Source https://nssdc.gsfc.nasa.gov/planetary/factsheet/Marsfact.html

Property	Mars	Earth
Carbon dioxide	95.32	0.04
Nitrogen	2.70	8.00
Argon	1.60	0.93
Oxygen	0.13	21
Water vapour	0.03	1.96

Earth.

In Earth atmosphere, above troposphere lies the stratosphere wherein temperature increase with altitude. The increase in temperature in this region is due to the large abundance of atmospheric ozone that absorbs solar UV radiations leaving the region hotter than that in the troposphere. However, there is no such persistent layer on Mars. This is due to insufficient amount of ozone present in the atmosphere of Mars.

In Mesosphere temperature becomes nearly isothermal. The rate of decrease in temperature (in mesosphere) is much slower as compared with that in troposphere. This is due to combined effect of weak EUV heating, increased 15 μm cooling and absence of convective heating in the Mesosphere. Thus, for Mars, there is a continuous decrease of atmospheric temperature from surface upto Mesopause (˜100 km). At Mesopause the temperature attains a minimum value of ˜160 – 180 K. Mesopause act as an inflection boundary where slope of temperature profile becomes positive. Above Mesopause lies the Thermosphere of Mars.

The Thermosphere of Mars extends roughly from ˜100 - ˜200 km, and in this layer the temperature rapidly increases with increase in altitude. This is primarily due to the absorption of Extreme Ultraviolet (EUV) and UV radiations. In addition, dynamical processes such as gravity waves and global circulation have been found to have significant heating and cooling effect in the region [25, 26, 27, 5, 28]. Further, short term events such as solar flair and dust storms further complicate the heat budget of the region [29, 30, 31, 32]. A detailed discussion of the heat budget is given in section 1.6. The complexity of the thermal balance in thermosphere coupled with its strong dependence on solar activity leads to strong seasonal, latitudinal and local time variabilities. In addition, the atmosphere of Mars is divided into dynamics-based regions; lower atmosphere (0-50 km), middle atmosphere (50 – 100 km) and upper atmosphere (100-200 km). The upper atmosphere mostly comprises the thermosphere of Mars. Thermosphere of Mars is the hottest layer of the atmosphere.

Figure 1.5 also reveals the significant role of dust events or dust storms on Mars. During dust storms, a huge amount of dust gets lofted up by the winds in the atmosphere of Mars. The levitated dust particles absorb heat and alter atmospheric parameters like temperature and pressure. Although, the occurrence of dust events is common to Mars as well as Earth, the occurrence of dust storms on global scale, also known as Global Dust Events (GDE) is unique to Mars. The absorption of heat by dust particles during a planetary scale dust event can cause enhancement in atmospheric temperature as much as by ˜40 K, as shown in Figure 1.5 (dashed curves). Martian dust storms and related dynamics are further discussed in Section 1.5.2.

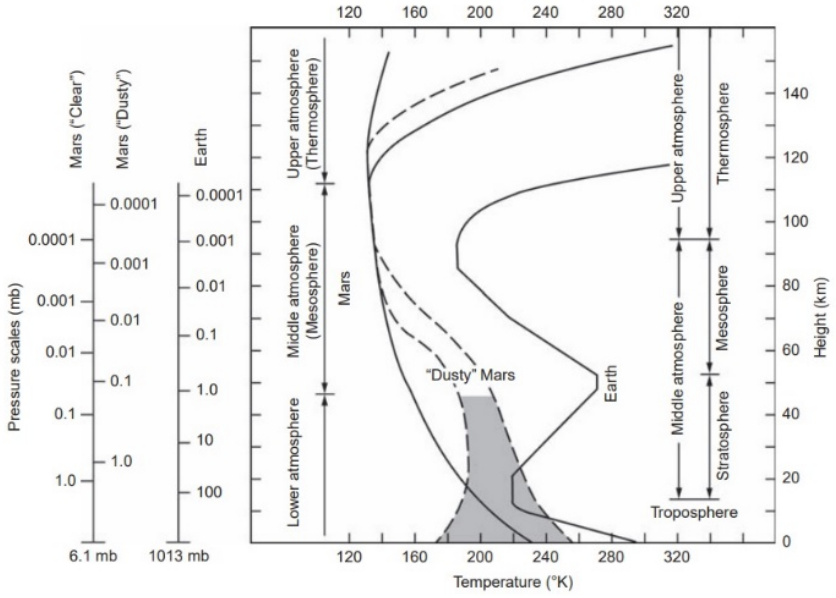

Figure 1.5: A comparison of the vertical structure of the atmosphere of Mars and Earth from [2]

The atmosphere of Mars can also be divided on the basis of its composition boundary, known as homopause. Homopause, in general is defined as a transition boundary between a well-mixed atmosphere to a diffusively separated region of a planetary body. Below homopause, the atmospheric constituents are homogeneously mixed by atmospheric turbulence (eddies). At homopause, molecular diffusion becomes dominant process over eddy diffusion. The region above homopause is known as heterosphere. In the heterosphere, the atmospheric constituents stratify according to their masses and scale heights [4, 33]. Heavier species such as CO_2 and Ar are more abundant near homopause and the lighter species such as O and He are dominant at higher altitudes.

Several other boundaries can be identified for the atmospheric region above homopause

based on photo chemistry. These boundaries are related to the Martian ionosphere. However, the work in this thesis focuses on the neutral upper atmosphere (>100 Km) comprising of thermosphere and exosphere of Mars. Thus, the ionosphere of Mars is not dealt with in detail.

1.4 Dynamics

1.4.1 Gravity Waves

Gravity Waves (GWs) are periodic disturbances in the vertical motion of atmospheric density. As the lower atmosphere (below tropopause) is turbulent in nature, and the atmosphere above it is relatively stable and stratified, GWs originate in lower part of the atmosphere and transport energy and momentum to the upper atmosphere. The vertical disturbances such as temperature and pressure gradient forces on the vertical motion of air parcels produce the gravity wave oscillations in the middle atmosphere [34] and upper atmosphere [35]. These oscillations are maintained by gravitational and buoyancy forces, that propagate through the atmosphere and are now well characterized on Mars. As the atmospheric density decreases with height, the amplitude of gravity wave increases with height to conserve energy. At a critical frequency, the oscillatory motion breaks and GWs quickly lose their kinetic energy and momentum. The critical frequency at which gravity wave breaking occurs in known as *Brunt Vaisala frequency* (N, given by equation 1.6) and is a function of environmental $(\frac{dT_o}{dz})$ and adiabatic lapse rate $(\frac{g}{C_p})$. The environmental lapse rate is defined as the rate of change of atmospheric temperature (T_o) with an increase in altitude (z). Adiabatic lapse rate, given by $\tau = -\frac{g}{C_p}$, is the change in temperature of an air parcel when it moves vertically and adiabatically due to pressure gradient in the atmosphere.

$$N = (\frac{g}{T_o}[\frac{dT_o}{dz} + \frac{g}{C_p}])^{1/2} \tag{1.6}$$

Here, g is the acceleration due to gravity and Cp is the specific heat at constant pressure.

Gravity waves in lower atmosphere can be excited by several sources that include flow over surface topography or atmospheric convection [36, 37, 38], front systems, and jet streams [34]. Whereas, in the upper atmosphere, vertically propagating atmospheric tides have been found to create fluctuations in the atmospheric density [39]. Rougher topography, thinner atmosphere and more volatile weather system of Mars as compared with those on Earth leads to larger amplitudes of Martian GWs than those in the thermosphere of Earth

[40, 41]. The GW dissipates energy through several dissipative processes such as molecular viscosity, thermal conduction, eddy diffusion, fast chemical reactions, ion drag, and radiative processes [41, 42, 25, 43]. The dissipated energy is absorbed by the atmosphere, which then produces heating and cooling in the middle and upper atmosphere [25, 44]. Thus, gravity waves are crucial to understand the spatial and temporal variability of the thermosphere of Mars.

The vertical wavelength of the gravity waves is of the order of few kilometers. Whereas, the horizontal wavelength ranges from few km to several hundreds of kilometers. Gravity wave undulations with a time period of a few days to weeks and a spatial scale of the order of 10^3 km are termed as *Planetary Waves* (PWs) [45, 46, 47, 48, 49]. Planetary waves are inertial waves that occur naturally due to planetary rotation and subsequent influence of Coriolis and pressure gradient forces. GWs perturbations generated in the atmosphere above the terminator regions are known as *Terminator Waves* (TWs). Terminator Waves originate in the lower atmosphere as a consequence of sudden heating due to night-to-day transition in dawn terminator and cooling due to day-to-night transition in dusk terminator [50]. The vertical wavelength of the TWs is of the order of few tens of kilometers [51, 52, 53]. Atmospheric *tides* are generated due to diurnal differential heating of the atmosphere by the sun. Tides on Mars are in general triggered by the interaction of atmosphere with topography of a planet [54, 37]. More recently, studies have found that the atmospheric tides are closely tied to atmospheric dust loading [55] and water ice aerosol loading [56, 57, 58]. In addition, solar driven atmospheric tides are now well established for middle atmosphere (˜50 km -70 km) and upper atmosphere (˜70 km – 110 km) [59, 60, 61]. The time period of atmospheric tides is subharmonic of a solar or lunar day. Similar to GWs, tides also propagate in vertical direction such that their amplitude grows with height. The vertical wavelength of tides varies from 10 to 10^2 km [60, 46].

On Earth, several studies have pointed out the importance of gravity waves of lower atmospheric origin in terms of their influence on the circulation of thermospheric region [62, 62, 44]. Similarly, on Mars, gravity waves have been observed to greatly influence the state of the thermosphere. Vertically propagating gravity waves, have been found to alter the thermal [25, 35] and dynamical state [42] of the thermosphere of Mars. These variations play a crucial role in shaping the spatial and temporal state of the thermosphere, as will be discussed in the following chapters.

1.4.2 Circulation

In a planetary system, the principal source of large-scale atmospheric circulation is the differential heating by solar radiation. The corresponding latitudinal and longitudinal pressure gradients result in the propagation of winds from high pressure to low pressure regions of the atmosphere. Our scientific understanding of atmospheric circulation on Mars is second only to that of Earth. There are remarkable similarities as well as significant differences between circulations on Earth and Mars. Absence of large water bodies such as lakes and oceans on Mars results in very low thermal inertia on Mars. In addition, extreme seasons on Mars generate stronger seasonal variations in the atmospheric circulation as compared to the seasonal variations in Earth's wind fields [63, 11, 64].

During equinoxial seasons i.e., Ls = 0° and Ls = 180°, the equatorial latitudes receive more solar flux than the polar regions of Mars. As a result, an air parcel over the equatorial latitudes rises from middle atmosphere to high altitudes. The air parcel then tends to move towards the polar regions of both the hemispheres of Mars. Air parcels thus accumulate or converge near the poles. The adiabatic compression associated with such convergence of winds in the polar regions leads to sudden heating in the polar regions of Mars [5]. These winds return back to the equatorial region and form a pair of meridional wind cells (known as Hadley cells) in the northern as well as southern hemisphere of Mars. The polar warming feature above 20 km implies the presence of a two-cell circulation. While the formation of Hadley cells is symmetric over latitudes during equinoctial seasons, it is stronger over the summer latitudes during solstice seasons [63, 11]

During solstice seasons i.e., Ls = 90° and Ls = 270°, the region of divergence of air parcel shifts from equator towards the high latitudes of summer hemisphere. The air parcel rises towards the high altitudes, crosses over the equatorial region and converges in the winter polar regions of Mars, thus resulting in one of the Hadley cells spanning more than 90 degrees in latitude. During Ls = 270°, southern hemisphere of Mars experiences summer season and the meridional wind flows northern poleward. Since it is the perihelion time for Mars, the southern hemisphere becomes much hotter than the northern hemisphere. This leads to an enhancement in pressure and temperature gradients between the two hemispheres. As a consequence, Mars observes the stronger mean meridional circulation in southern hemisphere as compared to the northern hemisphere, during Ls = 270° [2].

Coriolis effect is another important factor that influences the atmospheric circulation on Mars. This effect is related to the rotational motion of the red planet or for that matter any rotating object. If Mars did not rotate, the atmospheric winds would have a straight path.

The meridional winds (parallel to longitudes) would only flow from northern summer to southern winter. The zonal winds (parallel to latitudes), that are generated due to day-night difference in solar heating would flow from day to night regions of Mars. However, due to coriolis effect the winds in northern hemisphere, with the increase in altitude and towards the polar regions would get deflected slightly towards the evening terminator region and the winds in the southern hemisphere would get diverted towards the dawn terminator. Thus, instead of following a straight path, winds follow a curved trajectory. As a consequence, there is an additional zonal wind component in day-night-day direction. For example, during Ls = 90° southern hemisphere is in winter season and northern hemisphere is in summer season. The large-scale circulations in the thermosphere and their seasonal variability are the major source of local time, latitudinal and seasonal variations in distribution of thermospheric constituents.

1.5 Seasonal Cycles

The important seasonal cycles in the atmosphere of Mars that play a key role in determining its present atmospheric state are CO_2 cycle, dust and H_2O cycle. However the only dust and CO_2 cycle have significant effect on the variabilities discussed in this thesis. In the following sections, we discuss these two cycles.

1.5.1 CO_2 cycle

CO_2 cycle on Mars is a process in which carbon dioxide is exchanged between dry ice on the surface, particularly in polar regions and the atmosphere. Along the course of the Martian year, as the season changes, the atmospheric CO_2 condenses and sublimates over the polar regions of Mars [65, 19] (Figure 1.6). The seasonal CO_2 cycle is a direct consequence of the seasonal variation in the surface temperatures on Mars. During the winter seasons at the polar regions, the surface temperatures are as low as ˜140 K, which is lower than frost point of CO_2 present in the atmosphere of Mars. This means that the atmosphere is cold enough to convert the atmospheric CO_2 gas directly into CO_2-ice (Condensation). Thus, a significant amount of CO_2 is removed from the atmosphere and get deposited onto the surface in the form a thin layer of CO_2-ice. Approximately 25%–30% of the atmospheric mass (and therefore atmospheric pressure) is cycled as the seasonal polar caps grow and disappear annually [22, 23]. This process is responsible for the large seasonal variation in surface pressure observed on Mars (Figure 1.4).

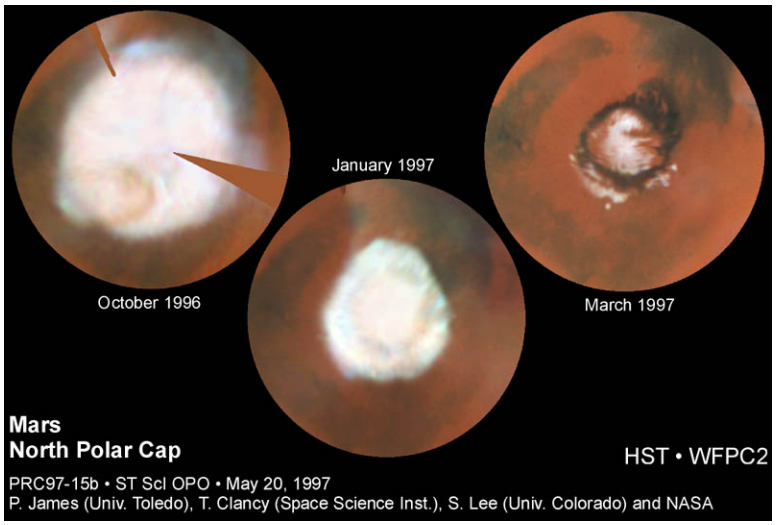

Figure 1.6: Images of the CO_2 ice Cap in the Northern Polar region, captured by the Hubble Space Tele scope. This Figure shows sublimation of CO_2 Ice as the season changes from winter (far left) to northern spring (far right). Image credit: Phil James, Todd Clancy, Steve Lee, and NASA (http://hubblesite.org/gallery/album/entire/pr1997015b/)

As 95% of the Mars atmosphere is made up of CO_2, the condensation and sublimation processes lead to seasonal, latitudinal and local time variability of the relative composition of other atmospheric non-condensable gases (Ar, N_2, CO, and etc.) in the lower atmosphere [66] as well as in upper atmosphere of Mars [67]. During polar winter season, when atmospheric CO_2 condenses onto the surface, the atmosphere becomes more enriched with non-condensable gases relative of CO_2. [68, 69] reported 1.5 – 6 times enhancement in Ar column abundance over the seasonal polar caps of Mars. When spring and summer seasons arrive, the temperature rises above the frost point, CO_2 sublimates off the ice caps and replenish the atmosphere. While the atmospheric CO_2 goes through growth and retrieval process, background atmosphere simultaneously tries to restore its equilibrium state. As a result, it drives large-scale meridional and zonal winds in the atmosphere of Mars [21, 70].

The climatology of Mars is also indirectly influenced by such important atmospheric cycles as H_2O cycle and dust cycle which can alter the seasonal cycle of CO_2 [71]. Subsurface CO_2-ice can store heat in summer season and can reduce the rate of accumulation of CO_2 on the surface during winter season [72, 73, 74]. Further, dust can influence the sublimation rate of CO_2-ice as it can change the emissivity and albedo of CO_2-ice by acting as condensation nuclei. Surface topography can further affect the CO_2 cycle by varying the amount of CO_2 deposition in the polar regions [71]. Thus, CO_2-cycle is a key driver of the Martian climate.

1.5.2 Dust cycle

The presence of suspended dust in the lower atmosphere is common to both Earth and Mars [75]. However, the phenomenon of dust storms, that results due to strong winds and dry and arid surface, is relatively more intense on Mars. The Martian dust storms can vary from local to regional and global on spatial scales. In addition, dust devils [76], dust cells [77], dust clouds [78], and dust plumes [79] are other types of dust activity that have been observed on Mars. The particulate matter that gets lifted up in the atmosphere usually has radius ranging from 0.9 μm to 1.9 μm in size [80, 81]. The airborne dust absorbs solar radiations and re-emits at the Infrared (9 μm) wavelength [82]. This results in significant heating of the Mars' lower atmosphere [83, 42, 84]. Dust aerosols have been observed to extend to high altitudes (above 60 km) in Mariner 9 [85], Viking [86], MGS [87, 78], and MRO limb measurements [88], associated with the 1971, 1977, 2001, and 2007 planet-encircling dust events, respectively. Although the airborne dust can extend up to ˜60 km, the thermal expansion of the lower atmosphere significantly influences the thermal, compositional and dynamical state of the upper atmosphere as well [89, 32, 90, 91, 31]. In addition, dust storms have been observed to have significant effect on the atmospheric escape rates as well [92, 93].

Dust loading in the atmosphere has been observed to occur repeatedly in each Martian year, with significant annual variability in the dust abundance. Although year-to-year variability exists at specific seasons, some aspects of the behavior of dust repeat from one year to the next. The total atmospheric dust loading is generally characterized by low levels during northern hemisphere spring and summer, and increased levels during northern hemisphere autumn and winter [82, 94, 95]. Such periodic occurrence of dust loading is known as dust cycle. Ls = 0° – 135° is the season of low-level dust loading (also referred as non-dusty season) in which the atmosphere is essentially clear and constitutes few dust particulates with respect to background atmosphere. It is notable that no large regional or global dust storms have been recorded during these seasons [96, 97, 98, 99, 82, 95, 100]. Ls = 135° – 360°, on the other hand, is season of high dust loading. During Ls = 135° – 360°, Mars is closest to sun (perihelion), during which time it experiences summer season with in its southern hemisphere. The combination of southern summer season at perihelion time leads to the heavy dust loading in the atmosphere and formation of regional or global dust storms. Local, regional and global dust storms with a variety of timings and sizes are observed [82, 95, 101]. However, regional dust storms are more common than the global dust storms. While, all the dust storms have been observed to originate in southern hemisphere,

they can vary year-to-year in terms of latitude, timing and duration. In addition, local dust storms or dust devils are also very common on Mars. They are swirling columns of winds that leaves giant tracks that are more than 30m wide and ˜4km long. The largest dust devils can reach up to height of ˜8 km and significantly contribute to the dust suspension in the atmosphere.

Global dust storm is a dynamical meteorological phenomenon on Mars during which whole planet gets engulfed in dust particles, thus earning them the name Planet Encircling Dust Event (PEDE) [96, 97, 102, 103, 104]. One PEDE can cover an area thousands of kilometers wide, spreading over most of the latitudes of Mars. The storms can be very massive with denser dust clouds and can reach the altitudes (as high as 80km) higher than the normal background dust. These storms are so strong that they can have profound effect on the atmospheric composition and circulation. They can act as space elevators by increasing the transport of atmospheric species through the atmosphere leading to their escape. Hence, the Global Dust Storms play a vital role in the environmental evolution of Mars.

1.6 Thermosphere of Mars

'Thermosphere', derived from the Greek word 'Thermos', which means heat, is the third atmospheric layer from the surface of Mars. It is the first layer which is exposed to the solar radiations, and consequently the first one to get heated up by the sun. It is the hottest layer of the Martian atmosphere. The interaction of atmospheric constituents with Ultraviolet (UV) and Extreme Ultraviolet (EUV) causes photoionization of the atmospheric molecules. Thus, it constitutes a major part of the ionosphere of Mars. It is a transition region from a well-mixed atmosphere to the region where the atmospheric gases are diffusively separated. This means, at the thermospheric altitudes, the atmospheric constituents are separated according to their molecular masses and scale heights (temperatures). Thermosphere of Mars starts from the top of the mesosphere which is nearly ˜100 km (known as mesopause) and extends up to the base of exosphere (referred to as exobase). Like mesopause, the altitude of exobase does not have a well-defined boundary but varies with seasons, local time and latitude in the range of ˜160 to ˜220 km [105]. The thermosphere of Mars can be characterized by two main quantities; thermal structure and the composition of the gases that makes up the thermosphere.

1.6.1 Thermal structure

Several observations have added to our knowledge of the thermal structure of thermosphere. This has allowed for validation of many atmospheric models and cross-calibration between instruments and techniques. The thermal structure of Mars thermosphere is similar to that of Earth, yet, is different in several ways. The temperature profile for 100 km-260 km from the surface (comprising of thermosphere and exosphere) is shown in Figure 1.7 (left panel). The temperature profiles are derived using Ar (blue) and N_2 (green) measurements from NGIMS using equation (3) and (4). The exponential increase in the temperature with height, up to approximately ˜170 km, is essentially due to the absorption of solar radiation. However, the atmosphere becomes isothermal above exobase altitude (˜200 km). This mean, in the exospheric region, the temperature variation ceases to change with respect to change in height. The mean exospheric temperature as observed by NGIMS is ˜268 K. The observed temperatures are also validated using Mars Global Ionosphere Thermosphere Model (M-GITM) (red dots) simulations, which gives approximate exospheric temperature as 257 K [4].

1.6.2 Vertical structure

Since the touch down of Viking lander(s) mission, the compositional structure of the upper atmosphere of Mars is well established by several spacecraft missions [106, 107, 7, 108, 109, 110]. Measurements from these missions revealed that the atmosphere of Mars constitutes several molecular and atomic species.CO_2 is the dominant one, O, O_2, Ar, N_2, CO, NO, C, He and N are the other important neutral species. The vertical structure of atmospheric abundance, shown in Figure 1.7 (right panel), show a smooth decrease in densities with increase in altitude. Molecular diffusion allows sorting of atmospheric species in such a way that molecular species, due to heavy masses and smaller scale heights, populate the lower altitudes of the upper atmosphere. The atomic neutrals owing to their light masses and larger scale heights, dominate at higher altitudes. Among all the atomic neutrals present in the upper atmosphere of Mars, atomic O becomes the dominant neutral species above somewhere between 180 km and 270 km [3].

Noble gases (e.g., Ar and He) are the minor species in the thermosphere of Mars. Despite that, the inert nature of these species allows them to remain in atmosphere without interacting with the other species chemically. Helium, owing to its light mass gets easily carried by the winds. Thus, He density can be used to trace the large-scale circulation in the atmosphere of Mars. In addition, Argon does not condense at Mars surface and at-

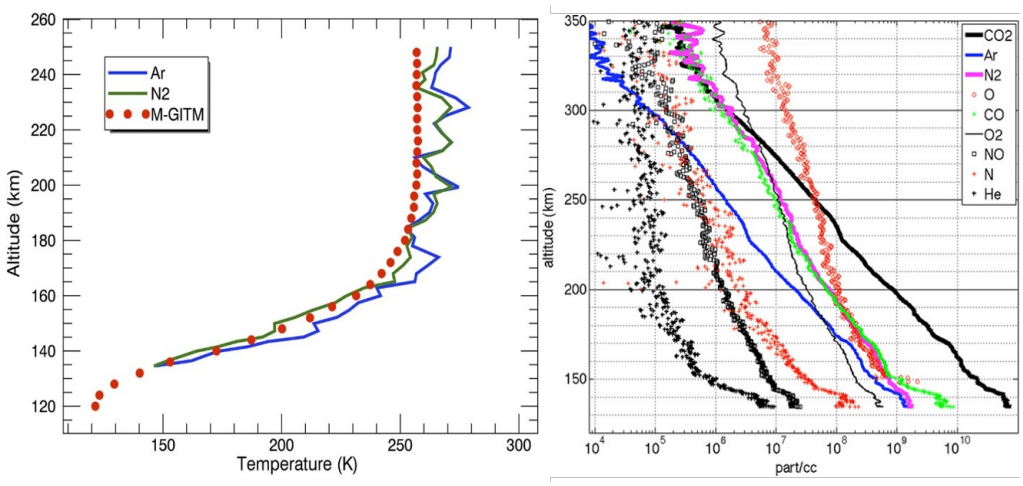

Figure 1.7: (left) Temperature profiles of Mars upper atmosphere using Ar (blue), N_2 (green) measurements from NGIM and modeled using M-GITM simulations (Red) [3]. (Right) Density profiles of atmospheric neutrals as observed by NGIMS [4]

mospheric temperatures [69] Thus, non-reactive species are the most suitable atmospheric constituents to study the spatial and temporal variabilities in the Martian thermosphere. In addition, species such as CO and N_2 can sustain in the atmosphere for longer time due to their longer lifetime. Therefore, these species can also help in characterizing the short-term and long-term variabilities in the Martian thermosphere. Thus, the present study is carried out using densities of such gases as Ar, He and N_2, to bring out thermospheric spatial and temporal variabilities clearly.

1.6.3 Thermospheric variabilities

Thermosphere of Mars is a very complex region as it is coupled to the atmospheric regions above and below it. Thermosphere regulates its thermal structure by balancing the incoming and outgoing solar flux through redistribution of heat through several processes. The primary source of heating of the thermosphere of Mars is the absorption of solar EUV radiations (10 nm-121nm). Since the EUV intensity varies based on local time and solar cycle, the atmospheric thermal structure at the altitude range of 100– 200 km, is closely governed by local time and solar cycle [5]. In addition to this, precipitating particles from the solar wind and solar transient events also produce heating and ionization in the thermosphere of Mars. e.g., [111, 112, 113, 114, 115, 116, 117, 118].

The wavy nature in the densities of CO_2, Ar, and He, observed near periapsis [4, 119, 120], is attributed to gravity waves. Gravity waves, thermal tides and planetary

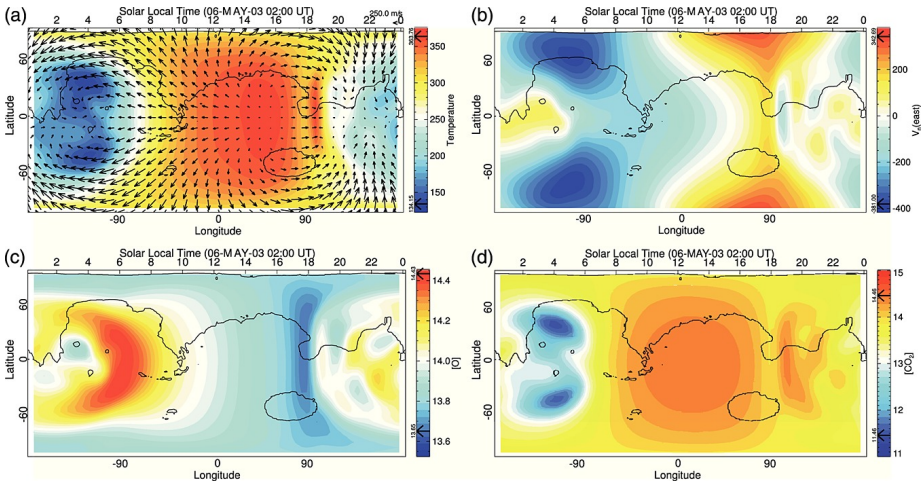

Figure 1.8: Latitude versus Longitude/local time variation of a) Temperature, b) Zonal Winds, c) [O] and d) [CO_2], at 200km, for Ls = 180 [5]

waves originate in the lower and middle atmosphere, propagate towards the upper atmosphere where they deposit energy and momentum at high altitudes causing variations in the structure of the thermosphere [25, 26, 27]. Further, seasonal inflation and contraction [5, 119, 41, 27, 121, 122, 4, 123, 124, 120, 26] lead to the spatial and temporal variations in the thermospheric temperature, composition and circulation as observed e.g., [125] and modeled by global circulation models such as MGITM and LMD-GCM (Figure 1.8), [5, 28]. Occasional heating of the thermosphere by solar flares [29] further complicates the temporal and seasonal variability of the Mars thermosphere.

While dynamical processes have been observed to bring considerable changes to the structure of the thermosphere, dynamical events such as dust storms, occurring in the lower atmosphere, significantly affects the densities and temperatures of the thermosphere [126, 30, 31, 32, 49, 89, 127, 128]. The coupling between the lower atmosphere and thermosphere takes place primarily through the radiative heating of the dust aerosols. The resulting heating and expansion of the Mars atmosphere and subsequent modifications to atmospheric circulation drive the changes in the upper atmosphere e.g., [126, 30, 28, 31, 32]. Although the upper atmospheric changes are observed during all dust storms (section 1.5.2), they are more prominent during planet-encircling dust events (PEDEs) such as the one which occurred in 2018 (PEDE-2018, [31, 32]).

The densities of the Heavy species such as CO_2 and Ar exhibit a general solar zenith angle (SZA) dependent trend, i.e. densities decrease with the increase in SZA [4]. Thermospheric scale heights and temperatures of heavy species have been observed to reach a maximum near perihelion and a minimum near aphelion and show a strong dependence

on long-term changes in the solar flux. On shorter time scales however, local factors such as waves are found to influence the variability. [125] observed strong diurnal variations in the upper atmospheric CO_2 densities and temperatures. They observed that the daytime thermospheric temperatures are maximum and reaches a minimum at the night side of Mars. In addition, [129] reported a temperature enhancement near the dusk terminator in the equatorial and midlatitude region. This enhancement was found to be consistent with the post-dusk dynamical features modeled and discussed by [130, 5]. While the distribution of Heavy species is mostly controlled by the processes that result in dynamical heating and cooling in the thermosphere of Mars, lighter species such as O and He have been observed to exhibit a peculiar behavior compared to the heavy species.

Lighter species such as O and He, owing to the small their masses, get easily carried away by the large-scale winds and get accumulated in the regions of wind convergence. In case of helium, these accumulations are referred to as 'Helium Bulges', at the thermospheric altitudes of Mars. The solar zenith angle (SZA) trend of the He densities show an opposite variation as compared to that of the heavy species, such that densities are found to be enhanced in the night time regions of Mars thermosphere [131, 4]. Seasonal variations in the zonal wind circulation [5] triggers corresponding seasonal variations in the He densities, so much so that the He abundances in the winter polar region are 1–2 orders of magnitude higher than those in the summer polar region. Existence of such a winter bulge has been reported for Earth [132, 133, 134, 135, 136, 137] and Venus [138, 139, 140]. Using the He measurements by the Neutral Gas and Ion Mass Spectrometer (NGIMS) onboard MAVEN, [131] reported the existence of the He bulges in the winter polar nightside of Mars. They found that the He abundance in the northern polar winter nightside is twice that on the northern polar summer nightside. The nightside enhancements in density are a factor of 10–20 larger than the dayside depreciations. These initial observations were found to agree preliminarily with the MGITM modeling results [131]

Homopause altitude is an atmospheric boundary that separates a well-mixed atmosphere from a diffusively separated region. Above homopause the mixing ratio of lighter species in general increases with the increase in altitude [4, 33]. The spatial and temporal variations in homopause altitude [105, 141, 67] affects the relative composition of thermospheric region lying above it. In addition, [142, 143, 105, 144, 145] also calculated total atmospheric loss from the isotopic record using the fractionation between the homopause and the exobase. The spatial and temporal variations at 140 km, in the N_2/CO_2 mixing ratio, have been found to be related to the variation in homopause altitude during day time [67].

1.7 Motivation for this Thesis

As described in the previous sections, the thermosphere of Mars is a very complicated region due to its coupled interaction with forcings from the top as well as the bottom of the region. Not only that, this region finds its importance due to its critical role in the escape of atmosphere to space also [146]. It is a region, where atmospheric constituents can gain sufficient energy, travel to exosphere and ultimately get lost to the space. The energy and momentum deposition by several processes not only act as the catalysts to the escaping processes but also cause spatial and temporal variations in thermospheric composition and temperature. Thus, it is very important to study the spatial and temporal variabilities in the Martian thermosphere.

The thermal and compositional structure of the Martian thermosphere and its variability have been investigated using several remote sensing techniques such as stellar occultation observations from UV SPICAM onboard Mars Express [147, 148] and IUVS onboard MAVEN [149, 150]; solar occultation observations, during solar flare events, from X-ray radiometer RF -15 aboard Phobos 2 [151]; dayglow observations from UV spectrometers onboard Mariner 6,7 and 9 [152, 153]; radio occultation measurements from Mariner 4,6, 7 and 9; Mars 2,3,4 and 6 and Viking(s) orbiter [154, 155, 156, 157, 158]. In addition, Radio occultation experiment aboard MGS, MARSIS aboard MEX have also given valuable information about thermosphere of Mars [159]. However, vertical profiles of thermospheric temperature and densities that are derived using aforementioned techniques are either extended only upto lower thermospheric region of Mars (˜130 km) or have very less altitude resolution.

Mars thermosphere have also been investigated during descent of several spacecrafts (using the accelerometers onboard) such as Viking lander 1 and 2 [160, 161, 162, 163, 164]; the Mars Pathfinder [165, 166]. In addition, Mars Pathfinder's atomic structure instrument [167], during its descent to surface, also provided thermospheric densities and temperatures [164]. Information about the thermospheric environment using accelerometer measurements during the aerobraking phase of MGS, ODY, MRO helped to further our understanding of the complex region [168, 49, 169, 164]. Data from these missions have also helped in developing atmospheric models and improving the aerobraking operations for other missions [170, 171, 172, 173]. In addition, the Phoenix lander [174] and Mars rover missions such as Spirit and Opportunity, Beagle 2, and MSL, have also played prominent roles in understanding the thermosphere of Mars [175, 176, 177, 178, 179]. However, the results from these studies are either limited to a maximum altitude of ˜120 km or have high

uncertainty at high altitudes.

Measurements from the mass spectrometers onboard Viking landers were the only direct measurements of the atmospheric composition that existed for nearly four decades until MAVEN and MOM reached Mars. Viking's measurements provided only two altitude profiles of atmospheric composition and temperature, upto an altitude of 200 km [180, 106]. This essentially implies that for a long period of time, we had no information about how thermospheric composition and temperature varies with solar cycle, seasons and local time. Moreover, the thermospheric variabilities that are discussed in section 1.6.3 do not give a comprehensive view of the spatial and temporal variations in the thermosphere of Mars. Thus, Martian atmospheric variability above an altitude of 100 km remained notoriously understudied.

MAVEN arrived at Mars in September, 2014 [6]. The instruments onboard started useful science operations in early-2015. Since then, there has been a rapid expansion in the knowledge base on the thermosphere region of Mars. In addition, MOM, which was inserted into orbit around Mars in September, 2013 [181], also aims to characterise the upper atmosphere of Mars. In the past 5 years, mass spectrometers NGIMS/MAVEN and MENCA/MOM have provided density and temperature profiles of important atmospheric species (chapter 2) that covers different seasons and regions of Mars above (>100 km) and throughout the Martian years. This extensive coverage provides an exciting opportunity to explore the long and short-term variability of the thermosphere of Mars. In addition, it will be very interesting to see time-correlated measurements for different regions of Mars using multi-spacecrafts measurements.

1.8 Outline of This Dessertation

The objective of this thesis is to study the spatial and temporal variations in the thermosphere of Mars.In Chapter 2, we describe all the instruments and models we used to cary out this research work. All the data used in this dessertation is also discussed in chapter 2. In Chapter 3 we study the local time variations in Ar density in the upper atmosphere of Mars using measurements from NGIMS. This study is done for an altitude region of 160 km – 200 km. In addition, we have investigated latitudinal and seasonal variations in the Ar density and the annual variability in the Ar densities by correlating with the solar F10.7 cm flux. In Chapter 4 we remove the possible contribution of seasonal bias to the local time variations, observed in chapter 2, by using simultaneous measurements from MAVEN and MENCA. In addition, we also study the effect on PEDE-2018 on the observed variabilities.

In Chapter 5 we investigate the latitudinal and local time variations in He densities in the thermosphere of Mars. In addition, we also compare the observed densities and horizontal winds with MGITM model simulations of He densities and zonal winds. In Chapter 6 we study the local time, seasonal and latitudinal variabilities in the mixing ratios of important neutrals in the Martian thermosphere, and also investigate the response of mixing ratios to the PEDE-2018. Finally, in chapter 7 we summarize the uniqueness of this research and suggest directions for the future work in these areas.

Chapter 2

Instruments, Data and Methodology

2.1 Introduction

Historically, Mars has been studied using ground based telescopes from Earth, several flyby and orbiter missions from outer space, and by landers and rovers on its own surface. At the time of writing this thesis, there are three robotic Mars rovers, one lander and seven orbiters that are investigating the surface and atmosphere of Mars. The present thesis uses data from two recent spacecraft that have been measuring the Mars neutral and space environment viz., NASA's MAVEN and ISRO's MOM spacecraft. As mentioned in section 1.6, prior to the arrival of these two missions, the available measurements of the Mars upper atmosphere were very limited and hence, the thermosphere of Mars remained under-studied. However, after the arrival of these spacecrafts at Mars, there has been significant increase in the available data on a global scale, which helped planetary science community in revealing interesting facts about the Mars upper atmosphere, particularly the thermosphere. Thus, MAVEN and MOM are among the most influential Mars exploration missions that helped in understanding the structure and composition of the Martian thermosphere; its interaction with lower atmosphere, exosphere and solar radiations and, its short- and long-term variabilities.

The work presented in this thesis is based on measurements from two mass spectrometers, namely NGIMS and MENCA onboard the MAVEN and MOM spacecraft, respectively. Mass spectrometry is a technique that provides the concentration of neutral and ion species as a function of their respective masses. In most of the mass spectrometers, at first the species (if neutral) are ionized in an ionization chamber. These ions are then focussed into a separation region, where they are separated according their charge and mass. The ions can be separated using electric or magnetic fields. The most common mass spectrometry techniques are Time-of-Flight mass spectrometry, Quadrupole mass spectrometry and

Ion-Trap mass spectrometry. Both NGIMS and MENCA are Quadrupole Mass Spectrometers. In quadrupole mass spectrometers, ions extracted from the ionizer region are directed along the axis of a set of four parallel rods, precisely separated and aligned, to produce a nearly perfect hyperbolic field. With just the right combination of radio frequency (RF) potential and direct current (DC) potential, an ion, with just the right mass to charge ratio (m/q), will be directed through the rods to an ion collector (usually a Channel Electron Multiplier or a Faraday Cup). All other mass to charge ratios will be rejected long before the ion is collected. By carefully scanning the RF and DC potentials, a mass spectrum, consisting of a number of ion current peaks, may be generated, where species are separated by passing them through an alternating electric field region. A representative block diagram of a mass spectrometer and a sample mass spectrum is shown in Figure 2.1

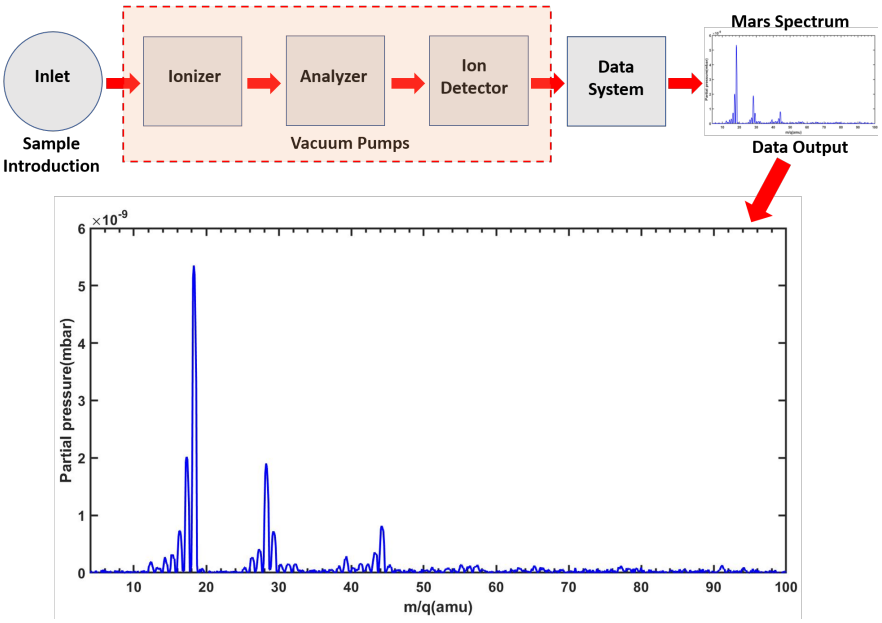

Figure 2.1: Schematic block diagram of a mass spectrometer (top) and a sample mass spectrum (bottom) generated during lab calibrations of MENCA

The organization of this chapter is as follows: section 2.2 presents the details about the MAVEN and MOM missions, the NGIMS and MENCA mass spectrometers that are used to carry out the research of this thesis are discussed in section 2.3. Measurements (datasets) from these two mass spectrometers are described in section 2.4. Sections 2.5 and 2.6 present the methodology of deriving the final data products such as densities, scale heights (temperatures), and homopause altitudes from the initial products of NGIMS and MENCA, respectively. Finally, section 2.7 presents a description of the university of Michigan M-GITM model that is used to compare with the spacecraft measurements. The aux-

iliary datasets that aid the interpretation of the mass spectrometer results are discussed in section 2.8.

2.2 Mars Missions

2.2.1 MAVEN

NASA's Mars exploration spacecraft MAVEN was launched on 18th November, 2013 and entered the orbit around Mars on 22nd September, 2014 [6]. The primary goal of the mission is to explore the upper atmosphere of Mars and to investigate its interactions with the solar wind and radiation so as to understand the processes that led to the loss of atmospheric volatiles to space. To achieve its goals, MAVEN mission is designed in such a way that it measures the entire Mars space environment, right from the upstream solar wind region to the thermosphere. In each orbit, the suite of instruments on MAVEN measure densities of various neutral and ion species, energetic electrons and ions, densities and temperatures of thermal electrons, and electric and magnetic fields. All these, along with the outputs of GCMs, are helpful to quantify the escape rates of the Mars volatiles to outer space. Thus, the ultimate goal of MAVEN is to get an insight into the history of Mars climate and atmosphere, liquid water, and its habitability.

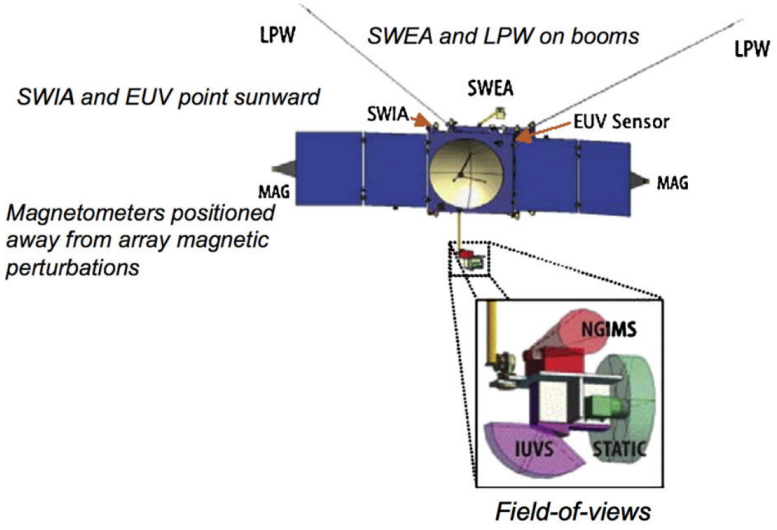

Figure 2.2: Location of Instruments on the MAVEN Spacecraft and Articulated Payload Platform (APP) [6]

To meet its science goals, MAVEN is housed with a set of nine instruments (Figure 2.2)

that are grouped into three science packages: Particles and Fields Package, Remote Sensing Package and the Mass Spectrometry Unit (Table 2.1). The Particles and Fields Package includes the Solar Wind Electron Analyzer (SWEA) [182], the Solar Wind Ion Analyzer (SWIA) [183], Solar Energetic Particles (SEP) [184], Suprathermal and Thermal Ion Composition Analyser (STATIC) [185], Langmuir Probe and Waves (LPW) [186], the Extreme Ultraviolet (EUV) Monitor [187] and Magnetometer (MAG) [188]; Remote Sensing and Mass Spectrometer packages includes Imaging Ultraviolet Spectrograph (IUVS) [108] and NGIMS [7], respectively. While each these instruments are designed to measure atmospheric abundances of specific energy and at certain region of altitudes, MAG provides information about the direction and magnitude of the background and crustal magnetic fields and EUV measures the solar irradiance at three wavelength bands. Among the nine sensors that housed on a three-axis stabilized spacecraft, three sensors: IUVS, NGIMS and STATIC, are mounted on the Articulated Payload Platform (APP) (as shown in Figure 2.2). This allows them to look in any direction independent of the orientation of the spacecraft (RAM). In addition, Radio Occultation Science Experiment (ROSE) [189] onboard MAVEN can provide the electron density profiles of Mars ionosphere for the altitude region of 100 – 500 km. However, the present thesis uses the neutral density measurements from NGIMS to characterize the thermosphere of Mars.

Table 2.1: Packages and instruments onboard MAVEN

Package name	**Instrument name**
Particles and Fields Package	Solar Wind Electron Analyzer (SWEA)
	Solar Wind Ion Analyzer (SWIA)
	Solar Energetic Particle instrument (SEP)
	Suprathermal and Thermal Ion Composition instrument (STATIC)
	Langmuir Probe and Waves (LPW)
	Magnetometer (MAG)
Remote Sensing Package	Imaging Ultraviolet Spectrometer (IUVS)
Mass Spectrometry instrument	Neutral Gas and Ion Mass Spectrometer (NGIMS)

MAVEN orbits Mars in an elliptical orbit which is inclined at 75° [6]. The periapsis of the MAVEN spacecraft was at an altitude of ˜150 km and apoapsis at 6,220 km. However, in February, 2019, MAVEN's orbit was changed by performing aerobraking and the apoapsis altitude of MAVEN's spacecraft was lowered to an altitude of ˜4,400 km and periapsis altitude below 132 km. In addition, some targeted campaigns (deep-dip, wind campaign, and etc) are performed. During these campaigns the periapsis altitude can be as low as ˜120

km and apoapsis altitude can be as high as ˜1200 km [3, 190]. The average time taken by MAVEN to complete one orbit around Mars is ˜4.5 hr and it orbits around Mars for more than five times in one Martian day (sol). The apoapsis altitude, orbital period, and orbital inclination are selected in such a way that all local solar times and all latitudes between +75º to -75º are covered.

2.2.2 MOM

ISRO's first interplanetary mission to Mars – the Mars orbiter Mission (MOM) was launched in November of 2013 and inserted into the Martian orbit in September, 2014 [181]. The primary science objectives of the MOM are to explore the surface features of Mars by studying the morphology, topography and mineralogy, study the atmospheric composition of Mars (including methane), and to understand the dynamics of the upper atmosphere of Mars and its response to solar winds and radiations. To achieve its science goals, MOM is equipped with five science experiments. The five instruments are: Lyman Alpha Photometer (LAP) [191], Methane Sensor for Mars (MSM) [192], Mars Exospheric Neutral Composition Analyser (MENCA) [193], Thermal Infrared Imaging Spectrometer (TIS) [194] and Mars Colour Camera (MCC) [195]. In the present study, we use measurements from MENCA to characterize the thermosphere of Mars.

MOM's orbit around Mars in a highly elliptical, with a periapsis between ˜260- 400 km and Apoapsis at ˜71,000 km [181]. The orbital period of MOM is ˜72 hours. Due to this, it is able to complete one full orbit around Mars in nearly three Martian days. In the present study we use measurements taken during 5-29, June of 2018 during which MOM measured the Mars upper atmosphere with a period of ˜2 days. During this time the periapsis altitude of MOM was below 165 km which helped in investigating the thermosphere of Mars.

2.3 Instruments

2.3.1 NGIMS

The Neutral Gas Ion Mass Spectrometer [7] is an instrument onboard MAVEN which is designed to investigate the structure and composition of the upper atmosphere of Mars. It is a quadrupole mass spectrometer with a mass range 2-150 amu and resolution of 1 amu. It measures neutral abundances of He, N, O, CO, N_2, NO, O_2, Ar, and CO_2 in the upper atmosphere of Mars. It also measures altitude profiles of dominant ion species such as O_2+,

CO_2+, NO+, O+, CO+, C+, N_2+, OH+, and N+ along the spacecraft track. In addition, NGIMS secures isotopic ratios of $^{13}C/^{12}C$, $^{18}O/^{16}O$, $^{15}N/^{14}N$, $^{40}Ar/^{36}Ar$, $^{38}Ar/^{36}Ar$. All the measurements are carried out in inbound as well as outbound trajectory of the MAVEN orbit within 500 km from periapsis. NGIMS operations are carried out by alternating between a closed and an open source to collect and sample atmospheric species [196, 7]. In the closed source mode, surface nonreactive species such as Ar, He, CO_2, N_2, and CO are measured, and this mode of operation is carried out on every orbit. The open-source mode, on the other hand, is used alternatively to measure the reactive neutral species and ions (e.g., O, N, etc.).

During the sampling process in NGIMS, the atmospheric species pass through the ionization, mass separation, and detection regions (Figure 2.3). In the ionization region, an electron beam of 75 eV is used to ionize ambient species by an electron impact ionization (EI) technique. These ionized species are then flushed into a mass separation region for sorting according to their mass-to-charge ratio. For this purpose, NGIMS uses a quadruple ion-mass filter, that consists of four hyperbolic rods to which radio frequency and static currents (DC) are applied alternately switching between the two sources. The use of two separate sources also results in better instrument calibration. The counts detected for each mass channel are processed for background, instrument sensitivity, and ram enhancement correction to derive atmospheric abundances [196, 7]

In its nominal orbit, NGIMS measures atmospheric abundance between periapsis and up to an altitude of 500 km by maintaining its field of view (FOV) within ±2° of spacecraft's ram direction [7, 4]. Furthermore, between April 14, 2018 and November 12, 2018, NGIMS performed 19 campaigns dedicated to Ar measurements up to 1,200 km enabling characterization of the exospheric region [190]. During the year 2016, a wind mode was introduced to the instrument's operation [197]. In this new mode, APP is moved ±8° off the ram axis in local vertical and local horizontal planes, which enables NGIMS to measure direct along-track and across-track winds (horizontal neutral winds) in the Martian upper atmosphere [197]. During the wind mode of operation, NGIMS normal science operations (measurement of abundances) are paused and modulations in CO_2 abundance alone are measured. Each wind campaign lasts for 2–3 days and the subsequent campaigns are separated by one to several months. During each campaign NGIMS collects wind measurements in a 5–10 set of MAVEN orbits that correspond to nearly the same sets of local time, latitude and altitudes. The winds are generally measured between ˜140km and ˜240km with a ˜30 s cadence. The magnitude of winds can vary by ±20m/s and ±6m/s along and across MAVEN track respectively, owing to errors in data retrieval processes [197].

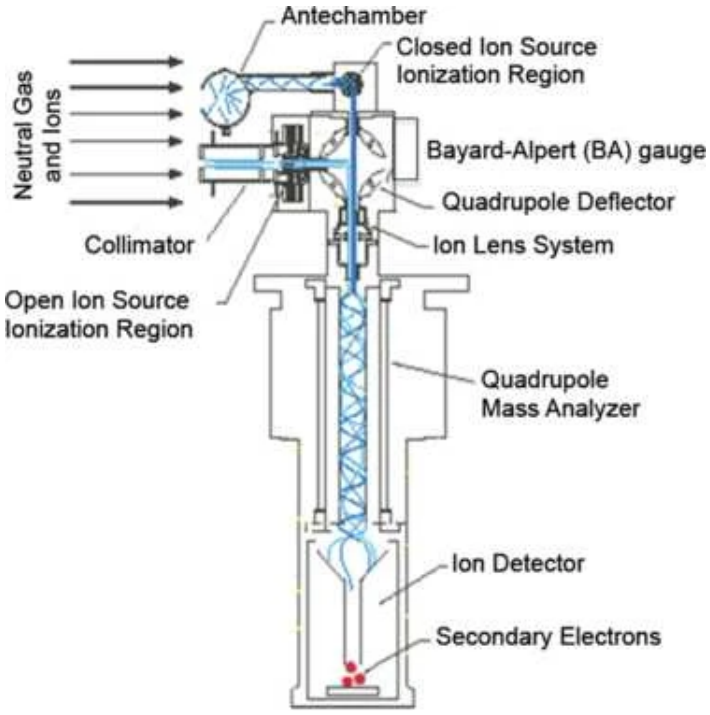

Figure 2.3: Schematic of sampling process of NGIMS [7]

2.3.2 MENCA

Mars Exospheric Neutral Composition Analyzer (MENCA) [193] is one of the five science experiments onboard MOM. It is a quadrupole mass spectrometer-based instrument which is designed to measure the neutral composition of thermosphere-exosphere of Mars. MENCA secures neutral density profiles of such dominant species as CO_2, Ar, N_2+CO and O, with the mass range of 1-100 amu and unit mass resolution. It consists of an open ion source where species are ionized using electron impact technique with electron energy ˜70 eV, a quadrupole mass filter to separate species according to their charge-to-mass ratio. In addition, MENCA consists of a Bayard Alpert (BA) gauge that measure the total pressure in the source region. It helps in deriving the absolute densities of the atmospheric species from the observations. In the detection region, MENCA houses a Channel Electron Multiplier and Faraday Cup to improve the sensitivity and amplify the low currents that corresponds to trace gases. The output of MENCA is the atmospheric partial pressure of the species. The method of derivation of density from the partial pressure is described in [193, 109, 110] and is explained in section 2.5.1. More details about MENCA and its data can be found in [193, 109, 110]. A detailed description on the sources of errors is also provided in the supporting information of [109].

2.4 Observations from NGIMS and MENCA

The data used in this thesis are He, Ar, N, O, and CO_2 measurements from NGIMS and O, Ar, and CO_2 measurements from MENCA. Due to outgassing and higher background noise in the outbound portion of MAVEN and MOM orbits, the analysis of the measurements from both instruments is restricted to Inbound portions of their trajectories. NGIMS measurements used in Chapter 3 are from Level 3 (Version 6) and key parameter (KP) data sets (Version 14), from January 2015 to November 2018, which span the Martian years (MYs) 32-34. Here, Level 3 data provide the derived scale heights and temperatures of dominant species, such as CO_2, Ar, O, etc. [196]. However, NGIMS measurements used in Chapter 5-6 are from Level 2 (Version 08) data sets which span MY 32-35. The Level 2 data sets provide derived abundances of dominant neutral and ion species in the atmosphere of Mars. In Chapter 4 density measurements from NGIMS and MENCA corresponds to 05, 08, 10, 13, 16 and 29 June, 2018. While NGIMS measurements are from Level 2 data set (Version 08, revision 06), MENCA measurements are from Level 01 data sets that contains mass spectrums of raw partial pressure of each species. Thus, densities were derived following a systematic procedure as discussed in section 2.6 and in [193, 109, 110]. In addition, the wind observations, used in Chapter 5 are from version 06_r01 data sets of Level 3 data products. The wind observations are from 41 campaigns that span the period from 2016 to 2020. However, the winds measured during both the inbound and outbound segments are used. Finally, Measurements from EUV/MAVEN and computer simulations of M-GITM have also been used to compare and validate the results.

The aforementioned data sets from NGIMS, are publicly available at MAVEN Science Data Center (https://lasp.colorado.edu/maven/sdc/public/) and the NASA Planetary Data System (https://atmos.nmsu.edu/data_and_services/atmospheres_data/MAVEN/ngims.html).
The data sets from MENCA are available at the Planetary Data System at the Indian Space Science Data Centre https://mrbrowse.issdc.gov.in/MOMLTA/ and can be obtained by registering at the link. In addition, the data corresponding to the results presented in Chapter 4 and 5 are publicly available on the Mendeley data repository http://dx.doi.org/10.17632/dmn8mjs6jw.1 [90] and (https://data.mendeley.com/datasets/jvzcpt65mh/1) [198], respectively. Finally, M-GITM datacubes for the 4-cardinal seasons during MY33, that are used in Chapter 5 are archived on the University of Michigan Deep Blue Data repository.

2.5 Parameter extraction from NGIMS

The measurements of atmospheric densities from NGIMS that are used in the present study are available publicly in level 2, level 3 and Key Parameters data sets as discussed in section 2.4. Therefore, only the methodology to derive scale heights (H) and Temperatures and Homopause altitudes from NGIMS measurements are discussed in this section.

2.5.1 Derivation of scale heights and temperatures

The scale heights (H) and Temperatures are computed by fitting a linear curve to the logarithmic of density profiles, between homopause/periapsis (zo) and the exobase/reference height (z) (as shown in Figure 2.4). The temperatures (T) are derived from the scale heights using the equation (1.4). Here, no is the density at zo.

$$n = n_o exp(\frac{-z - z_o}{H}) \tag{2.1}$$

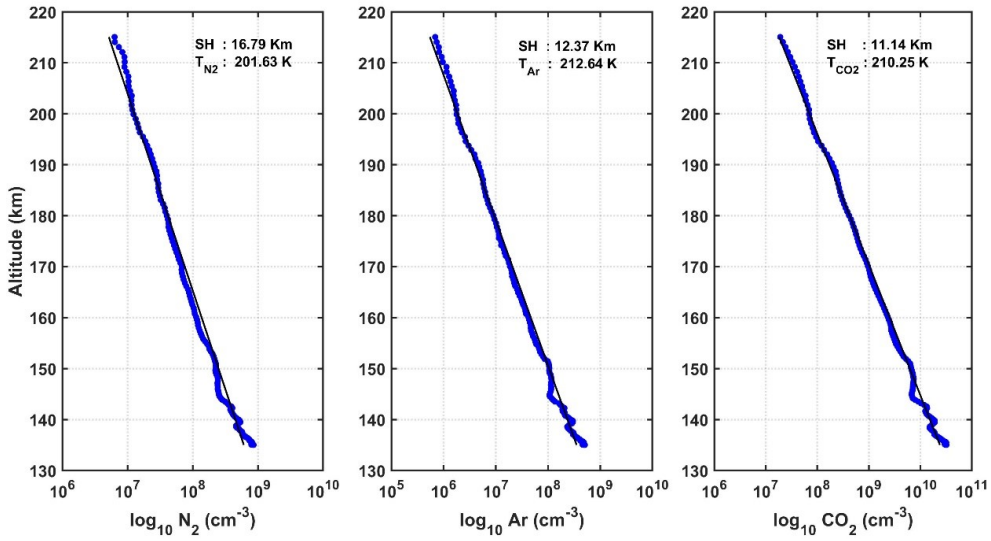

Figure 2.4: Altitude profiles of N_2 (left), Ar (middle) and CO_2 (right). The blue dots represents the densities measured by NGIMS and black lines represents the linear fit to the densities.

2.5.2 Derivation of Homopause altitudes

In chapter VI, mixing ratios of various species are compared with variations in the Homopause altitudes. Here, the homopause altitudes are derived using NGIMS data by following a methodology which similar to that of [105]. The homopause altitudes are derived in three steps that are explained below:

The first step involves the derivation of the exobase altitudes. Exobase is defined as a transition region from a strongly collisional to collision less region of the atmosphere. It is a critical altitude at which the mean free path of an upward moving particle is equal to one pressure scale height. Mean free path (λ) is mathematically related to collisional crossection (σ) of a particle as,

$$\lambda = \frac{1}{n\sigma} \tag{2.2}$$

where, n = number density of the atmospheric species. For the present study, we use $\sigma = 3 \times 10^{-15} cm^2$, which is collisional crossection of Ar with CO_2 [199, 200] and number density of the dominant species (CO_2) in the atmosphere of Mars. To derive the exobase altitude, we integrate the $n * \sigma$ downward from very low-density region (high altitudes). The altitude at which the integrated value becomes 1 is selected as exobase altitude (as shown in Figure 2.5, pink dotted line).

In the second step Homopause attitudes are derived. Homopause is an altitude region below which the atmosphere is well mixed. Thus, all the species exhibit same scale heights. We derive the homopause altitude by taking ratio of N_2 and Ar density profiles between the periapsis and the exobase altitudes derived in first step. Since MAVEN periapsis never reaches homopause altitude, we fit the log(N_2/Ar) profile with a linear function and then extrapolate it downwards (as shown in Figure 2.5 black line). The altitude where the ratio N_2/Ar becomes equal to the nominal value measured by Mars Science Laboratory, which is 1.25, is selected as homopause altitude.

2.6 Data retrieval from MENCA

In MENCA the atmospheric abundance is detected in the form of atmospheric partial pressure of the species. In each mass sweep of MENCA, a raw spectrum that contains the relative abundances of different species in arbitrary units is obtained. Corresponding to each raw spectrum file, a value of the total pressure is also measured by a Bayard Alpert (BA) gauge. The raw spectrum is such that there are nine data points per amu with a scan

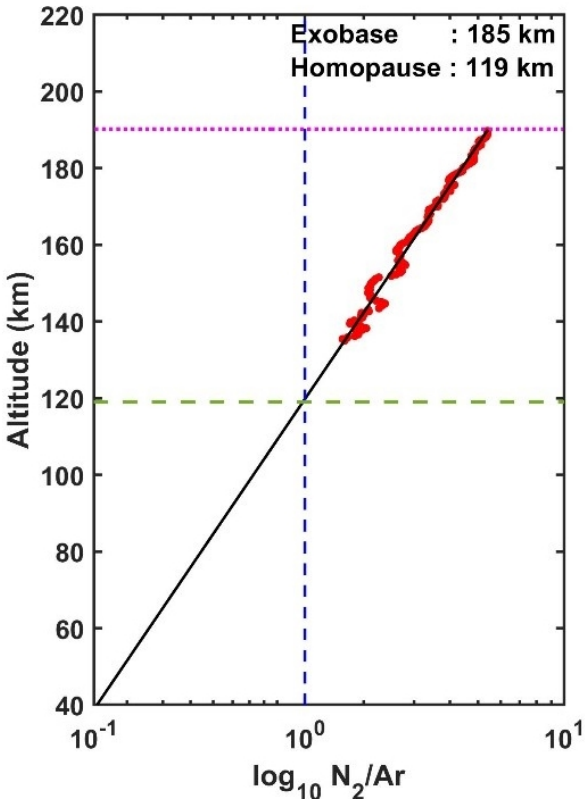

Figure 2.5: Represents the methodology followed to derive the homopause altitudes. Here, the red dots represent the altitude variation of N_2/Ar ratio and black line represents the linear fit to the ratio which is extrapolated towards the lower altitudes. Blue dashed lines mark the value where N_2/Ar = 1. Pink line represents the derived Exobase altitude and green line is shown to represent the derived homopause altitude derived by taking the crossing point of N_2/Ar=1 and linear fitted line. The data presented in the Figure corresponds to the MAVEN orbit number #713

rate of 48 points per second. Figure 2.6 show an example of a mass spectrum for amu 33 to amu 42 as obtained on 5 June, 2018. The range 33 amu to 42 amu is shown only to highlight the Argon-40, which is used to study the local time variations in thermosphere in Chapter 4. In Figure 2.6, the raw data highlighting the nine points that constitute the Ar peak are plotted in red color.

The actual partial pressure is obtained by multiplying a total pressure-dependent normalization constant with the raw partial pressure, after incorporating the correction factors. The factors are Electron Multiplier Gain (EMG) correction, Quadrupole Mass Discrimination (QMD) correction and the gas-dependent relative sensitivity factors. The details about the calibration can be found in [193, 109]. The method used to obtain the absolute mass spectrum, background subtraction and the conversion of the corrected partial pressure to

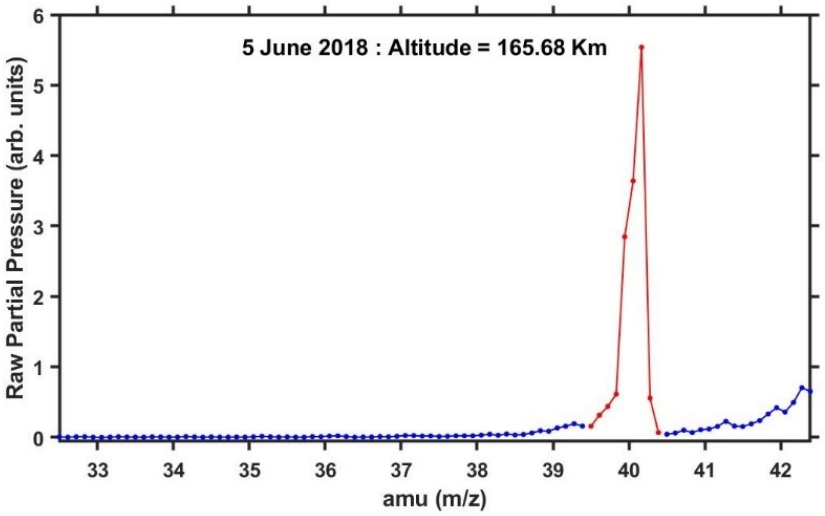

Figure 2.6: Raw Spectrum obtained by MENCA on 05 June, 2018 for the mass range of 33 amu – 42 amu, at ˜165 km

the absolute number density are the same as given in [193, 109, 110]. An example of the corrected mass spectrum observed on 05 June 2018 is shown in Figure 2.7. This is obtained after implementing all the above corrections. Note that the partial pressure of Ar is smaller than the major constituents such as amu 44 (CO_2). To highlight Ar, we show the partial pressures from amu 33 to amu 42 in the bottom panel of Figure 2.7 which is similar to top panel of Figure 2.7.

Figure 2.8 shows the temporal variation of corrected partial pressures of Ar observed on 05 June, 2020. Here a five-point running average is applied on the original data and the smoothed data is used for further analysis. The enhancement of Ar partial pressure towards to the periapsis is apparent in Figure 2.8. The mean background levels in the inbound and outbound segments (shown with black dashed lines) are much smaller than the partial pressure at the periapsis. Also shown in the Figure 2.8 is the 2σ level of the background (blue dashed lines). The points that are clearly above this level are used for obtaining the Ar densities. Since the background and 2σ levels vary from day to day, we restrict our analysis to altitudes < 220 km, which are always much above these levels.

In addition, the partial pressures are corrected for the effective pressure enhancement due to the spacecraft velocity. This ram enhancement factor is given by equation (2.3) by [201]

$$R = \frac{v_s \cos\alpha + v}{v} \tag{2.3}$$

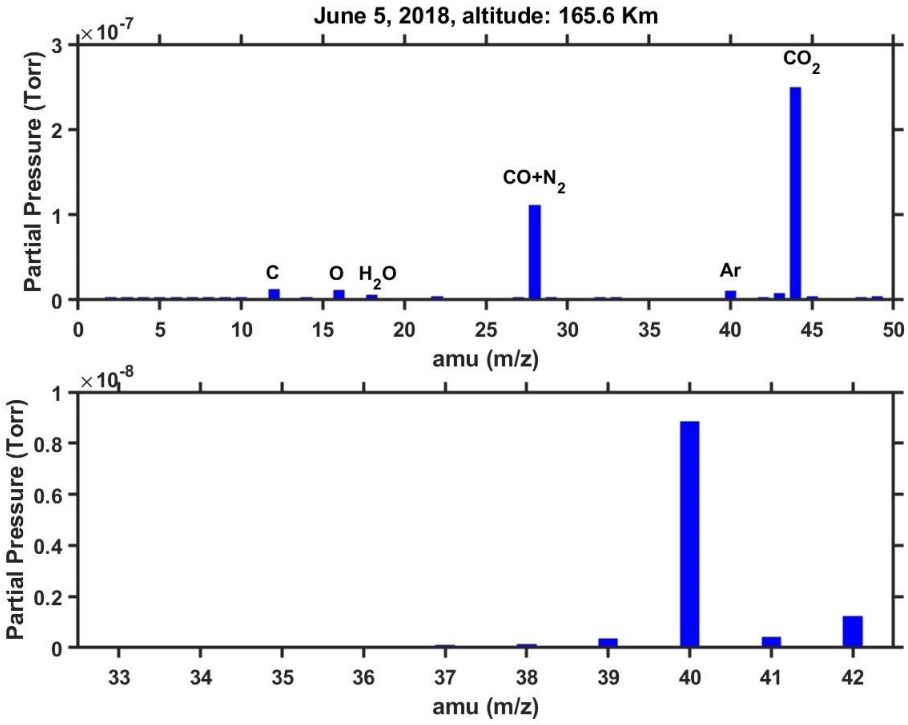

Figure 2.7: (top) An example of the mass spectrum observed by MENCA on 05 June 2018 that shows all important neutral species between 1-50 amu. (bottom) Same as above, but shown only for amu between 33 and 42 to highlight Ar peak (amu 40).

Where vs is the spacecraft velocity, α is the angle between the sensor axis and the spacecraft velocity vector, and v is the average thermal speed of the species. At the periapsis, the MOM spacecraft has an average velocity of ˜5 km s-1. After these corrections, the total uncertainty in the number density of Ar from MENCA is estimated to be < 50% [109]. More details about MENCA and its data can be found in [193, 109, 110]. A detailed description on the sources of errors is also provided in the supporting information of [109].

The neutral densities are derived from the corrected pressure profiles using barometric law (equation 1.2). A sample derived altitude profile of Ar density is shown in Figure 4.3a. The scale heights (H) and Temperatures are then computed using the method as explained in section 2.5.1. The computed SH and Temperatures are show in Table 4.1.

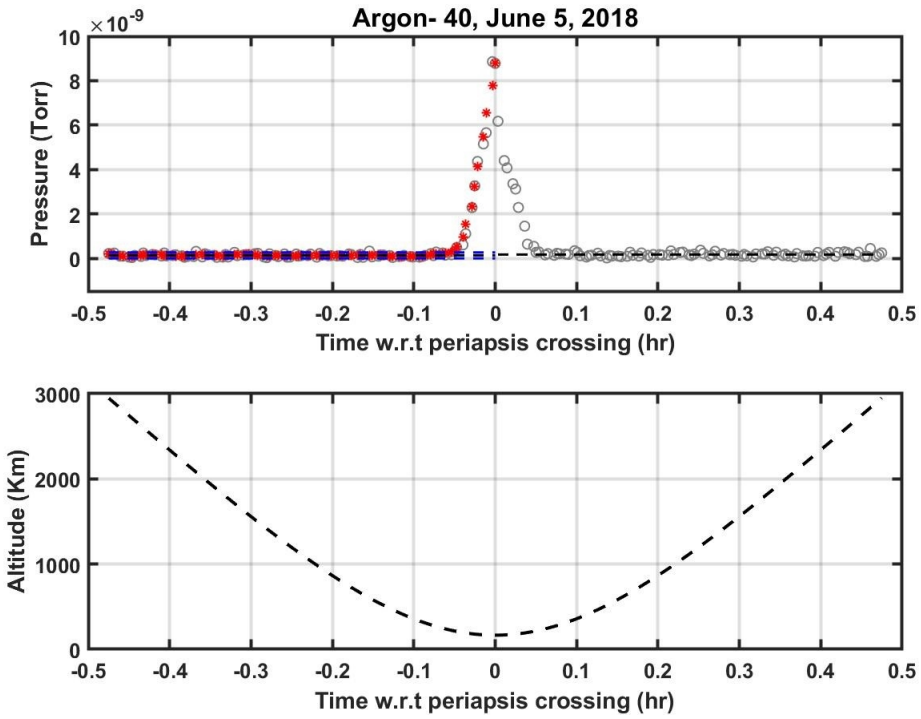

Figure 2.8: (top) Temporal variation of the partial pressure of Ar observed by MENCA on 05 June 2015 (Ls=187.8º). The time in the x-axis is given in hours with respect to the time of periapsis crossing. The grey circles represent the amu 40 spectral data points. The red stars represent the data points after a smoothing using a 5-point running average. The dashed black lines represent the mean background levels in the inbound and outbound legs and the dashed blue lines represent the 2σ standard deviation of the original background data points of the inbound segment.

2.7 Mars Global Ionosphere Thermosphere Model (M-GITM)

M-GITM is essentially a modified version of the terrestrial GITM to fit with the Martian environment using the Mars fundamental physical processes. M-GITM incorporates the key radiative processes and contains prognostic equations for ion-neutral chemistry of the Mars upper atmosphere. The modern M-GITM is a whole atmospheric model that can simulate the thermal, compositional, and dynamical structure of the Mars atmosphere from the ground to ˜250 km. The model has 5 $\times$ 5° horizontal resolution and 2.5 km vertical resolution, and is normally run at 2s time steps. Model physics and simulated features of the upper atmosphere (above ˜80 km) are stressed in most applications of the M-GITM model thus far.

Unlike the Earth GITM code, the new M-GITM code currently simulates the conditions of the Martian atmosphere all the way to the surface [5]. For the Mars lower atmosphere (˜0-80 km), a state-of-the-art correlated-k radiation code was adapted from the NASA Ames Mars General Circulation Model (MGCM) [202]. This provides solar heating (long and short wavelength), seasonally variable aerosol heating, and CO_2 15-μ m cooling in the local thermal equilibrium (LTE) region of the Mars atmosphere (below ˜80 km). In addition, dust opacity distributions are typically prescribed based upon empirical dust opacity maps obtained from several Martian years of measurements e.g., [100, 94, 95]. For the Mars upper atmosphere (˜80–250 km), a modern CO_2 Non-Local thermodynamic equilibrium (NLTE) 15-μ m cooling scheme has recently been implemented e.g., [203], along with MAVEN Extreme Ultraviolet Monitor (EUVM) L3 solar EUV and UV fluxes taken from the Flare Irradiance Spectral Model for Mars (FISM-M) empirical model outputs on a daily cadence [204]. Subsequently, M-GITM thermospheric heating, dissociation and ionization rates are simulated at each time step e.g., [5]. Corresponding prognostic fields for neutral temperatures, neutral densities (CO_2, CO, N_2, O, O_2, He, Ar, and N_4S), and photochemical ion densities (CO_2+, O_2+, O+, NO+, and N_2+), plus 3-component neutral winds are computed on a three-dimensional regular grid. For application in this paper, FISM-M fluxes are used for driving new M-GITM simulations for the four-cardinal seasons spanning MY33 (Ls = 0°, 90°, 180°, and 270°).

On several occasions, a suite of M-GITM simulations have been compared successfully with MAVEN NGIMS, IUVS, and Accelerometer measurements e.g., [205, 5, 131, 129, 206]. Both remote and in-situ measurements are included in this extensive set of observation-model comparisons and model validation studies. Observation-model comparisons generally reveal that: (a) the M-GITM code well captures the basic dayside density variations of key neutral species and (b) M-GITM temperatures also closely match NGIMS and IUVS derived temperatures at low solar zenith angles (SZA). Furthermore, initial helium density distributions from early NGIMS data sets [131] are compared to M-GITM predictions at 180 km. Even with limited data sampling, the basic observed features are simulated with significant helium bulges on the nightside. Nevertheless, [206] have reported that M-GITM versus MAVEN ACC mass density comparisons can be quite good from noon to the dusk terminator, but are poor from midnight toward the dawn terminator. The latter is likely due to incomplete M-GITM physics addressing gravity wave processes impacting global winds and the thermospheric circulation patterns throughout all seasons.

M-GITM predictions are used to compare with the observations from NGIMS in Chapter 5. The simulated He densities and horizontal winds are used as reference to explain the

variability in He densities and neutral winds that are observed by NGIMS. The He densities and zonal winds output from M-GITM are simulated for four Martian seasons: Ls = 0°, 90°, 180°, and 270° and correspond to the MY 33 nominal dust conditions. The seasons considered here correspond to a band of ±45° centered at each seasonal cardinal point (Ls = 0°, 90°, 180°, and 270°). M-GITM datacubes for the four-cardinal seasons during MY33 are archived on the University of Michigan Deep Blue Data repository [207].

2.8 Solar and Dust Indices

Solar Extreme Ultraviolet (EUV) radiations that are emitted in the wavelength range of 0.1 nm -190 nm are quickly absorbed by the Mars thermosphere. This leads to heating and ionization in the region. EUV radiation changes by a factor of 10 over one solar cycle. This produces similar variability in the upper atmospheric temperatures and densities. Solar radio flux at 10.7 cm, also known as F10.7 Index, is often used to investigate the solar activity dependent variabilities. In the present thesis, we use measurements from EUV monitor onboard MAVEN to study the annual variability of the thermosphere. The EUV monitor instrument [187] is a part of LPW suit aboard MAVEN. EUV monitor measures solar emissions in three separate wavelength bands, soft X-ray (0.1–7 nm), EUV (17–22 nm), and Lyman-α (121–122 nm). The Measurements used from the EUV monitor (In Chapter 3) spans Martian Year (MY) 32-34.

Dust plays a key role in the spatial and temporal variability of Mars thermosphere. Mars dust can absorb solar radiations at visible and infrared wavelengths. (For e.g., 0.67 μm in visible and 9 μm in infrared) wavelength. Thus, to estimate the amount of dust aerosols present in the atmosphere, several optical methods are used to measure the dust opacity of the atmosphere of Mars. One of the important parameters to estimate the amount of dust present in the atmosphere is Column Dust Optical Depth (CDOD). The CDOD acts as a tracer of lower atmospheric dust activity such that the largest values of CDOD represent the peak of the dust activity. In the present study (In Chapter 4) we use the CDOD dataset which is a gridded combination of dust opacity nadir observations by the Thermal Emission Spectrometer (TES) aboard Mars Global Surveyor, the Thermal Emission Imaging System (THEMIS) aboard Mars Odyssey, and limb observations by the Mars Climate Sounder (MCS) aboard Mars Reconnaissance Orbiter (MRO) [100]. We use the dust scenario data set corresponding to the global dust storm that occurred in Martian Year 34 (PEDE- 2018) [100].

2.9 Uncertainity and Errors

The sources of error for deriving the number density using measurements from NGIMS and MENCA are detailed in [196] and [109], respectively. The total uncertainty in the number density from MENCA is estimated to be less than 50 percent [110]. The 1 σ error values in Ar scale heights and temperatures (used in chapter 4) that are derived from MENCA and NGIMS measurements are shown in Table 4.1 and Table 4.2 respectively. The homopause altitudes shown in figure 6.5 are derived using a similar methodology as used by [105]. Homopause altitude is basically a transitional region from a well-mixed lower atmosphere to diffusively separated atmosphere. However, the homopause altitudes shown in Figure 6.5 are derived by assuming that homopause altitude is a fixed altitude and not a gradational region. This spares the possibility of physical errors or uncertainties except the errors induced due to fitting procedure followed here. To reduce such statistical error, only those values are shown that are derived with a discrepancy measure (goodness of fit) of 85% and above. Using this method the mean homopause altitude is calculated as 108 km with the mean uncertainity of $\pm$ 10% in the homopause altitudes.

Chapter 3

Dawn-Dusk Asymmetries in the Martian Upper Atmosphere

In this study, we report the first comprehensive observations of local time asymmetries in densities and scale heights (temperatures) of the Martian upper atmosphere (between 150 and 300 km) measured by the Mars Atmosphere and Volatile Evolution mission/Neutral Gas and Ion Mass Spectrometer. For this purpose, we use the densities and temperatures of Ar. In general, the daytime densities and temperatures are greater than the nighttime values. The maximum and minimum values, however, are observed at the dusk and dawn terminators, respectively. An enhancement at the dusk terminator is persistently observed at all altitudes; however, the time of the peak enhancement shifts toward sunlit hours with increasing altitude. At the dawn terminator, a minimum in density is observed at altitudes of 150–170 km. At higher altitudes, the minimum is observed close to midnight. Accordingly, the dawn-dusk asymmetry is more prominent at 150–170 km and decreases with increasing altitude. A maximum ratio of six is observed between the dusk and dawn densities at 160 km. In addition, the local time for the maximum ratio at each altitude moves toward sunlit hours with increasing altitude. The observed asymmetry is explained in terms of dynamical heating and cooling due to convergent and divergent winds at the dusk and dawn terminators, respectively. In addition, upward propagating gravity waves generated by the solar terminator wave and O/CO_2 radiative cooling are also proposed as important mechanisms contributing to the observed asymmetry.

3.1 Background

As mentioned in the introduction, recent measurements by the MAVEN spacecraft [6] provided a more detailed picture of the Martian thermosphere and revealed important temporal

and spatial variabilities [3, 205, 4]. The initial report by [4] revealed detailed altitude variations for nine atomic and molecular neutral species (CO_2, Ar, O, O_2, N_2, NO, CO, N, and He). In addition, the densities of CO_2, Ar, and He near periapsis exhibit a wavy nature, which has been attributed to gravity waves. The densities of the heavier species decrease with increasing solar zenith angle (SZA) [4]. Later, [122] demonstrated longitudinal structures in the Martian upper atmosphere that are dominated by Waves 2 and 3, accounting for 8%–16% of the change in mean density. In addition, thermospheric scale heights and temperatures have been reported to reach a maximum near perihelion and a minimum near aphelion and show a strong dependence on long-term changes in the solar flux [205]. On shorter time scales, however, local factors such as waves are found to influence the variability. Using NGIMS observations, it was shown that the temperatures and densities in the Martian upper atmosphere have a strong diurnal variation [125]. Thermospheric temperatures have been found to reach a maximum during daytime and a minimum at night. In addition, [129] reported a temperature enhancement near the dusk terminator in the equatorial and midlatitude region. This enhancement was found to be consistent with the post dusk dynamical features modelled and discussed by [130] and [5]. In this study, using the NGIMS measurements, we demonstrate a consistent asymmetry in the thermospheric densities, scale heights, and temperatures between the dawn and dusk terminators.

3.2 Data

To complement the NGIMS observations, the present study also uses the F10.7-cm solar fluxes measured at Earth and corrected for the Martian orbit and/or concurrent measurements of solar indices by the MAVEN mission.

These fluxes are shown in Figure 3.2 which indicates that the observations of the present study were acquired under a moderate-to-minimum solar activity period. The average F10.7-cm flux values corrected for the Martian orbit are 60.50 sfu (solar flux unit, 1 sfu = 10-22 $Wm^{-2}Hz^{-1}$, 38.90 sfu, and 28.68 sfu for MY 32, MY 33, and MY 34, respectively. The extreme ultraviolet (EUV) monitor experiment on MAVEN measures the soft X-ray (0.1-7 nm), EUV (17-22 nm), and Lyman$-\alpha$ (121-122 nm) fluxes in the Martian upper atmosphere. The average values of the soft X-ray fluxes are $4.02 \times 10^{-4} Wm^{-2}, 1.53 \times 10^{-4} Wm^{-2}, and 0.5 \times 10^{-4} Wm^{-2}$ for MY 32, MY 33, and MY 34, respectively. The EUV fluxes for these years are $2.98 \times 10^{-4} Wm^{-2}, 1.98 \times 10^{-4} Wm^{-2}$, and $2.27 \times 10^{-4} Wm^{-2}$, and the Lyman-$\alpha$ fluxes are $0.0028 Wm^{-2}, 0.0023 Wm^{-2}, and 0.0025 Wm^{-2}$, respectively. Combined, these solar indices consistently indicate that the observations presented in this

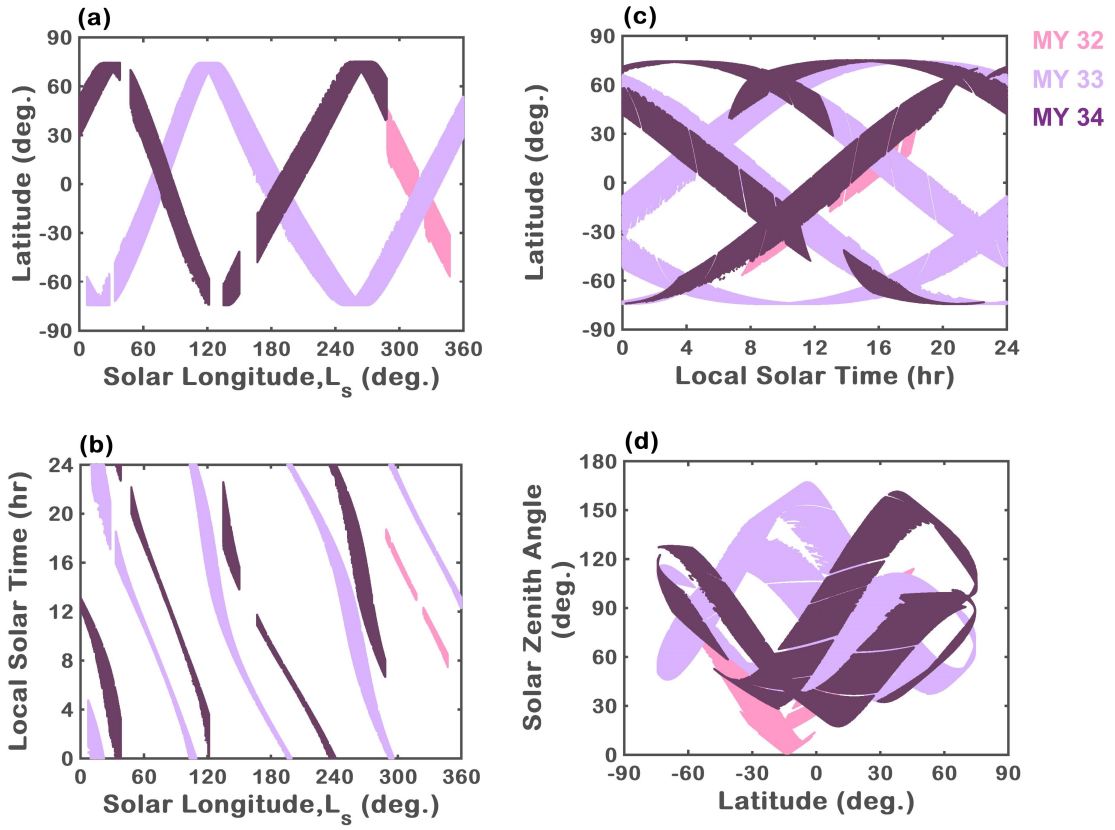

Figure 3.1: Latitude, SZA, Ls, and local time distribution of the NGIMS data coverage between periapsis and 300 km. The distributions are shown between (a) latitude and Ls, (b) local solar time and Ls, (c) latitude and local solar time, and (d) SZA and altitude. The three colors correspond to MY 32, MY 33, and MY 34.

study fall within a solar minimum period.

3.3 Results

3.3.1 Mass dependent variability

Figures 3.3a–3.3d show the SZA and altitude variation of CO_2, Ar, O, and He densities, respectively, which are averaged on a 5° × 5 km grid. The data used to construct Figure 3.3 cover all seasons, latitudes, and longitudes during MY 32–MY 34, as shown in Figure 3.1. From Figure 3.3, we can note that the densities of CO_2, Ar, and O all decrease with increasing SZA at all altitudes. The He density, however, shows a peculiar SZA variation, with enhanced values around the terminator. The SZA variability of all of these species

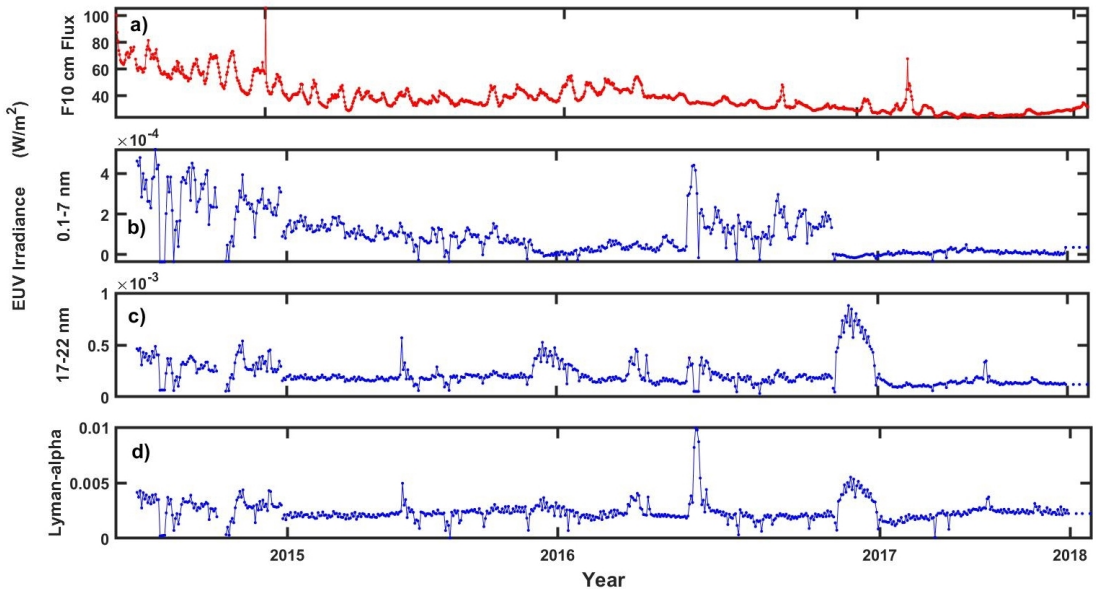

Figure 3.2: a) F10.7 solar flux output corrected for martian orbit. (bottom) solar irradiance measurements from EUVM/MAVEN for spectral band b) 0.1-7 nm c) 17-22 nm d) Lyman-α

is consistent with that shown in Figure 3.4 of [4] but extend deep into the nightside. The peculiar variability of He was previously studied by [131] and was interpreted as bulges in the polar regions. In the following, we study the local time variations of the Martian upper atmosphere using Ar densities. Most of the following results are applicable to CO_2 as well. From Figure 3.3, we can note that below 150 km, there are large gaps in the local time coverage. Hence, in the following, we restrict our analysis to altitudes above 150 km.

3.3.2 Local time Vs altitude variability

Figure 3.4 shows the altitude and local time variation of the Ar densities averaged over a 5 km $\times$ 1 hr grid using data from MY 33. From Figure 3.4, we can note that the Ar densities at all local times are higher at lower altitudes and decrease with increasing altitude. In addition, the densities are higher during daytime than nighttime. The density peak, however, is observed not at the noon but near the evening (dusk) sector. This feature can be clearly observed at all altitudes. For 150–170 km, the density peak is observed at 17–18 hr. At higher altitudes, the density peak is observed at ˜16 hr. For 150–170 km, the density minimum is observed in the morning (dawn)

sector, at 3-5 hr; however, at higher altitudes, the density minimum is observed close to midnight. A similar variability is also observed for MY 34.

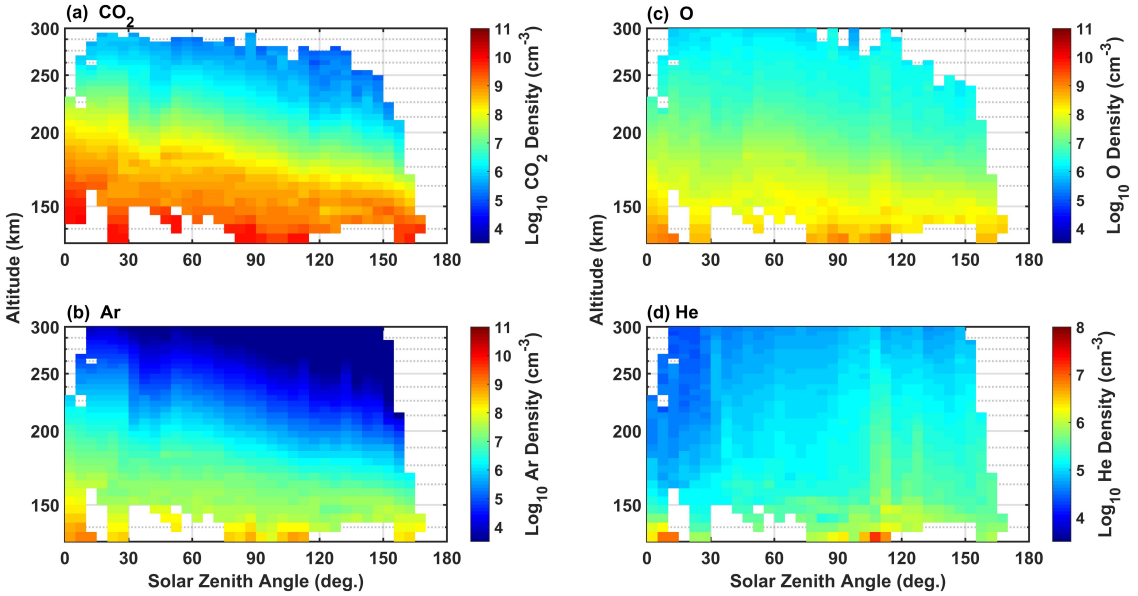

Figure 3.3: Variability of (a) CO_2, (b) Ar, (c) O, and (d) He densities as a function of SZA and altitude. These Figures were constructed using all of the data shown in Figure 3.1, which cover several latitudes, longitudes, and Ls values. The densities are averaged over a grid of 5° SZA × 5 km altitude.

3.3.3 Diurnal variation

The dawn-dusk asymmetry can be more clearly observed in Figure 3.5, where the day-to-night variation is removed. Here, we consider the hourly averaged densities at each height and remove the diurnal pattern to obtain the residual densities. We have chosen the quadratic fit to remove the smoothly varying diurnal pattern so that the dawn and dusk features are elevated. The top panels of Figures 3.5a–3.5c show the Ar densities (blue open circles connected by a thick line) for 160 km, 200 km, and 240 km, respectively. The black lines show quadratic fits to the original data. The fitted values are then subtracted from the original values to obtain residual densities, which are shown in the bottom panels of Figure 3.5. From the residual densities, we can clearly note that the densities near the dawn terminator are smaller than those at the dusk terminator at 160 km. This feature is also apparent in the original densities. At higher altitudes, the enhancement at dusk is clear in both the original and residual densities. In addition, the residual densities show a decrease at the dawn and post sunset hours, which is not apparent in the original data. This decrease is primarily due to the assumed diurnal pattern of the quadratic fit, with a peak at noon and a minimum at midnight. Having demonstrated a clear dawn-dusk asymmetry in the

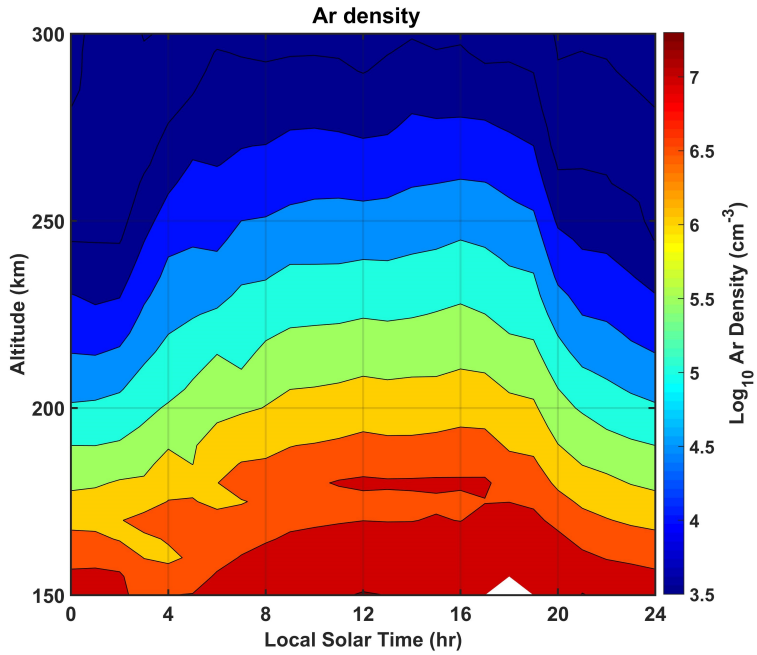

Figure 3.4: Local time and altitude variation of the mean Ar densities for MY 33. The mean densities were calculated by averaging all of the data in a 1-hr local time and 5-km altitude grid.

densities, hereafter, we deal with the original densities shown in Figure 3.4

To further clarify these local time variabilities, Figure 3.6 shows the mean (solid lines) (averaged over a grid of 1 hr in local time and 5 km in altitude) and 1σ standard deviation (shaded region) of Ar densities for the dawn (blue) and dusk (pink) sides at three altitudes (160 km, 200 km, and 240 km) for MY 33. Here, the "dusk side" is defined as local times between noon and midnight through the dusk terminator, and the "dawn side" is defined as local times between noon and midnight through the dawn terminator. Note that the bottom scale of the x-axis in Figure 3.6 displays the local times for the dawn side, whereas the top scale shows the local times for the duskside but in reverse order. This type of display is chosen to examine the asymmetry of the density variation at conjugate local times on the dawn and dusk sides. For example, 8 and 16 hr form a conjugate local time pair; similarly, 6 and 18 hr form another conjugate local time pair. From Figure 3.6, it is clear that the mean densities on the duskside are greater than those on the dawn side at most of the conjugate local times near the terminator. This trend is clearly apparent at all altitude ranges shown in Figure 3.6. At 160 km, the maximum difference is observed at 17–20 hr for the dusk terminator and 4–7 hr for the dawn terminator. At higher altitudes, the maximum difference is observed during sunlit hours. The 1σ values of the dawn side and

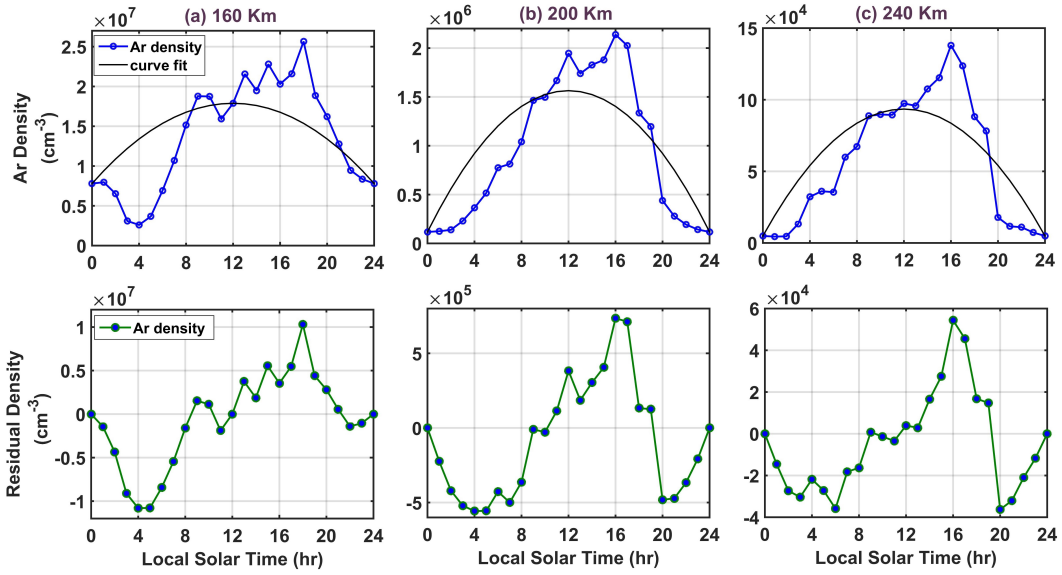

Figure 3.5: Local time variation of the Ar densities for (a) 160 km, (b) 200 km, and (c) 240 km for MY 33. The top panels display the original densities (open circles with blue lines) and a quadratic fit (black lines). The bottom panels show the residual densities obtained after the quadratic fit is removed from the original densities.

duskside, however, overlap for most of the local times and for all altitudes, except for the terminator regions at an altitude of 160 km (4–6 hr for the dawn terminator and 18–20 hr for the dusk terminator).

The dawn-dusk asymmetry is quantified in Figure 3.7, which shows the ratios of Ar densities at the conjugate local times for the dusk and dawn sides at different altitudes for MY 33. At all altitudes, the duskside densities are greater than those on the dawn side. The maximum asymmetry is observed at an altitude of 160 km, where the dusk densities at 20 hr are greater than the dawn densities at 4 hr by a factor of 6. Notably, at this height, the dusk densities are enhanced, and the dawn densities are reduced (top panel of Figure 3.5a), leading to a maximum ratio. At higher altitudes, however, the dawn-dusk asymmetry is primarily due to enhanced densities on the duskside, as the densities on the dawn side are not greatly reduced. Therefore, the ratio decreases with increasing altitude. From Figure 3.7, we can note that as the height increases, the local time of the maximum ratio shifts toward sunlit hours. For example, the maximum ratios at 180, 210, and 250 km are 3.16, 3.12, and 2.64 and are observed at dusk/dawn local times of 19/5, 17/7, and 16/8 hr, respectively. This gradual shift to sunlit hours is primarily due to the shift in the duskside density enhancements toward sunlit hours (top panels of Figures 3.5b and 3.5c).

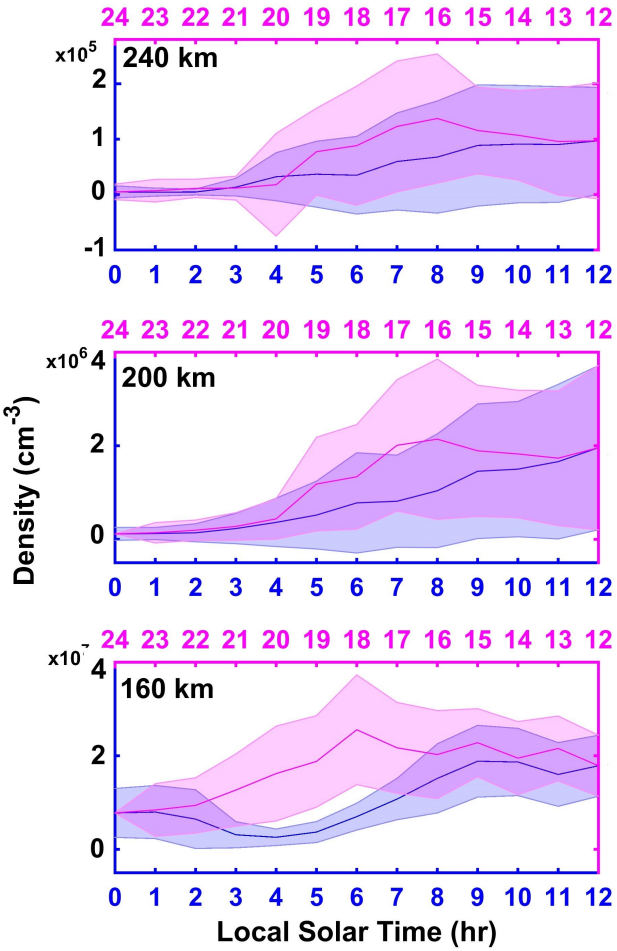

Figure 3.6: Mean and 1σ standard deviation of the Ar densities for the dawn side (midnight to noon through the morning terminator; shown for 0–12 hr on the bottom of each panel) and duskside (midnight to noon through the evening terminator; shown for 24–14 hr on the top of each panel) at three different altitudes for MY 33.

3.3.4 Seasonal and Latitudinal variability

The seasonal and latitudinal trends of the dawn-dusk asymmetry are shown in Figure 3.8, based on all of the data from MY 32-MY 34. For this purpose, we divided the observations into two latitude bands: Southern Hemisphere (SH) high latitudes (40°-90°S) and Northern Hemisphere (NH) high latitudes (40°-90°N). From Figure 3.1a, we can note that by combining the observations in MY 33 and MY 34, the NH and SH high latitudes simultaneously have full local time coverage between Ls = 90° and Ls = 160° (hereafter, near aphelion) and between Ls = 210° and Ls = 300° (hereafter, near perihelion). Accordingly, the local time and altitude variations of the Ar densities for the NH and SH high latitudes

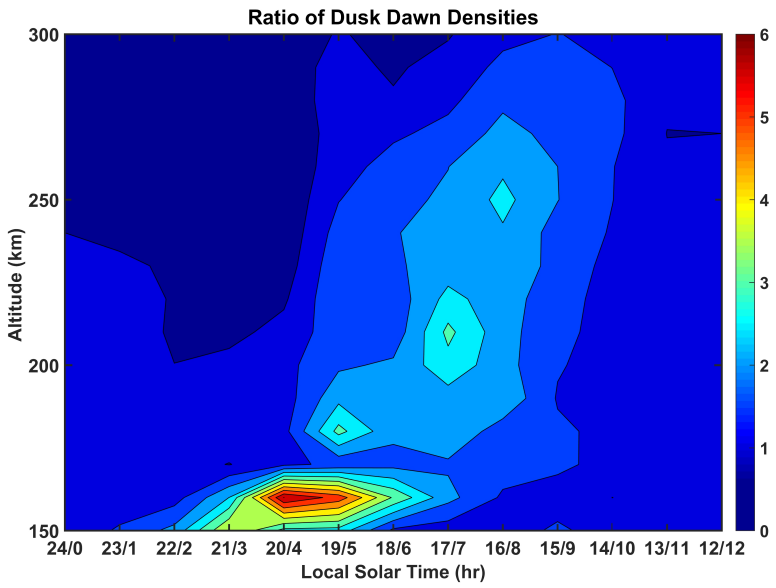

Figure 3.7: Altitude and local time variation of the ratios of the dusk to dawn densities at conjugate local times for MY 33.

are shown in Figure 3.8. In the NH high latitudes (left panels of Figure 3.8), data gaps near dawn prevent a study of the density variation and its comparison with that on the duskside. However, from the local time trend, one can clearly note that the dawn side densities are smaller than those on the duskside at any given altitude. This pattern appears to be more pronounced near aphelion. Data gaps can also be observed in the local time coverage in the SH high latitudes (right panels of Figure 3.8), but these gaps do not restrict the dawn-dusk comparison. From these panels, it is clear that the dawn-dusk asymmetry occurs in the SH as well and is thus present in both seasons. Again, the asymmetry is more pronounced near aphelion. At equatorial latitudes (40°S-40°N), the dawn-dusk asymmetry is also clear (data not shown). However, full local time coverage at equatorial latitudes is only possible when data from all seasons are combined, which may introduce some seasonal bias; hence, we do not show the variability at equatorial latitudes.

The latitude and local time variations of the Ar densities are further illustrated in Figure 3.9a, which shows the densities for an altitude of 160 km, averaged over 1 hr in local time, and 5° in latitude, based on all of the data shown in Figure 3.1. In Figure 3.9a, it is clear that the Ar densities near the dusk terminator are greater than those at the dawn terminator. This trend appears to occur for all latitudes, but further latitude-local time coverage of the observations is required to firmly establish the latitude variation of the

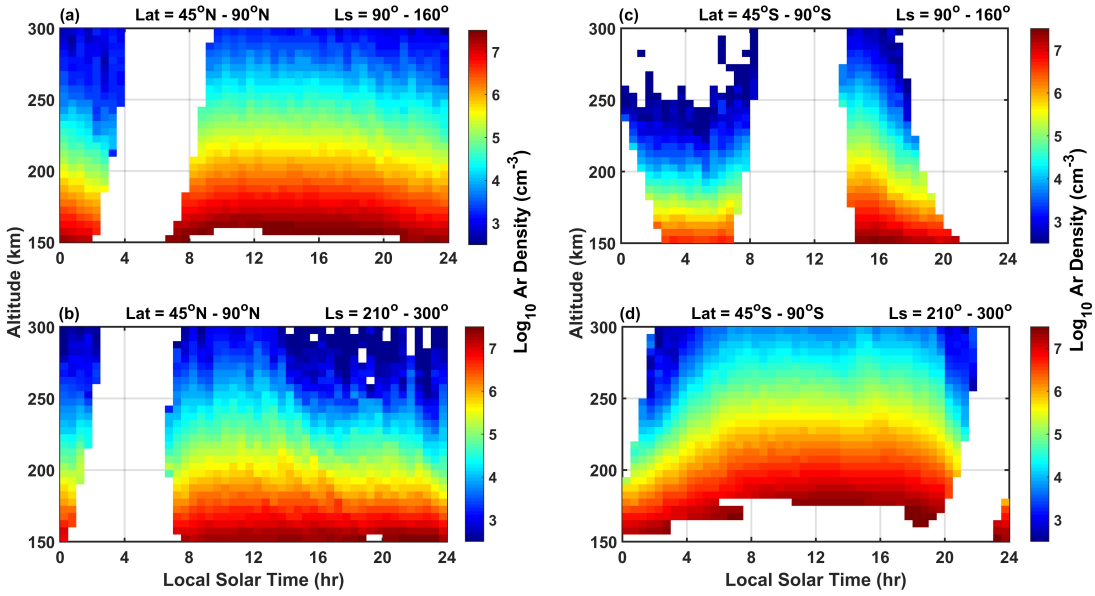

Figure 3.8: Altitude and local time variations of the Ar densities for the NH (left panels) and SH (right panels). The top panels represent the variation over an Ls range of 90°–160°, and the bottom panels represent the variations for 210°–300° Ls.

dawn-dusk asymmetry. To examine any possible seasonal bias in this Figure, we show the local time and Ls variation of the Ar density for the three Martian years in Figure 3.9b. In this Figure, it is clear that the duskside densities are greater than those at the dawn for all seasons, except between Ls = 140° and Ls = 240° in MY 34. In this case, the dawn densities are greater than those at dusk, potentially because the dawn densities occur between Ls = 185° and Ls = 225°, where a major global dust storm occurred (e.g., [208]). It is known that thermospheric densities are enhanced during lower atmospheric dust storms [89].

3.3.5 Scale Heights and Temperatures variability

The dawn-dusk asymmetry is not restricted to the Ar density. It is also observed in the CO_2 density (data not shown). Moreover, this asymmetry is also apparent in the Ar scale heights and temperatures. Figure 3.10 shows the scale heights (top panels) and temperatures (bottom panels) of Ar as a function of periapsis SZA. This Figure shows that the scale heights and temperatures are larger at low SZAs and decrease gradually with increasing SZA; however, the spread of scale heights and temperatures is enhanced near the terminator.

The local time and seasonal variation of the Ar scale heights and temperatures are shown in Figures 3.11a and 3.11b, respectively, for MY 32 (left panels), MY 33 (middle

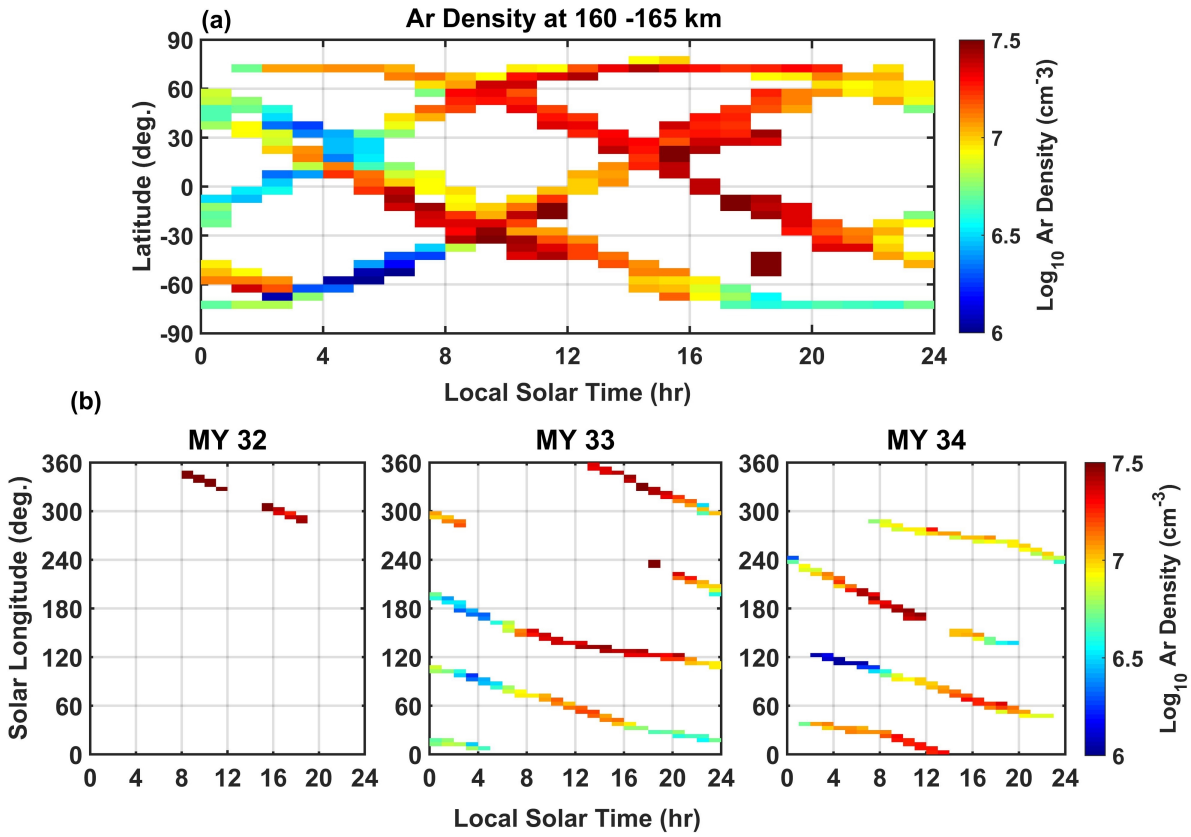

Figure 3.9: (a) Latitude and local time variations of the Ar densities for 160 km. All of the data shown in Figure 3.1 were used to construct this Figure. (b) Ls and local time variation of the Ar densities at 160 km for (left to right) MY32, MY33, and MY34.

panels), and MY 34 (right panels). In this Figure, it is clear that the scale heights and temperatures are greater for the duskside than for the dawn side. This asymmetry is apparent for all seasons in both MY 33 and MY 34, where data are available for both terminators. At the dusk terminator, the average scale heights (temperatures) for MY 32, MY 33, and MY 34 are 15.8 (254), 13.13 (210), and 11.9 km (190.5 K), respectively. At the dawn terminator, these values are 10.8 (174) and 9 km (144 K) for MY 33 and MY 34, respectively. For MY 32, data are not available for the dawn terminator. The decrease in scale height from MY 32 to MY 34 is in accordance with the variation in the F10.7-cm flux, which decreases from 60.5 sfu to 38.9 sfu and then to 28.68 sfu from MY32 to MY 34. The scale heights reach a maximum of 23 km on the duskside and a minimum of 4.7 km on the dawn side.

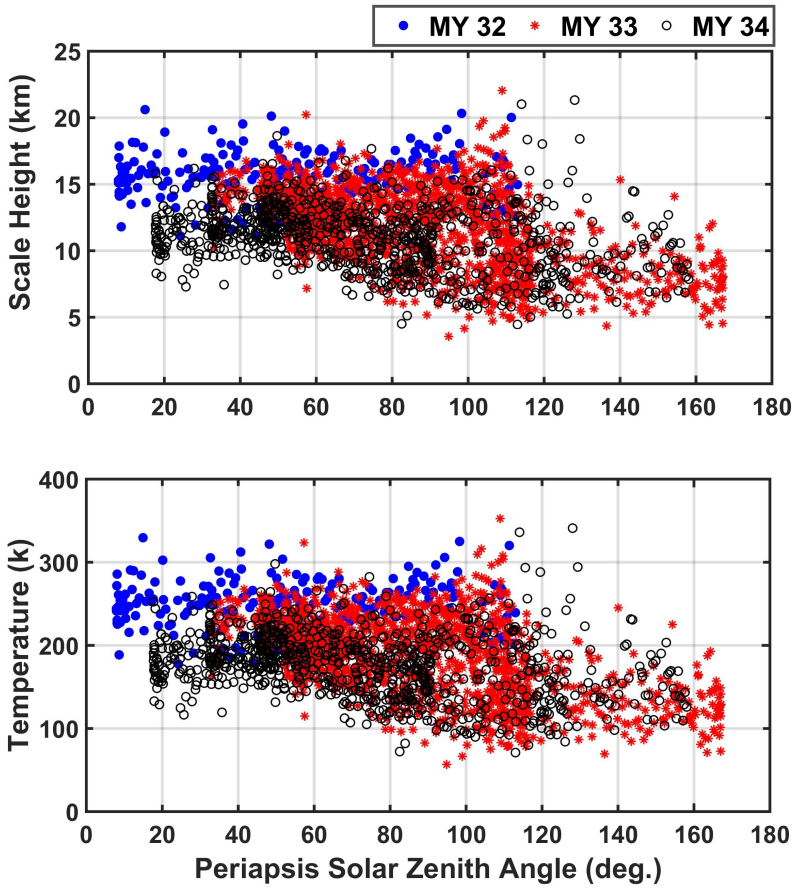

Figure 3.10: SZA variation of the Ar (top panel) scale heights and (bottom panel) temperatures for (blue closed circles) MY 32, (red stars) MY 33, and (black open circles) MY 34.

3.4 Discussion

In this study, we investigated the local time variabilities in the Martian upper atmosphere (between 150 and 300 km) using Ar densities measured by the MAVEN NGIMS for MY 32, MY 33, and MY 34. The daytime densities were found to be higher than the nighttime values; however, the peak density is observed close to the dusk terminator. This dusk enhancement is consistently observed at all altitudes, but with increasing altitude, the enhancement moves toward sunlit hours. For 150–170 km, the density minimum is observed at the dawn terminator. At higher altitudes, the density minimum is close to midnight. Thus, there is a clear asymmetry in the densities between the dusk and dawn terminators. At an altitude of 160 km, the densities at the dusk terminator are sixfold greater than those

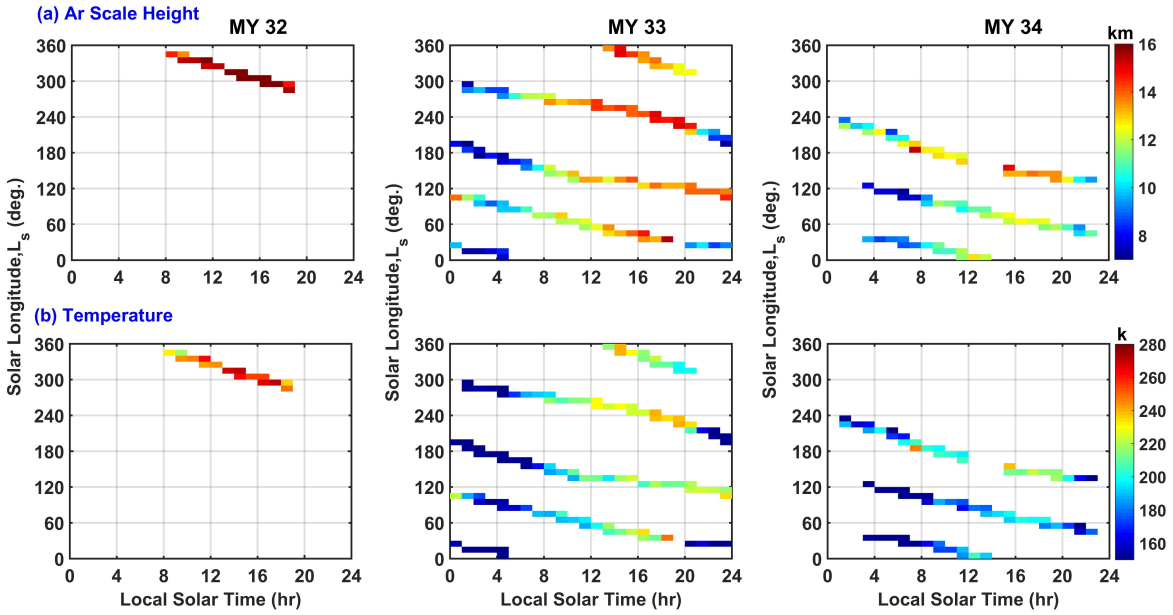

Figure 3.11: Local time and Ls variation in Ar (a) scale heights and (b) temperatures for (left to right) MY 32, MY 33, and MY 34.

at dawn. The conjugate local times (with respect to noon) at which this asymmetry is observed are ˜18–20 hr on the duskside and 4–6 hr on the dawn side; however, this dawn-dusk asymmetry decreases with increasing altitude. Moreover, the conjugate local times showing asymmetry shift toward sunlit hours with increasing altitude, primarily due to the shift in the dusk enhancement. This dawn-dusk asymmetry in the upper atmospheric densities is observed in both aphelion and perihelion seasons but is more pronounced near aphelion. Moreover, the asymmetry appears to be present at all latitudes. In addition to the densities, the scale heights and derived temperatures also show a similar asymmetry. Such an asymmetry is observed in the CO_2 density as well.

The diurnal variation of the Martian upper atmospheric densities and temperatures, with larger values during daytime and smaller values during nighttime, is consistent with the previous NGIMS observations [125] and Mars Global Ionosphere-Thermosphere Model (M-GITM) simulations [5]. In addition, the present study also shows that the densities, temperatures, and scale heights at the dusk terminator are greater than those at the dawn terminator. Previously, [206] studied the variability of the Martian thermospheric densities measured by the MAVEN accelerometer. Using data from the MAVEN deep-dip (DD) campaigns, they reported that the thermospheric densities on the duskside (DD1 campaign) are greater than those on the dawn side (DD5 campaign). However, this trend could not be firmly established, as there was a change in season between the two measurements

(DD1 occurred near perihelion, whereas DD5 occurred near autumnal equinox). Using NGIMS observations, [129] reported two local maxima and one minimum in thermospheric temperatures at the dusk terminator. The enhancement at dusk is consistent with simulation results obtained for general circulation models [5, 209]. Our study shows a reduction in temperatures and densities at the dawn terminator, while [129] showed an enhancement. The results of the present study are also consistent with the results of global circulation modeling [5, 209]. In global circulation models, the asymmetry is primarily confined to the equatorial and midlatitudes, while the present study shows an asymmetry at all latitudes.

A dawn-dusk asymmetry was previously studied in the Venusian thermosphere using Pioneer Venus Orbiter observations (including the orbiter ultraviolet spectrometer) and numerical simulations [210, 30, 211, 212, 213]. These observations showed dusk terminator O mixing ratios up to 2.5-fold larger than those at the dawn terminator. The dawn-dusk asymmetry of Ar densities in the Martian upper atmosphere (present study) is qualitatively consistent with that of O mixing ratios in the Venusian thermosphere, although the variations in Ar cannot be directly compared with those of O. Super rotation of the thermosphere and an asymmetrical turbulence pattern due to upward propagating gravity waves have been proposed as plausible sources of the asymmetry in the Venusian thermosphere. The asymmetry on Venus was observed only at latitudes poleward of 30° in both the Northern and Southern Hemispheres, while such a pattern was not apparent in the equatorial latitudes.

In the Martian thermosphere (the present study), however, the dawn-dusk asymmetry is observed at all latitudes; thus, there are some differences in the dawn-dusk asymmetries observed in the Martian and Venusian upper atmospheres. To understand the observed dawn-dusk asymmetry in the densities, scale heights, and temperatures, it is important to examine the possible mechanisms that lead to cooling at the dawn terminator and heating at the dusk terminator. The densities and scale heights follow the heating and cooling trends. The Martian thermosphere is primarily heated by EUV radiation, which reaches a maximum at local noon and decreases gradually toward the terminator. As there are no sharp variations in flux at the terminator, the EUV radiation cannot be the source of the observed asymmetry. Previous modeling studies have shown that adiabatic heating produced by the convergence of large-scale winds at the dusk terminator and cooling due to divergence of winds at the dawn terminator can explain the observed asymmetries [5, 209, 129]. While this basic mechanism can explain the observed asymmetries, in the following, we discuss other possible mechanisms.

CO_2 radiative emission at 15 μm is an important cooling mechanism in the Martian thermosphere. The O/CO_2 mixing ratio is generally used as an indicator for this cooling,

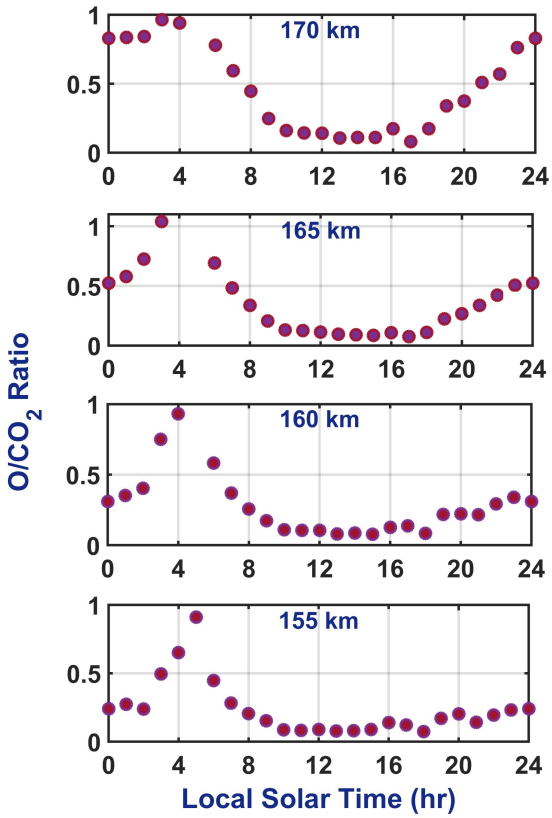

Figure 3.12: Local time variation of the O/CO_2 ratio for (top to bottom) 170, 165, 160, and 155 km, based on observations for MY 33.

as collisions between O and CO_2 lead to the excitation of CO_2 molecules, which ultimately radiate at 15 μm (e.g., [214]). This mechanism is examined in the present study using the NGIMS measurements. Figure 3.12 shows the O/CO_2 ratios for 155, 160, 165, and 170 km for MY 33, where the observed asymmetry reaches a maximum (Figures 3.3 and 3.4a). From Figure 3.12, we can note that the O/CO_2 ratio is close to unity near the dawn terminator, indicating that the observed reduction in temperatures, scale heights, and densities at dawn can be partially attributed to O/CO_2 radiative cooling.

Dynamical heating of the thermosphere by upward propagating gravity waves is another possible mechanism. In particular, gravity waves with high-phase speeds can reach the middle and upper thermosphere and contribute to the divergence of the viscous heat flux that tends to heat in the middle and upper thermosphere of Mars [215, 216]. The key aspect to the practicality of this mechanism is finding a source that continuously supplies gravity waves at the terminator. The solar terminator wave [52, 51, 217] is one such constant source of gravity waves. Modeling simulations for Mars have shown that the dusk terminator

produces strong gravity waves [51] that propagate upward and heat the middle and upper thermosphere of Mars through divergence of the viscous heat flux. This behavior leads to strong heating of the middle and upper thermosphere at the dusk terminator, resulting in an increase in temperatures, densities, and scale heights. At the dawn terminator, however, the amplitudes of these gravity waves are lower [51]. Assuming that the corresponding phase speeds are smaller, these waves can lead to heating of the lower thermosphere and cooling of the middle and upper thermosphere through convergence of the sensible heat flux [215, 216]. However, the cooling of the middle and upper atmosphere at the dawn terminator is expected to be weaker due to the smaller amplitudes of the gravity waves. Thus, cooling and heating by gravity waves generated by the solar terminator wave are another possible mechanism that may contribute to the observed dawn-dusk asymmetry. We propose that a combination of these three mechanisms is responsible for the altitudinal and seasonal variation of the dawn-dusk asymmetry, which requires further investigation in the future based on general circulation models. Finally, the consistent enhancement in densities and temperatures at the dusk terminator may have significant implications on the gaseous escape, as the enhancement can effectively lift gases to altitudes above the exobase, where they can be easily lost to space.

Chapter 4

Enhanced densities in the Martian thermosphere associated with the 2018 planet encircling dust event: Results from MENCA/ MOM and NGIMS/ MAVEN

In the previous study we investigated the local time variability of Ar and CO_2 densities and scale heights. The results of the previous study showed a consistent temporal asymmetry in the Ar densities and scale heights at most of the latitudes. In this study, we further investigate the variability of Ar density to bring out a seasonally consistent and global picture of the thermosphere of Mars. We present and analyse the unique observations of the Martian thermosphere made together by the Mars Orbiter Mission (MOM) and the Mars Atmosphere and Volatile Evolution (MAVEN) spacecraft. The Mars Exospheric Neutral Composition Analyzer (MENCA)/MOM and the Neutral Gas and Ion Mass Spectrometer (NGIMS)/MAVEN have simultaneously (on the same day) measured the neutral densities in the Martian thermosphere. These measurements were made on 5, 8, 10, 13, 16, and 29 June, 2018 when the periapsis altitude of MOM occurred in the mid-thermosphere. This period falls in the onset and progression time of the planet encircling dust event (PEDE) in the Mars lower atmosphere. During this time, the inbound trajectories of MAVEN and MOM spacecraft occurred on the dawn and dusk sides, respectively. Using these observations, we found that thermospheric densities both on the dawn and dusk sides are enhanced associated with the onset and growth of PEDE-2018. The enhancement, however, is more on the dusk side than on the dawn showing the dawn-dusk asymmetry. The densities on the dusk side reach their maximum on 29 June, 2018 close to the time of peak dust activity. These results are explained by considering the local time asymmetries in the radiative

heating of the lower atmosphere and subsequent expansion of the thermosphere due to PEDE-2018. Furthermore, O/CO_2 ratios below 220 km altitude become one on the dawn side whereas they are always <0.2 at the dusk. This indicates that the radiative cooling is more efficient on the dawn side than the dusk side.

4.1 Background

Previous studies have shown that increase in dust activity in the Mars lower atmosphere significantly affects the densities and temperatures of its upper atmosphere [126, 30, 31, 32, 49, 89, 127, 128]. The coupling between the two regions takes place primarily through the radiative heating of the dust aerosols. The resulting heating and expansion of the Mars atmosphere and subsequent modifications to atmospheric circulation drive the changes in the upper atmosphere [126, 30, 28, 31, 32]. Although the upper atmospheric changes are observed during all dust storms, they are prominent during the planet-encircling dust events (PEDEs), such as the one occurred in 2018 (PEDE-2018, [31, 32]).

Among the Martian upper atmospheric variabilities, variations near the terminator are of particular interest. The MAVEN spacecraft, however, covers only one terminator at any given time due to its slow precession in local time. As a result, measurements from other terminator are available only after several months and in a different season. It is, therefore, important to probe the two terminators simultaneously (i.e., on the same day) in order to have better understanding on their variability. Fortuitously, such measurements were made in June 2018 when the MAVEN and MOM spacecraft observed the dawnside and duskside, respectively during the onset and growth phase of PEDE-2018 [218, 219, 220]. During this time, the periapses of both the spacecraft occurred in the mid-thermosphere and in low-latitude regions. Both the spacecraft have mass spectrometers that measured important neutral species of the Martian upper atmosphere. In the present study, we use these near simultaneous observations to get further insight into the Martian thermosphere at terminators and to study its response to PEDE-2018.

4.2 MENCA and NGIMS measurements

The spatial and temporal coverage of MENCA and NGIMS during the six days are shown in Figure 4.1. From Figure 4.1, it can be noted that the observations of the present study are confined to low-latitudes and fall in different longitude sectors. The inbound trajectories shown in Figure 4.1 start at an altitude of 220 km at the north-of/near the equator and their

periapses end at the south of the equator. In addition, MOM observations fall on the dusk side (local times between 17.51 hr and 18.47 hr) whereas those of MAVEN are on the dawn side (local times between 07.10 hr and 08.20 hr). From tables 4.1 and 4.2, we can note that the NGIMS and MENCA observations are not exactly simultaneous. Hence, in the text we often use 'near simultaneous' to refer to the observations made on the same day. In addition to the six days of observations, we also use NGIMS observations from Martian Years (MYs) 33 and 34 for a statistical analysis

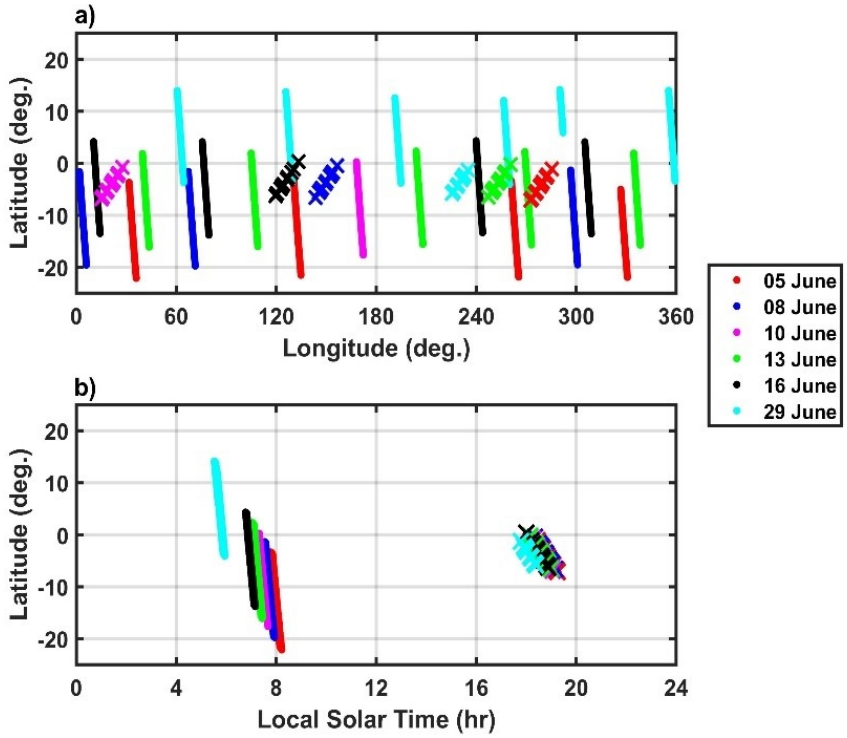

Figure 4.1: MAVEN (closed circles) and MOM (crosses) "along-track" (a) latitude versus longitude and (b) latitude versus local solar time coverage of the inbound trajectories. The inbound trajectories start at an altitude of 220 km at north-of/near the equator and their periapses end at south of the equator.

4.3 Results

4.3.1 Altitude variation of Ar densities

Figure 4.2 shows the altitude profiles of Ar densities measured by NGIMS and MENCA in the inbound segments of MAVEN and MOM spacecraft, respectively on 5, 8, 10, 13,

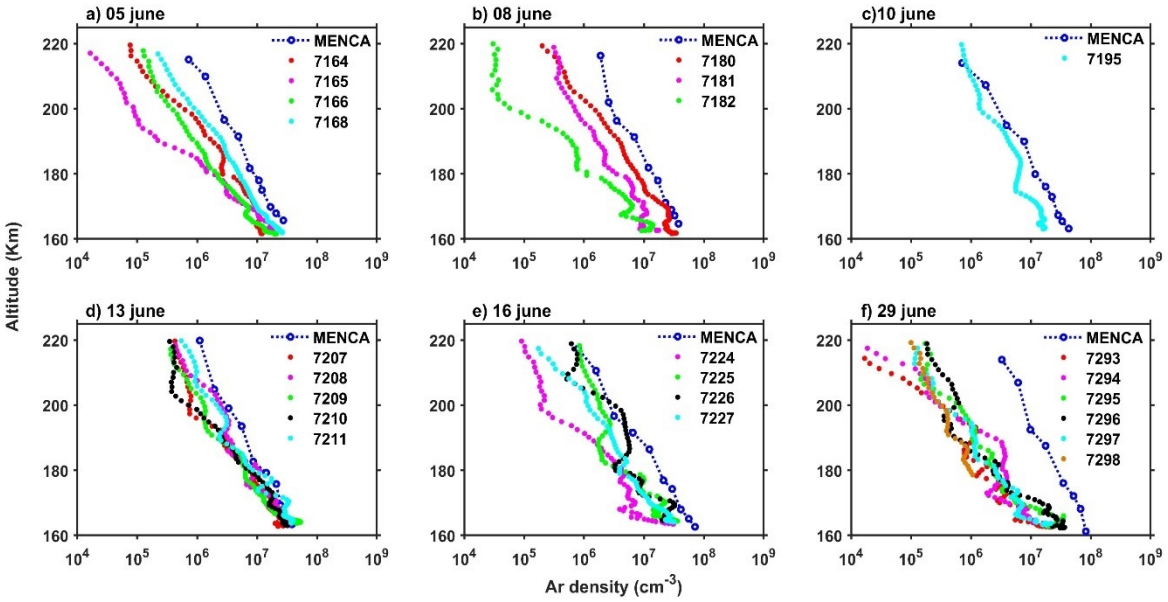

Figure 4.2: Altitude profiles of Ar densities measured by (open circles) MENCA/MOM and (closed circles) NGIMS/MAVEN on (a-f) 05, 08, 10, 13, 16 and 29 June, 2018. The NGIMS observations for each day are color coded. Note that on each day MOM has only one inbound segment and hence the orbit numbers are not provided.

16, and 29 June, 2018. Note that on each day, MENCA has only one profile whereas NGIMS has more than one due to the less orbital period of MAVEN (˜4.5 hr versus ˜65 hr for MOM). Here, we use Ar densities for studying the Martian thermosphere. The results of the study, however, are equally applicable to CO_2 densities. In general, densities measured by both NGIMS and MENCA decrease with an increase in altitude. Furthermore, densities measured by NGIMS in different orbits on a given day show large variability, as high as an order of magnitude. From Figure 4.1 we can note that the MAVEN orbits on a given day cover different longitude sectors. Therefore, the observed variability in NGIMS measurements on a given day is most likely due to longitudinal variations caused by tides and planetary waves (e.g., [221, 122]). More importantly, densities measured by MENCA on the dusk side are greater than those measured by NGIMS on the dawn side. This is particularly evident on 05, 08, 10, and 29 June. The differences are largest on 29 June.

From Figure 4.2, it can be noted that the altitude resolutions of MENCA and NGIMS measurements are different. The resolution of NGIMS measurements ranges from 0.06 km to 2.51 km whereas those of MENCA lie between 1.81 km and 15.02 km. In order to compare their densities, it is important to bring these measurements to the same altitude resolution. For this purpose, the MENCA densities in each profile are interpolated between

165 km and 220 km with 5 km resolution. Considering the high resolution of NGIMS measurements, their densities are averaged over 5 km grid. For example, the densities at 170 km are obtained by averaging the densities between 167.5 km and 172.5 km. The interpolation and averaging procedures are illustrated in Figure 4.3.

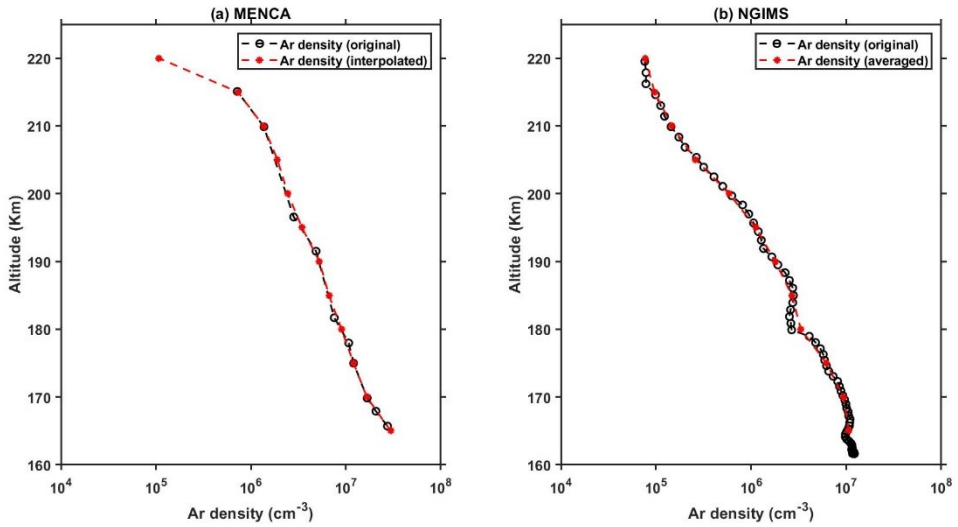

Figure 4.3: Altitude profiles of Ar densities observed in the inbound segments on 05 June 2018 by (a) MENCA and (b) NGIMS. The open black circles represent the original data points and the red closed circles represent the points with 5 km resolution. The 5 km resolution points for MENCA observations are obtained by linear interpolation and for NGIMS by averaging within 5 km altitude range.

With the above procedure, we obtained the NGIMS and MENCA density profiles with 5 km altitude resolution. In the following we use these densities to compare the changes on the dawn and dusk sides.

Figure 4.4 shows mean and standard deviations of Ar densities computed using all the profiles observed on the six days. These computations were separately carried out for NGIMS and MENCA observations. From Figure 4.4, it can be noted that the densities on both terminator sides show large variability within a few days. Despite this, MENCA densities on the dusk side are, on average, 3.5 times larger than those of NGIMS on the dawn side. On 29 June, when the dawn side observations are measured at the terminator (Table 4.2), the densities at dusk terminator exceed those at the dawn by an order of magnitude (Figure 4.2f). Furthermore, from Tables 4.1 and 4.2 it can be noted that the average scale heights and scale height derived temperatures, respectively are 12.24 km and 195.78 K on the dawn side and 14.17 km and 242.67 K on the dusk side. Thus, the Ar scale heights and scale height temperatures on the dusk side are, on average, 1.93 km and 46.89 K greater

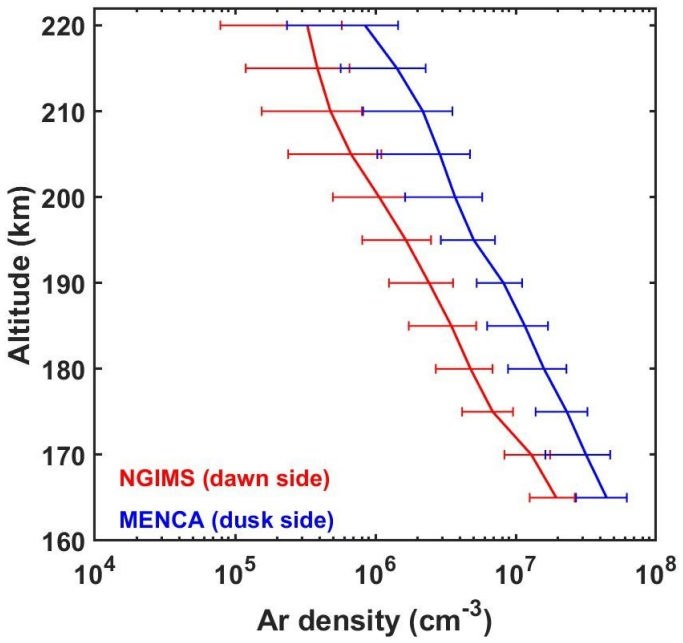

Figure 4.4: Mean and standard deviation of Ar density profiles measured by (red) NGIMS/MAVEN and (blue) MENCA/MOM.

than those on the dawn side. However, these differences become insignificant when the errors in the scale heights (a few km) and scale height temperatures (a few tens of K) are considered (Tables 4.1 and 4.2).

4.3.2 Seasonal and Local time variability

Figure 4.5 shows the solar longitude (Ls) versus local time variability of the Ar densities, scale heights and temperatures by including all the NGIMS observations in MY 34. These measurements are averaged 1 hr in local time and 5° in Ls. The densities shown in Figure 4.5a correspond to an altitude of 170 km. For comparison, the six days of MENCA observations from the dusk side are also included (the dotted horizontal arrows in Figure 4.5 point to the MENCA observations). By looking at the NGIMS observations alone, we can note that the densities on the dusk side are greater than those on the dawn side. This result is consistent with the dawn-dusk asymmetry presented in Chapter-3.

Table 4.1: Summary of MOM orbital parameters at the periapsis and scale heights and derived temperatures for Ar (with 1σ error) measured by MENCA on six days in June 2018

Date	UTC (hr)	LST hr)	Lat. (deg.)	Lon. (deg.)	SZA (deg.)	Ls (deg.)	Alt. (km)	Ar SH (error) (km)	Temp. (error) (K)
05 June 2018	11.48	18.45	-1.07	285.20	96.76	187.8	165.70	14.70 (1.65)	251.59 (28.25)
08 June 2018	4.54	18.35	-0.47	156.46	95.21	189.4	164.67	14.43 (1.29)	247.05 (22.17)
10 June 2018	21.61	18.40	-1.93	25.41	93.93	190.9	162.94	14.01 (1.43)	239.83 (24.61)
13 June 2018	14.78	18.16	-0.24	260.51	92.39	192.5	163.38	14.38 (2.02)	246.17 (34.66)
16 June 2018	7.90	18.00	0.30	133.33	90.17	194.1	162.62	11.66 (0.56)	199.59 (9.63)
29 June 2018	23.24	17.79	-1.29	234.97	82.70	202.2	154.30	15.88 (6.78)	271.84 (116.09)

Notes. Columns 2-8 list the Universal Time (UTC, hours), Local Solar Time (LST, hours), Latitude (Lat., degrees), Longitude (Long., degrees), Solar Zenith Angle (SZA, degrees), Solar Longitude (Ls, degrees), Altitude (Alt, km). Columns 8 and 9 summarize the scale heights and scale height temperatures, respectively along with their 1σ errors shown in the brackets.

4.3.3 Role of Global Dust Storm (PEDE-2018)

The densities and scale heights between Ls = 185° and Ls = 220° on the dawn side are relatively larger compared to those in other seasons observed at the same local time. It is important to note that the PEDE-2018 had its onset around 1 June 2018 (Ls˜=185°) and peaked during 7-10 July (Ls˜205°), 2018 [218, 220]. Considering the NGIMS densities alone, it is not clear whether the dawn-dusk asymmetry is retained during PEDE-2018 or not. This is mainly due to the lack of observations from the dusk side. The MENCA observations in the present study fill this gap. By comparing the MENCA and NGIMS observations (Figure 4.4), it is clear that during PEDE-2018 also the densities on the dusk side are greater than those on the dawn side. This is also apparent in Ar scale heights and temperatures. Thus, during the PEDE-2018 period the densities are enhanced both on the dusk and dawn sides so that the dawn-dusk asymmetry is intact.

[31] have studied changes in the upper atmospheric densities during the PEDE-2018 using NGIMS measurements. A similar analysis is carried out here by including the MENCA observations and the results are shown in Figure 4.6. The NGIMS and MENCA measured densities at an altitude of 170 km are shown in Figures 4.6a and 4.6b, respectively. Figure 4.6c shows the 9.3 μm IR absorption column dust optical depth (CDOD) corresponding to 610 Pa [100, 222] averaged between ± 25° latitudes and all longitudes. Figure 4.6a is similar to that reported by [31] where they have reported an increase in Ar and CO_2 densities

Table 4.2: Summary of MAVEN orbital parameters at the periapsis and scale heights and derived temperatures of Ar measured by NGIMS for selected days in June 2018

Date	Orbit	UTC (hr: mm)	LST (hr)	Lat. (deg.)	Lon. (deg.)	SZA (deg.)	L_S (deg.)	Alt. (km)	Ar SH error (km)	Temp. (error) (K)
05 June 2018	7164	03:37	8.20	-21.31	35.79	58.15	188.34	161.62	13.81(7.29)	220.93(116.57)
	7165	08:04	8.18	-21.12	330.48	58.37	188.46	162.27	8.30 (3.53)	132.71 (54.99)
	7166	12:32	8.16	-21.06	265.20	58.57	188.57	161.48	15.27 (3.37)	244.25 (53.98)
	7168	09:26	8.13	-20.71	134.61	58.99	188.81	161.87	11.23(2.67)	179.00 (42.82)
08 June 2018	7180	02:53	7.92	-19.20	71.24	61.52	190.23	161.62	10.89 (2.11)	174.14 (33.76)
	7181	07:20	7.90	-19.02	5.96	61.74	190.34	162.61	12.66 (5.00)	202.50 (80.10)
	7182	11:47	7.88	-18.97	300.68	61.96	190.46	162.51	11.88 (8.04)	190.10 (128.70)
10 June 2018	7195	09:41	7.66	-17.36	172.13	64.85	192.00	163.07	12.93 (5.37)	206.85 (85.88)
13 June 2018	7207	03:07	7.44	-15.45	108.82	67.76	193.43	162.78	11.16 (3.96)	178.96 (63.40)
	7208	07:34	7.43	-15.54	43.62	67.92	193.55	162.95	15.70 (4.11)	251.04 (65.86)
	7209	12:02	7.41	-15.45	338.36	68.15	193.67	163.76	16.77 (4.68)	268.23 (74.94)
	7210	04:29	7.39	-15.14	273.04	68.46	193.79	163.16	9.89 (4.49)	158.15 (71.87)
	7211	08:56	7.38	-15.04	207.80	68.68	193.91	163.78	12.65 (7.76)	202.30 (124.12)
16 June 2018	7224	06:49	7.15	-13.25	79.44	71.90	195.46	163.44	11.41 (5.79)	182.55 (92.64)
	7225	11:16	7.13	-13.22	14.22	72.11	195.58	164.35	14.43 (6.68)	230.77 (106.83)
	7226	03:43	7.11	-13.01	308.92	72.40	195.69	164.53	13.53 (3.88)	216.34 (62.10)
	7227	08:10	7.10	-12.81	243.67	72.67	195.81	164.13	12.76 (4.81)	204.14 (76.99)
29 June 2018	7293	01:48	5.94	-4.08	260.02	90.20	203.73	162.53	9.77 (9.31)	156.33 (148.90)
	7294	06:15	5.94	-3.82	259.96	90.31	203.73	162.53	8.21 (7.56)	131.33 (120.95)
	7295	10:42	5.92	-3.80	194.80	90.54	203.86	163.18	10.71 (6.24)	171.34 (99.82)
	7296	03:08	5.90	-3.63	129.60	90.84	203.98	162.77	13.37 (7.11)	213.81 (113.73)
	7297	07:35	5.89	-3.43	64.41	91.14	204.10	162.24	12.47 (4.51)	199.38 (72.11)
	7298	23:54	5.87	-3.40	359.26	91.37	204.22	163.25	11.74 (2.62)	187.86(41.95)

Notes: Columns 3-11 are similar to columns 2-10 in table 4.1, except that UTC in column 3 is shown in hour: minute (hr: mm) format.

associated with PEDE-2018 on the dawn side. Comparing, Figures 4.6b and 4.6c, we can note that MENCA observations on the dusk side start and end during the growing phase of PEDE-2018. During this period, the SZA at 170 km changes only by ˜ 13° whereas the densities show three-fold increase. The enhancement is particularly strong between 13 June and 29 June. Note that 29 June falls close to the peak of the PEDE-2108. Therefore, it is possible that at least a part of the density variation observed by MENCA is driven by PEDE-2018. However, since the SZA on both dawn and dusk sides varies throughout the observation period and the neutral densities decrease with an increase in SZA [4, 223], it is difficult to firmly attribute the observed variabilities to the dust activity. Particularly on the dawn side (Figure 4.6a), the dust related enhancement is not readily apparent as there

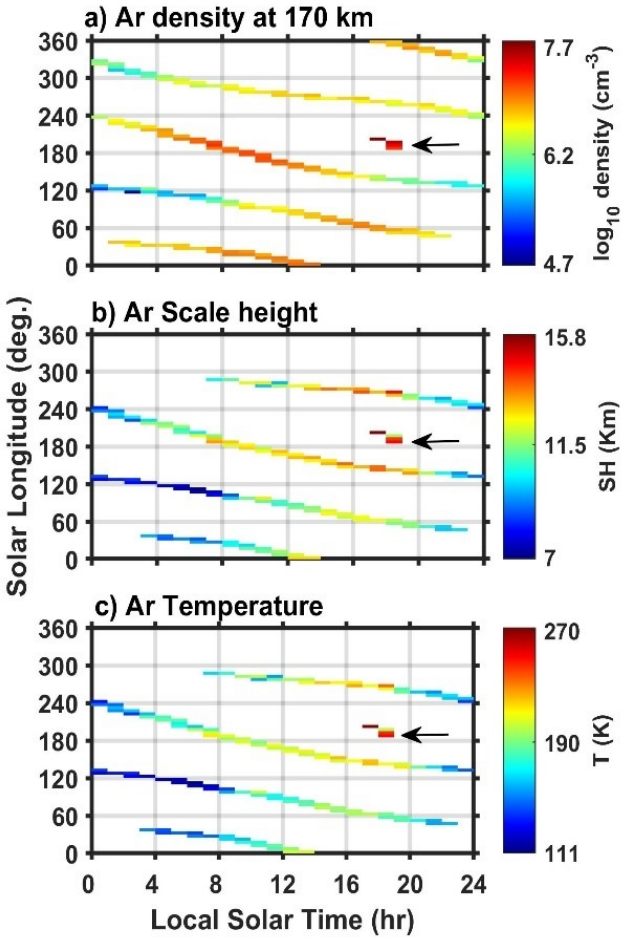

Figure 4.5: Solar longitude versus local solar time variations of Ar (a) densities at 170 km, (b) scale heights below the exobase, and (c) scale height temperatures measured by NGIMS and MENCA in MY34. Horizontal arrows in all panels point to the MENCA observations.

is ˜50° change in SZA during the course of the observation.

To clearly bring out the changes in thermospheric densities due to lower atmospheric dust activity, the densities at 170 km (shown in Figures 4.6a and 4.6b) are plotted as a function of SZA in Figure 4.7. For comparison, the densities measured by NGIMS at 170 km in MY 33 and those between Ls=0° and Ls=120° in MY 34 are averaged and shown in Figures 4.7a and 4.7b as 'seasonal mean'. These values are considered to represent the SZA variation of Ar densities in general. All the NGIMS densities shown in Figure 4.7 are averaged over 1° SZA and the SZA variation on the dawn and dusk sides are computed separately. From Figure 4.7a, we can note that the densities during PEDE-2018 and those of the seasonal mean, both vary with SZA. However, the densities during PEDE-2018 show

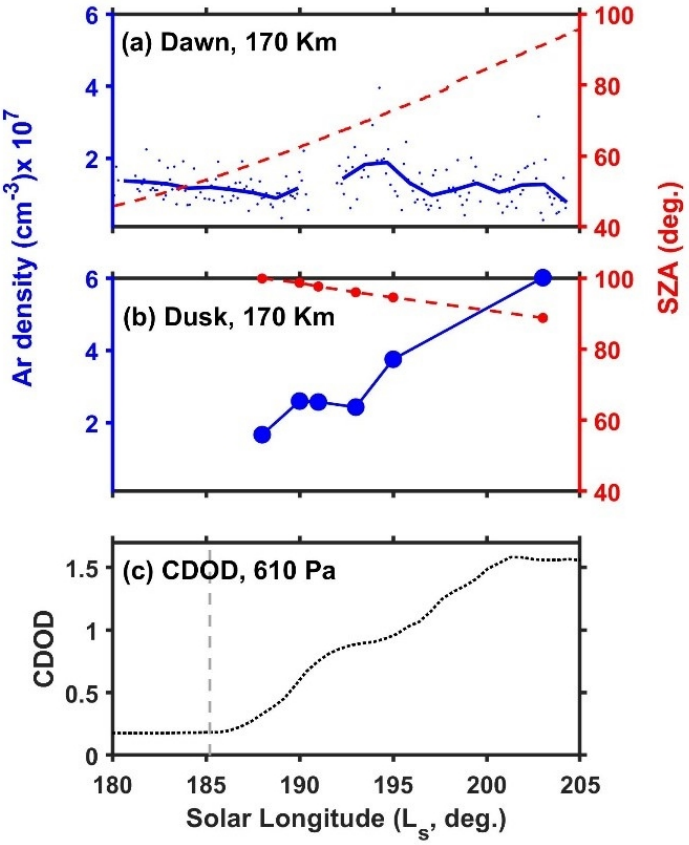

Figure 4.6: Solar longitude (Ls) variation of Ar densities at 170 km measured by (a) NGIMS/MAVEN and (b) MENCA/MOM spacecraft. In panel 'a', the dots represent the individual measurements and the solid line represents the ten-orbit smoothing average. Dashed red line in panels 'a' and 'b' represent the SZA (mentioned on the right ordinate). (c) Ls variation of CDOD at 610 Pa. Vertical line at the bottom panel indicates the time of onset of the PEDE-2018.

a sudden enhancement after SZA=65° and continue to be higher than the mean values. Comparing Figures 4.7a, 4.6a, and 4.6c, we can note these sudden enhancements occurred in the growth phase PEDE-2018. Between SZA of 66° and 94°, the average value of the 'seasonal mean' densities is 5.05× 106 cm-3 and during PEDE-2018 the value is 13.5 × 106 cm-3. Thus, the densities during the PEDE-2018 are ˜ 2 times those of the seasonal mean values. In addition, there are sporadic enhancements in densities at SZAs of 70°-71° (Ls=˜194°) and 89°-90° (Ls=˜202°). At these SZAs, the PEDE-2018 densities are 3.4 and 4.5 times, respectively of the seasonal mean values. This clearly shows that the enhancement in densities associated with PEDE-2018 is apparent when the densities are plotted as a function of SZA

On the dusk side (Figure 4.7b), the densities during PEDE-2018 drastically depart from

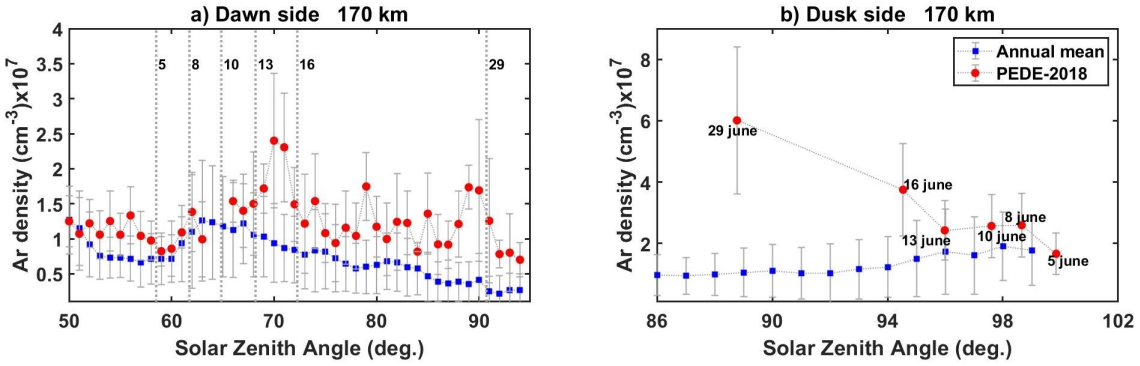

Figure 4.7: SZA variation of the (blue squares) seasonal mean and (closed red circles) PEDE-2018 Ar densities for 170 km observed (a) on the dawn side, and (b) on the dusk side. Note that the dates of MENCA measurements are also shown. The seasonal mean is computed by averaging the densities measured in MY 33 and those measured between Ls=0° and Ls=120° in MY 34.

the SZA variation. Between SZA of 88° and 100°, the average value of the 'seasonal mean' densities is 1.15 × 107 cm-3 and that of the PEDE-2018 is 3.17 × 107 cm-3. This shows that on the dusk side the densities during PEDE-2018 are ˜2.7 times that of the seasonal mean values. On 29 June, which is close to the peak of the dust activity, the densities are 6.45 times those of the seasonal mean values. Thus, the thermospheric densities during PEDE-2018 are, on average, 2-3 times greater than those of the seasonal mean values and are as high as 6.45 times at the peak of the dust activity. Furthermore, the dust related density enhancements are slightly larger on the dusk side than on the dawn.

Figures 4.8a and 4.8b show the residual Ar densities during PEDE-2018 after removing the SZA contribution. Here the SZA contribution is removed by subtracting the seasonal mean densities from those of PEDE-2018 at each SZA (that are shown in Figure 4.7). After removing the SZA contribution, the residual densities on the dawn side show clear enhancement associated with PEDE-2018. The temporal evolution of densities on both the dawn and dusk sides is nearly same and have similar variation as that of PEDE-2018. Particularly evident are the intermittent enhancements of the densities observed between 13-16 June and on 29 June.

4.3.4 O/CO_2

In this section, we study the altitude variation of O/CO_2 ratios on the dawn and dusk sides using the densities measured by NGIMS and MENCA, respectively. The ratios are useful to understand the radiative cooling of the thermosphere at 15 μm which takes place due

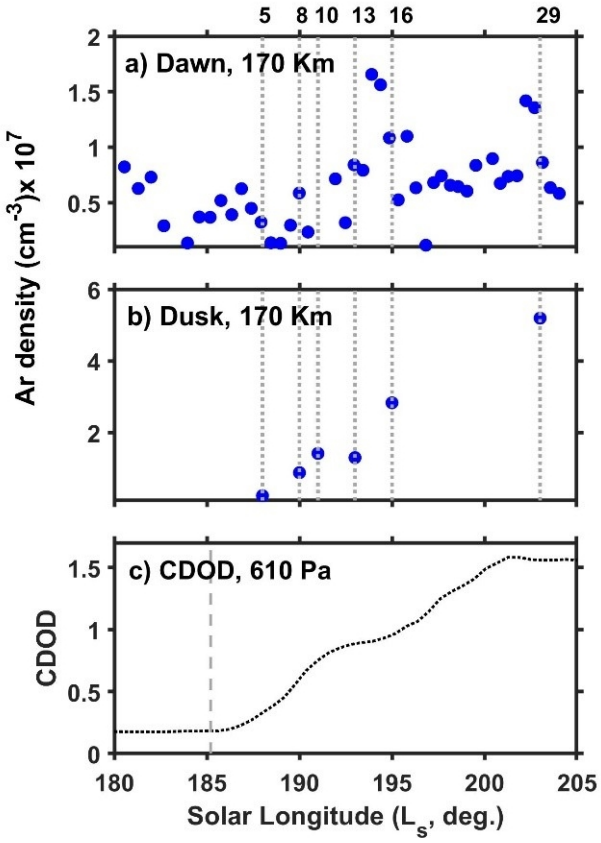

Figure 4.8: Solar longitude (Ls) variation of residual Ar densities at 170 km measured by (a) NGIMS/MAVEN and (b) MENCA/MOM spacecraft. The residual densities are obtained by removing the seasonal mean densities at each SZA from those measured during PEDE-2018. The dotted grey lines represent the dates when MENCA measurements were made. (c) Ls variation of CDOD at 610 Pa. Vertical line at the bottom panel indicates the time of onset of the PEDE-2018.

to collisions between O and CO_2 (e.g., [214]). Figure 4.9 shows the O/CO_2 ratios on the dawn and dusk sides for all the six days. Note that here we use the original densities (not the binned ones). On the dawn side, the ratios are becoming one above 185 km. On the dusk side, however, the ratios at all heights are < 0.2.

4.4 Discussion

The results of the present study suggest that thermospheric densities on both dawn and dusk sides are enhanced during PEDE-2018. PEDE-2018 has its onset around 01 June 2018 and peaked between the end of June and 10 July, 2018 [224, 218, 220]. Accordingly, the observations of the present study fall in the initial and growth phases of PEDE-2018.

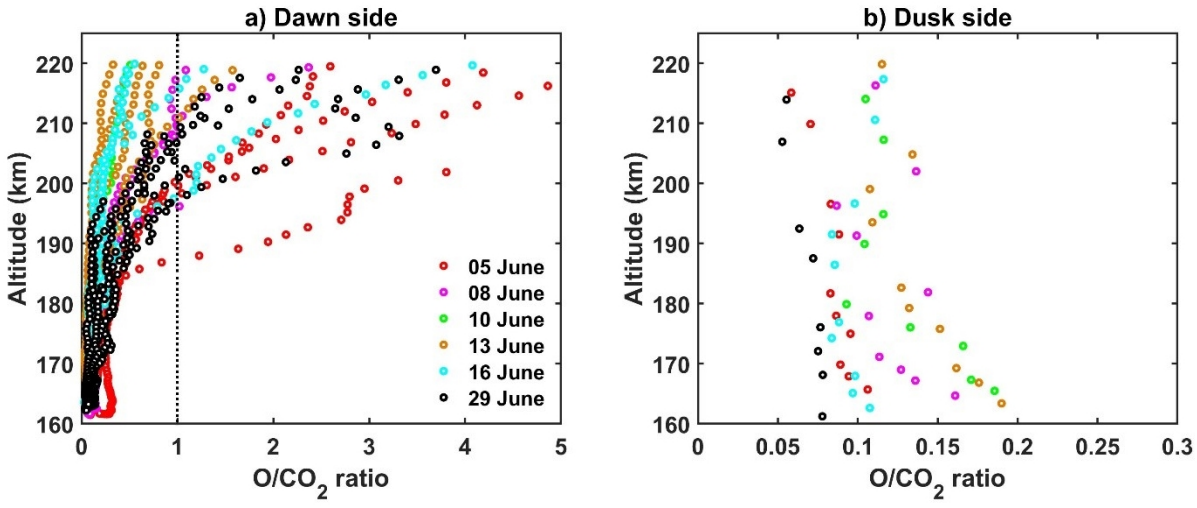

Figure 4.9: Ratios between O and CO_2 densities (a) on the dawn side measured by NGIMS/MAVEN and (b) at the dusk terminator measured by MENCA/MOM on 05, 08, 10, 13, 16 and 29 June 2018. The dotted vertical line in the left panel is plotted where the O/CO_2 ratio is one.

In addition, the deep convective activity associated with PEDE-2018 was mostly confined to low- and mid-latitude regions during 9-29 June, 2018 [225]. From Figure 4.1 and Tables 4.1 and 4.2 of the present study, it can be noted that the observations reported here are also confined to low-latitude regions. Furthermore, [224] have shown that the temperatures in the lower and middle atmosphere (25-80 Km) are enhanced during PEDE-2018. Hence, it is likely that the thermosphere probed by MAVEN and MOM was affected by the deep convective activity associated with PEDE-2018. In fact, previous studies have reported the PEDE-2018 related warming of the thermosphere and associated changes in the circulation pattern and neutral densities on the dawn side [31, 32]. In addition, it was reported that the local dust storms can also affect the Martian thermosphere [89, 128]. Thus, the enhancement in densities reported in the present study concur with those of previous studies. Accordingly, the hydrostatic expansion of the thermosphere, associated with radiative heating of the dust aerosols in the lower atmosphere, is most likely playing an important role in the enhancement of thermospheric densities (e.g., [31, 28, 32, 89, 226].

From the present study it is apparent that the density enhancement associated with PEDE-2018 is more on the dusk side than on the dawn side. Note that the densities in the thermosphere are, in general, higher on the dusk side than on the dawn side, known as the dawn-dusk asymmetry [223]. [223] have studied the dawn-dusk asymmetry statistically using long-term observations. Since the dawn and dusk observations in that study were from

different seasons, it was not possible to remove the seasonal bias. The near simultaneous observations of the present study show that during the growth phase of PEDE-2018, not only that the dawn-dusk asymmetry is retained, but it got intensified. The dusk/dawn ratios shown by [223] lie between 2 and 6, while that of the present study, on average, is 3.5. The low value is possibly because the dawn and dusk observations in the present study are not exactly from conjugate local times. Corresponding to 17.79 – 18.45 hr on the dusk side, the conjugate local times on the dawn side would be 5-6 hr [223]. But the dawn side observations during PEDE-2018 shown in the present study are between 7-8 hr (except 29 June). It is known that the thermospheric densities increase from dawn towards noon [223, 4, 125]. As a result, the dusk/dawn ratios in the present study are slightly smaller than those reported in [223]. The exception is observed on 29 June when the dusk side densities exceed those on the dawn side by one order. This is because the dawn and dusk observations on 29 June fall exactly at conjugate local times (˜ 6 LT on the dawn side and ˜ 18 LT on the dusk side; Tables 4.1 and 4.2). Furthermore, the observations of the present study are in line with the results of the global circulation model which predict the dawn-dusk asymmetry to be maximum at equatorial locations [3, 209].

Mars Climate Sounder observations have shown that the dust activity during the PEDE-2018 has a distinct diurnal variation with the dust reaching highest altitudes in the late afternoon hours and lowest altitudes in the late nights [218]. In addition, Thermal Imaging System (THEMIS) infrared observations show that evening temperatures are larger than morning temperatures during the initial and growth phases of PEDE-2018 [220]. Following these, we surmise that asymmetrical heating and uplifting of the thermosphere on the dawn and dusk terminators likely resulted in the stronger response of the thermospheric densities at the dusk than at the dawn. In addition, changes in the thermospheric circulation associated with PEDE-2018 (e.g., [32] are likely playing important role in the differential uplifting of the thermosphere on dawn and dusk sides.

In addition, it is important to note that during growth phase of PEDE-2018 there are intermittent enhancements in thermospheric densities. Significant enhancements are observed during 13-16 June (SZAs of 70°-71°) and on 29 June (SZAs of 89°-90°). Interestingly, these enhancements are present both on the dawn and dusk sides. Notably, the deep convection in the lower atmosphere during PEDE-2018 also displays the episodic nature [225]. Hence, it is likely that the strong episodes of deep convection drive the intermittent warming of the thermosphere resulting in such enhancements in deep convection. In addition, the roles of thermospheric circulation and atmospheric dynamics (such as thermal tides, planetary waves and gravity waves) cannot be neglected. The exact mechanism, how-

ever, need to be singled out with more observations and using general circulation models.

Furthermore, the present study also shows that O/CO_2 ratios at the dawn terminator become one above 185 km, whereas at the dusk terminator they are always < 0.2 below 220 km. Using NGIMS observations in MY33, [223] have shown that below 170 km the O/CO_2 ratio becomes one at the dawn terminator, but not at the dusk. The dawn and dusk observations in that study, however, are from different seasons. The simultaneous observations of neutral densities on the dawn and dusk sides in the present study unambiguously confirms this result. This can also be noted from MENCA exospheric observations, which showed that the O/CO_2 ratios at the dusk terminator become 1 at 270±10 km [109]. All these results consistently indicate that the radiative cooling of the thermosphere is prominent on the dawn side and not so significant on the dusk side.

Chapter 5

Latitudinal and Seasonal Asymmetries of the Helium Bulge in the Martian Upper Atmosphere

The thermospheric variability we investigated in chapter 3-4 was brought out using Ar and CO_2, a heavy mass species, measurements from the NGIMS/MAVEN. Here, we present the structure of thermosphere with respect to the light mass species in the region. In the present study, we investigate the characteristics of helium [He] bulges in the Martian upper atmosphere using He densities and winds measured by the Neutral Gas and Ion Mass Spectrometer (NGIMS) aboard the Mars Atmosphere and Volatile EvolutioN (MAVEN) spacecraft. The observations are compared with those predicted by the Mars Global Ionosphere Thermosphere Model (M-GITM). The results of the present study show that the nightside He bulge is a persistent feature of the Martian upper atmosphere in all seasons. The He densities inside the bulges are 1–2 orders of magnitude greater than those on the dayside. In solstices, the bulges are observed in the winter polar region which is in accordance with the model predictions. In equinoxes, however, the bulges are observed to extend from mid-latitudes into the southern polar regions (>60°S), which is contrary to the model predictions at mid-latitudes. These anomalous bulges are predominantly observed in the northern spring equinox and are 10 – 30 $\times$ greater than the modelled ones. During the autumnal equinox, the observed winds depart from the modelled winds. Furthermore, the observed winds point to the southern polar regions where the bulges are observed. Thus, the results of the present study indicate that in equinoxes the regions of local vertical advection, that are responsible for the formation of the bulges, are displaced towards the southern polar regions. The results of the present study point to the need of a larger wind database from NGIMS in southern polar region, particularly during equinoxes.

5.1 Background

Thermospheric composition generally shows species dependent response to thermal and dynamical forcings. Heavier species (such as CO_2 and Ar), due to their small scale-height, show stronger response to changes in the heating than the lighter species [5]. Since CO_2 is the dominant neutral species, the thermosphere expands in regions of heating and contracts in regions of cooling. Such a response of was clearly shown in Chapter 4 during the 2018 PEDE time. The lighter species (such as He and O), on the other hand, respond more to the background circulation (zonal and meridional winds) and related vertical advection (upwelling and downwelling) leading to their accumulation at specific locations and local times [227, 5, 228, 229, 134, 230]. Therefore, He/CO_2 ratio is often used to better appreciate the He bulge in the Martian thermosphere(e.g., [131]). [134] have shown that while the vertical advection and molecular diffusion are the dominant processes for the formation of He bulge on Earth, horizontal winds contribute indirectly by maintaining the thermospheric mass continuity.

A similar process is envisaged to operate on Mars as well for the formation of the He bulge [5, 131]. Accordingly, the upwelling part of the vertical advection on the dayside leads to the depreciation of lighter species (i.e., the He/CO_2 ratio decreases). The meridional winds propagate poleward on the dayside which after crossing poles converge on the nightside. The downwelling of winds at the convergent point leads to the accumulation of lighter species (particularly helium, where He/CO_2 ratio increases) and formation of a bulge on the nightside [5, 131]. Zonal winds cause local time variations of the bulge by moving the downwelling part of the vertical advection toward morning and evening terminators. This nightside convergence point also moves latitudinally with season. During equinoxes the convergent points lie in the mid-latitudes whereas in solstices the convergence happens in the winter polar regions. Modeling studies also predicted formation of the bulges in the Martian thermosphere [5, 131].

The He bulge, in general, is referred to as the winter He bulge wherein the He densities in the winter polar region are 1-2 orders of magnitude higher than those in the summer polar region. Existence of such a winter bulge has been well reported for Earth [132, 133, 134, 135, 136, 137] and Venus [138, 139, 140]. Prior to MAVEN, the He observations on Mars were only those measured by the Extreme Ultraviolet Explorer Satellite in airglow remote sensing method [231]. Using the He measurements by the Neutral Gas and Ion Mass Spectrometer (NGIMS) onboard MAVEN, [131] reported the existence of the He bulges in the winter polar nightside. They found that the He abundance in the northern

polar winter nightside is twice that on the northern polar summer nightside. The nightside enhancements in density are a factor of 10–20 larger than the dayside depreciations. These initial observations were found to agree preliminarily with the MGITM modeling results [131].

The present study finds its importance in three major contexts. First, since the initial report of He bulge on Mars by [131], there has been a substantial amount of He data collected by MAVEN that covers a wide range of latitudes, local times, and seasons. Due to the limited data set, [131] could not establish the presence of He bulge in the southern polar winter and also could not clearly resolve the seasonal and local time variations. The present study addresses these issues with the larger data set. Second, NGIMS/MAVEN has been measuring the altitude profiles of horizontal winds in the Martian thermosphere since 2016 [197, 232]. These wind measurements span a range of local times and seasons and are useful to infer the actual circulation pattern of the Martian thermosphere. Such direct wind measurements are expected to be useful in understanding the transport of lighter species. Third, since the work of [131], there has been considerable improvement in the M-GITM code which needs to be validated with the observed He densities and winds (see Section 2.7 for more details). Considering these developments, we revisit the He bulge to get better insight on its spatial and temporal variability and to offer a more realistic explanation for its formation based on the improved M-GITM and direct wind measurements.

5.2 He densities from observations and model

The present study uses the Level 2, version 08, revision 01 density data of NGIMS database. We use the density measurements from all inbound periapsis passes starting from the Martian year (MY) 32 (solar longitude, Ls = 288°; February 11, 2015) until Ls = 230° in MY 35 (June 30, 2020). Due to instrumentation effects as mentioned in [131], we did not include the density data prior to February 15, 2015. We use NGIMS measurements of He and CO_2 densities between 160 and 300 km only. For wind observations, we used $v06_r01$ data sets of Level 3 data products from 41 campaigns that span the period from 2016 to 2020. The winds measured during both the inbound and outbound segments are used. The winds from each campaign are averaged with a similar procedure as that of [232]. The observed and modeled densities used in the present study are averaged over 5 km $\times$ 5° $\times$ 0.33 hr altitude-latitude-local solar time (LST) grids. In the present study, we have not included observations from Ls = 180° to Ls = 360° in MY 34 as there was a planet-encircling dust event (PEDE-2018) during this period and the focus of the present paper is to study the

He bulges during nominal dust conditions. The present study also uses the outputs of the MGITM model, which was discussed in Chapter 2.

5.3 Results

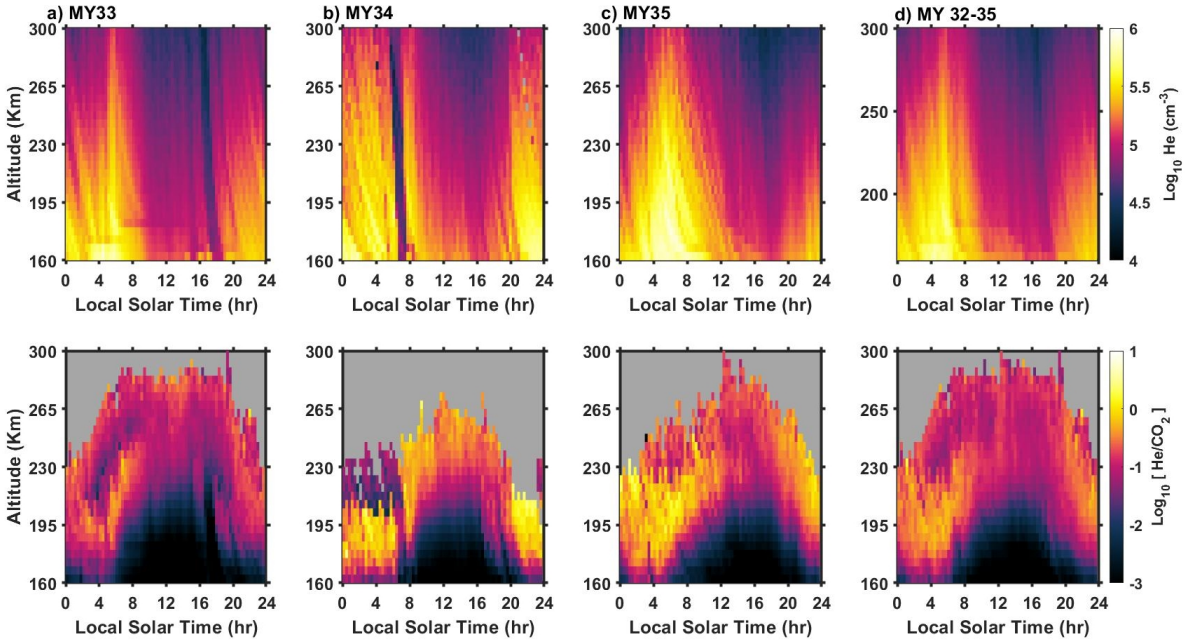

Figure 5.1: Local Solar Time (LST) versus altitude variability of (top panels) He densities and (bottom panels) He/CO_2 ratios during (a) MY 33, (b) MY 34, (c) MY 35 and (d) Average of MY 32 – 35. The data are averaged within an altitude and local time grid of 5 km × 0.33 hr.

The top panels of Figure 5.1 show the altitude versus local solar time (LST) variability of He densities. Note that as the data for MY 32 do not cover all LSTs, we do not show it separately but include it in Figure 5.1d. The patchiness in the data is mainly related to the data coverage. The low-density streaks observed at 18 hr in MY 33 and 7 hr in MY 34 are mainly due to the spread of observations in different latitudes and seasons. The diurnal variability of He shows a consistent formation of bulge on the nightside centered on ˜2 – 6 hr in all the Martian years. The strength (density) and the local time extent of the bulge, however, decrease gradually with increase in altitude. This is particularly apparent in MY 35. The He densities inside the bulges are approximately an order of magnitude higher than those observed during daytime. Since CO_2 is the dominant neutral species in the Martian thermosphere and its variation from dayside-to-nightside is opposite to that of

He [5, 131], the He bulges can be better appreciated by normalising the He densities with those of CO_2. As shown in the bottom panels of Figure 5.1, the He/CO_2 ratios show the formation of nightside He bulge at altitudes below 230 km. Above 230 km, existence of the bulge cannot be inferred due to the lower availability of CO_2 data. Note that Figure 5.1 gives a broad LST variability of He bulges but does not resolve their latitudinal or seasonal variability.

To further understand the seasonal, latitudinal and LST variability of the bulges, Figures 5.2a and 5.2b show the He/CO_2 ratios and He densities, respectively for an altitude of 200 km as a function of solar longitude (Ls). The top three panels in Figure 5.2 are color coded according to the season while the bottom panel is color coded according to LST. The seasons shown in Figure 5.2 correspond to ±45° centered on each Ls. Note that the gap from orbit #7093 to #8766 in Figure 5.2 is due to the exclusion of data during PEDE-2018. In Figure 5.2, the existence of bulge can be better appreciated in He/CO_2 than in He alone. Irrespective of season and latitude, the He/CO_2 ratio increases during nighttime and decreases during daytime. The strongest bulges (He/CO_2 >1), however, are clearly apparent in Ls = 0° (marked as E1 & E4), Ls = 90° (E3) and Ls = 180° (E2 & E5). Out of the five bulges, four bulges are observed in equinoxes (E1, E2, E4, and E5) and one bulge is observed in the southern winter. No considerable bulge is observed in Ls = 270°; however, due to limited data availability we cannot conclude on the formation/absence of the bulge in this season. By comparing with LST (Figure 5.2d), we can note that the bulges occur during nighttime, mostly in the early morning hours. Among the five bulges shown in Figure 5.2, four bulges (E1, E3, E4, E5) occur in the southern high latitudes and one (E2) in the low-latitudes. There is some enhancement of He in the northern polar region at Ls = 0° (MY 34) but the same is not reflecting as bulge in He/CO_2 ratio. Overall, no appreciable bulge is observed in the northern high latitudes, partly due to the limited sampling of winter polar region near Ls ˜ 270°

5.3.1 Local time and latitude variability

LST-latitude variation of He densities for an altitude of 200 km are presented in Figure 5.3 for four seasons. Among the four seasons, data coverage is better for Ls = 90° (12.3%) and poor for Ls = 270° (4.7%). For Ls = 0°, the densities are near maximum (of all He densities in the season) in the southern polar nighttime (between 45°S and 80°S; 3 – 8 LST). The densities are also relatively higher in the northern mid-latitudes during daytime (˜30°N – 60°N; 10 – 13 LST), but are lowest in the northern polar nighttime (˜70°N; 4 –7 hr). In the

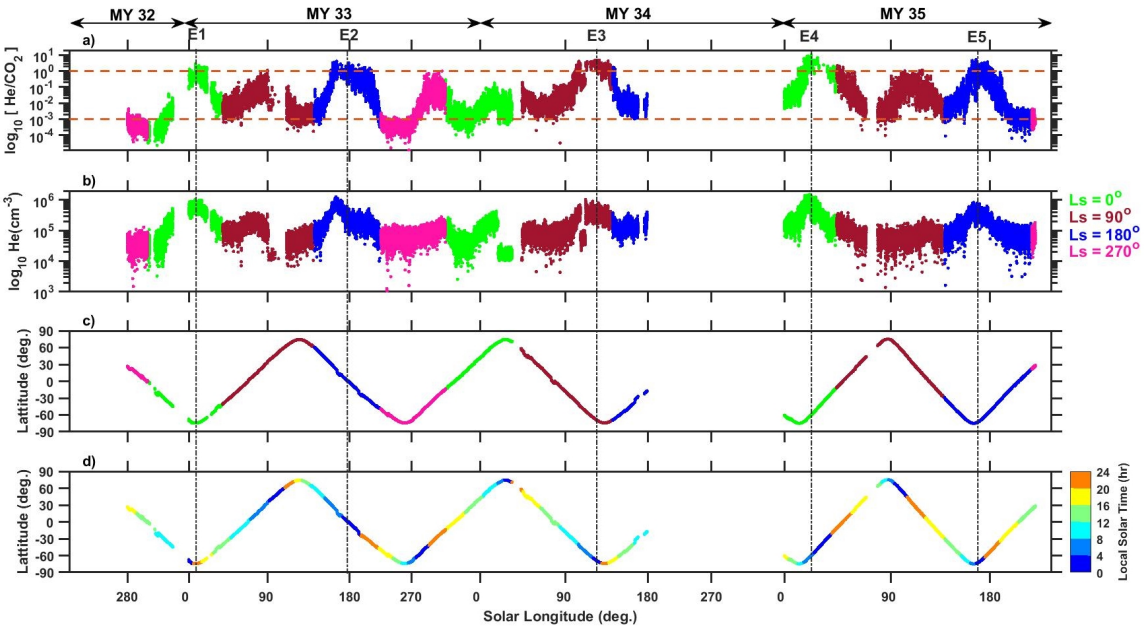

Figure 5.2: Temporal (as a function of Solar Longitude (Ls)) variation of (a) He/CO_2 ratios, (b) He density and (c) MAVEN latitude, for 200 km and color coded according to the season. Each season covers ±45° Ls. Bottom panel is color coded according to the LST. In the top panel, horizontal red dashed lines are drawn to highlight the highest and lowest values of He/CO_2 ratios. Dominant He bulges are indicated by E1 to E5

northern summer solstice (Ls = 90°), the densities are near maximum in the southern high latitude nighttime (50°S – 80°S, 0 – 7 hr) and are minimum in the northern high-latitudes. For Ls = 180°, the densities are near maximum in the northern equatorial to mid-latitudes during nighttime (10°N – 30°N; 4 – 7 hr). The densities are also relatively higher in the southern high latitude nighttime (˜60°S – 80°S; 1 – 8 hr). Much cannot be inferred from the density variation in Ls = 270°, except that the densities in the southern high latitudes are relatively smaller compared to those in Ls = 90°. Thus, in the northern summer solstice (Ls = 90°), the He bulge seems to form in the winter polar region (˜50 – 80°S) whereas in equinoxes (Ls = 0° and = 180°) the bulges are not confined only to mid-latitudes but are extended to southern polar regions. Similar conclusions can be drawn about the bulges from He/CO_2 ratios (Figure 5.4) which show much better contrasts in their variability. Note that the seasons considered here correspond to ± 45° centered at each seasonal cardinal point (Ls=0°, 90°, 180° and 270°). Reducing the duration will not change the results (c.f. figure 5.2) but will lead to reduced data coverage in each season.

M-GITM predictions of the He bulges (color contours) and horizontal winds (yellow arrows) for an altitude of 200 km for the four seasons are shown in Figure 5.5. In the

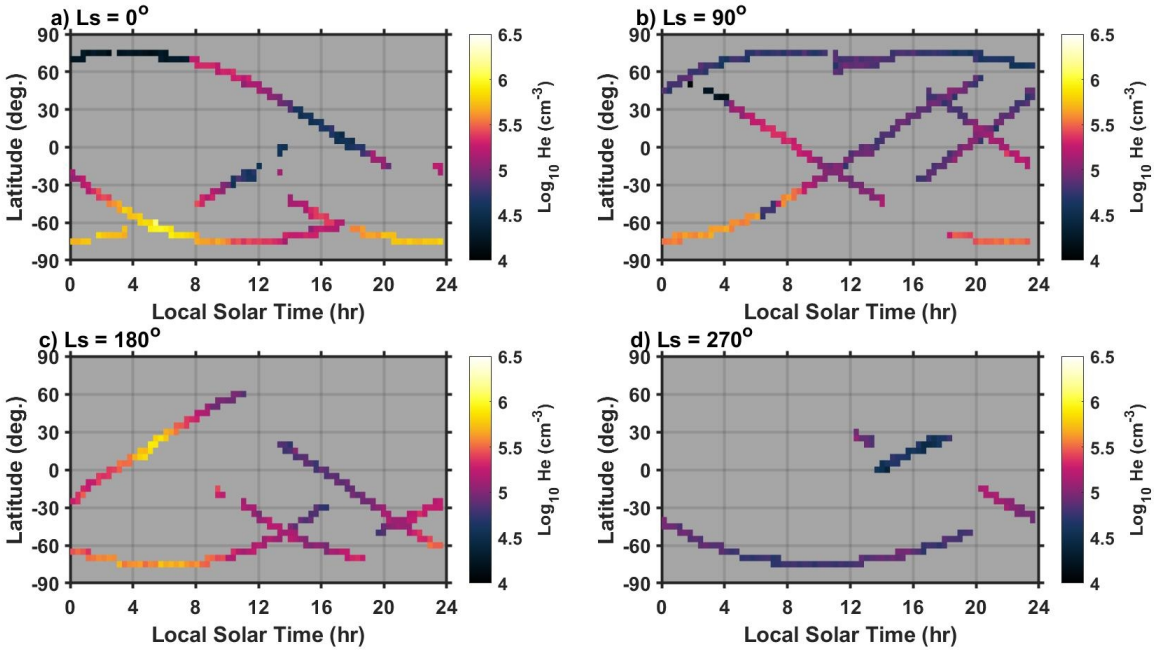

Figure 5.3: a) Latitude versus LST variation of He density for (a – d) Ls 0°, 90°, 180°, and 270° as observed by NGIMS at 200 km. The data are averaged on a latitude and local time grid of 5° × 0.33 hr.

equinoxes (Ls = 0° and 180°), the bulges are observed between 1 – 5 hr at mid-latitudes (20 – 60°) with nearly equal strength on both the hemispheres. In solstices (Ls = 90° and 270°), the strongest bulges are observed in the winter polar nighttime. In Ls = 90°, there is a distinct (yet weak) second bulge between low- and mid-latitude regions in the northern hemisphere. Such a distinct secondary bulge, however, is not apparent at Ls = 270° but a continuous streak from the winter mid-latitudes to summer low-latitudes is observed. In addition, the winter bulge in solstices extends to pre-midnight hours and the extended portion of the bulges is stronger in Ls = 270° than in Ls = 90°. The modelled horizontal winds seem to converge in regions of the bulges. Comparing the modelled bulges in Figure 5.5 with the observed ones in Figure 5.4, we can note that the latitude and local time of predicted bulge differ from those of observed ones.

5.3.2 Comparison of observations with model outputs

To get a better understanding on the discrepancies in the location of the bulges in different seasons, the observed (green arrows) and modelled (yellow arrows) horizontal winds are also shown in Figure 5.6. The modelled winds are taken from those LST-latitude grids

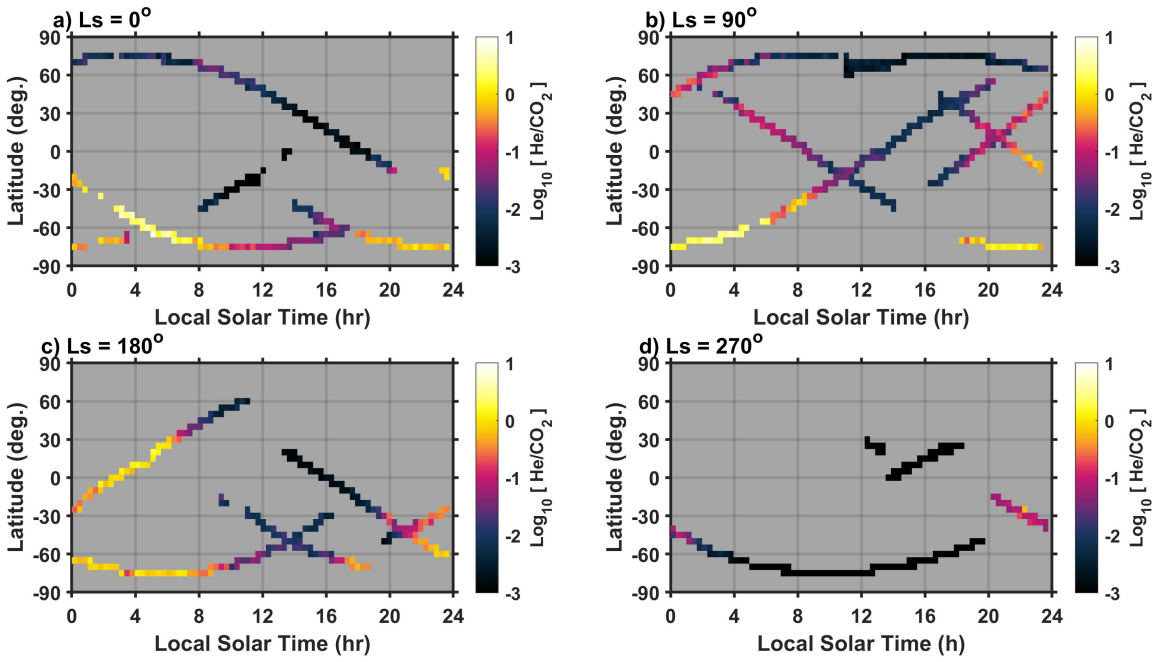

Figure 5.4: Similar to Figure 5.3, but for He/CO_2 ratios.

where the observations are available. The observed winds correspond to an altitude range of 200±10 km whereas the modelled winds correspond to a constant altitude of 200 km. With the limited wind observations, we can note that in Ls = 0° the winds are mainly observed from equatorial and northern mid-latitudes whereas the bulges are observed in the southern hemisphere high latitudes. Thus, no firm conclusions regarding wind convergence in the southern polar night can be drawn. However, in Ls = 180°, the magnitudes of the observed and modelled winds match well but the observed winds, in general, point toward south whereas the modelled winds are more toward south – west. Thus, in Ls = 180° the observed winds point to the regions where observed densities exceed the modelled ones. In Ls = 90°, the observed winds point in several different directions and hence it is difficult to draw any conclusions of their effect on the He density variations. Finally, only a few wind measurements are available in Ls = 270° and hence no conclusions are drawn.

5.4 Discussion

Characteristics of He bulges in the Martian thermosphere during nominal dust conditions are investigated using He densities and horizontal winds measured by the MAVEN NGIMS during 2015 – 2020 and 2016 – 2020, respectively and the modern M-GITM simulations.

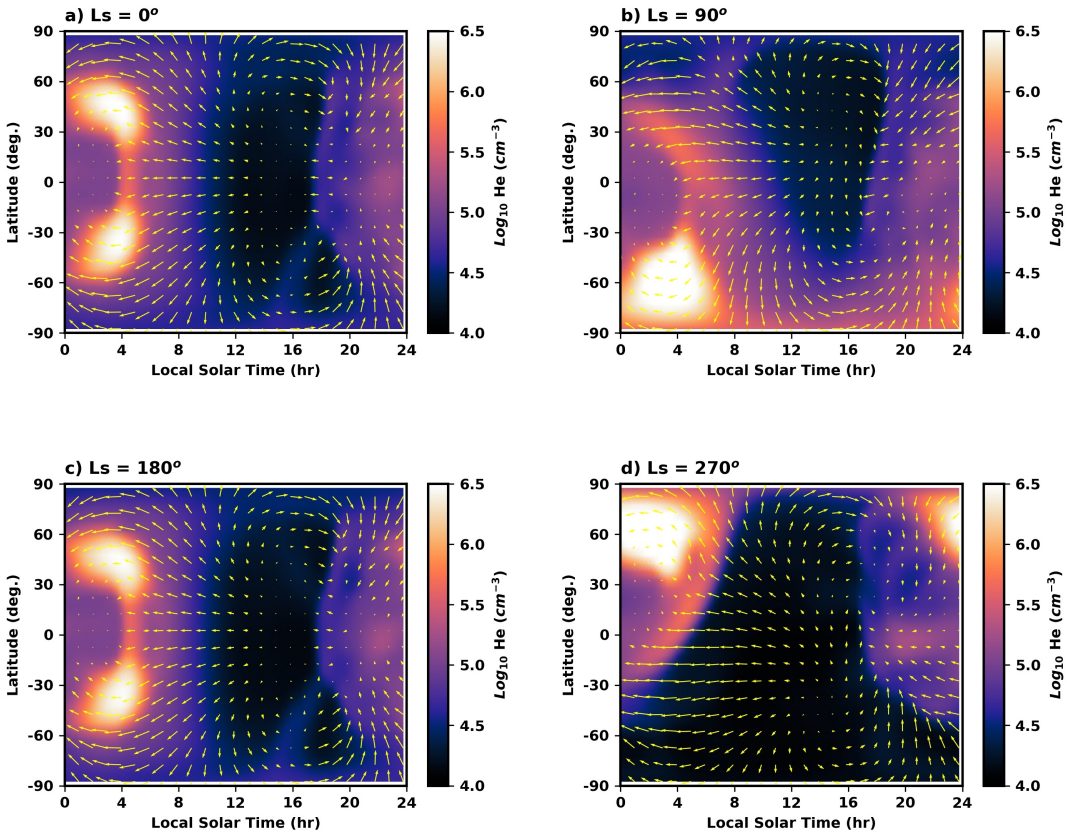

Figure 5.5: Similar to Figure 5.3, but the He densities shown are from M-GITM simulations for nominal dust conditions. The arrows show the modeled horizontal winds.

The following are the salient results of the present study.

- In equinoxes, the He bulges are observed to extend from mid-latitudes into the southern polar regions (>60°S). Such an extension to polar latitudes is less obvious in the northern hemisphere, partly due to limited observations.
- M-GITM predicts the formation of the bulges in the winter polar nightside latitudes (˜45 – 80°) during solstices and in the mid-latitude (˜20 – 60°) nightside in the equinoxes. The observed He densities in the southern polar regions (>60°S) in equinoxes are thus unexpected and are 10 – 30x greater than the modelled ones.
- The observed winds during the autumnal equinox (Ls = 180°) point to the direction of the observed He bulges whereas the modelled winds are slightly offset.
- Winter polar bulge is clearly observed in the southern polar regions at Ls = 90° as predicted. Such a winter polar bulge, however, could not be observed in the northern

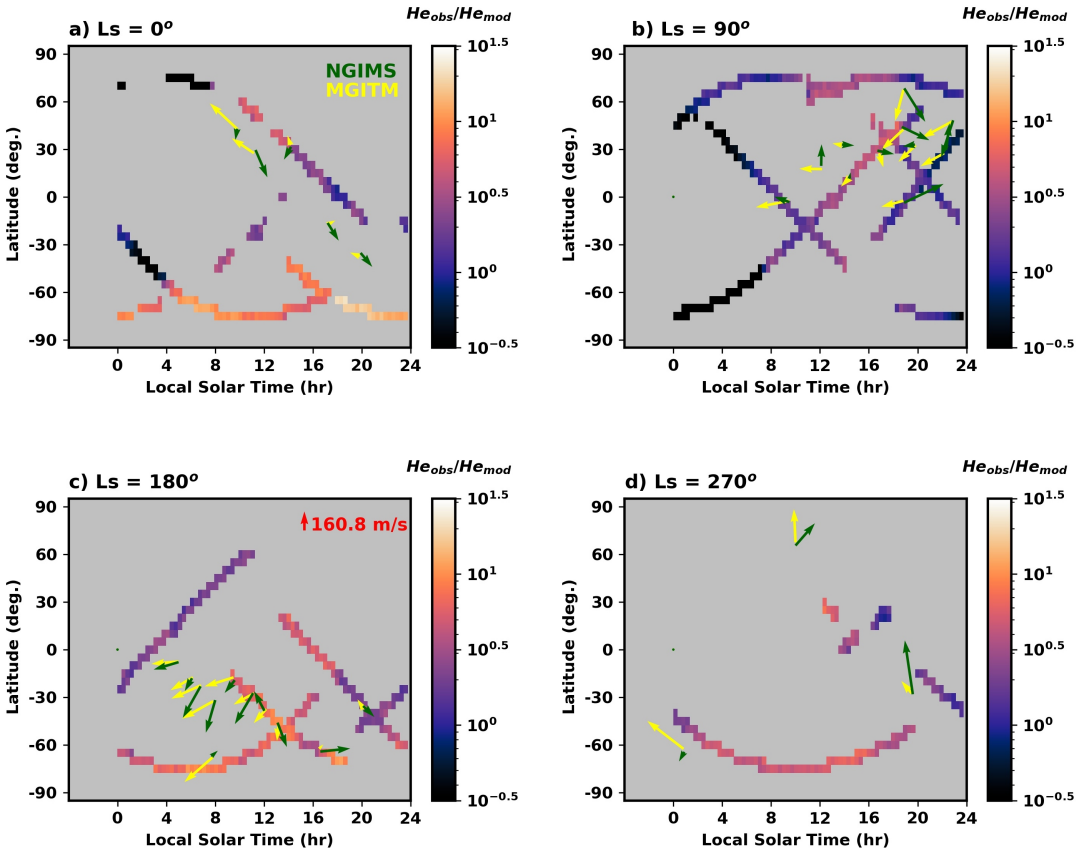

Figure 5.6: Similar to Figure 5.3 but shows the ratios of the observed and modelled He densities (shown by colorbar). The green and yellow arrows represent the winds observed by NGIMS and modelled by M-GITM, respectively. Tails of the arrows show the location of the winds, length of the arrows show the magnitude (reference magnitude is shown by red arrow in panel c) and heads of the arrows point to the direction of the winds.

polar regions at Ls = 270°, partly due to limited observations.

As predicted by models [5] and previously reported from NGIMS observations [131], He bulges are a persistent feature of the nightside Martian thermosphere. The densities inside the bulges are 1 – 2 orders higher than the dayside minimum densities. Similar to that observed at the Earth [134, 233], the He bulges on Mars are strongly seasonal dependent. Particularly, M-GITM predicts their formation at mid-latitudes (˜20 – 60°) in equinoxes and at the winter poles (˜45 – 80°) in solstices. For Earth, the local vertical advection and molecular diffusion are shown to be primary drivers of the bulge formation [134, 233]. The seasonally varying horizontal winds contribute indirectly as their divergence on the dayside and convergence on the nightside drive the local vertical advection. Similar processes are likely to work on Mars as well [131].

In the entire MAVEN dataset, the northern winter pole was observed only twice: in MY 32 and MY 34. The initial observations of MAVEN (MY 32) were reported by [131] wherein their usage was cautioned due to possible instrumentation effects. As mentioned earlier, the MY 34 northern winter observations fall under PEDE-2018 which we did not include in the present study. As a result, we could not observe the He bulge in the northern winter polar region. The formation of the bulge in the northern winter pole reported by [131], however, is as predicted by the M-GITM simulations. In the present study, we report the first observations of the southern winter polar bulge which was observed by MAVEN in MY 34. These observations concur with the M-GITM predictions.

The most unexpected result of the present study is the formation of the bulges in the southern polar region (>60°S) in equinoxes. Even during daytime, the He densities at the southern polar region are greater than those at mid-latitudes. In equinoxes, the M-GITM predicts the formation of bulges at mid-latitudes (˜20–60°) in both the northern and southern hemispheres. While there is also some enhancement in the mid-latitudes (30 – 60°), the most unexpected is the extension of the bulge to the southern polar region (60 – 80°S) which was clearly observed in the northern spring equinox (Ls = 0°). These bulges are in fact stronger than the one observed in the northern winter polar region by [131]. The observed helium bulges at equinoxes thus extend beyond mid-latitudes and much closer to the southern pole than predicted. From the initial observations, [131] also noted these anomalous enhancements but was attributed to the instrumental effects. The present study clearly shows that the equinoxial He bulge extending to the southern pole is a persistent feature. Even the modern M-GITM simulations could not predict these anomalous equinox enhancements. This shows that the periodic solar insolation drivers of the Mars thermospheric circulation (e.g. solar heating changes on diurnal, seasonal and solar cycle timescales) are not sufficient to capture the high latitude convergence regions of global thermospheric winds implied by the helium distribution during equinox conditions. Therefore, other non-solar processes must be investigated. These processes include upward propagating gravity waves, which are thought to deposit their momentum and energy in the thermosphere and drive substantial changes in the otherwise solar driven upper atmosphere circulation (e.g. [25]). Addressing the coupling with the lower atmosphere via gravity wave momentum and energy deposition may be helpful to reproduce the observed southern polar helium bulge during equinoxes.

A comparison between the observed and modelled horizontal winds helps to some extent in understanding the formation of the equinoxial southern polar bulges. The convergent point of the modelled horizontal winds coincides with the locations of the modelled He

bulges indicating that the horizontal winds lead to the local vertical advection. The magnitude and direction of the observed winds, however, deviates from the modelled winds. During the autumnal equinox (Ls = 180°) in particular, the observed winds point to the location of the southern polar bulge. This probably indicates that the actual location of the local vertical advection is in the southern polar region which is different from that predicted by M-GITM. To advance the present study, a larger wind database from NGIMS in the southern polar region is required, particularly during the equinoxes.

Chapter 6

Local time and Latitudinal variation of Mixing Ratios in the Martian Upper Atmosphere

6.1 Abstract

In the previous studies we investigated the spatial and temporal variability of thermospheric constituents- Ar and CO_2, which are the heavy mass species and He, which is a light mass species. The results of the previous studies clearly showed that the distribution of the thermospheric species is strongly connected to the dynamical processes which have mass dependent effect on the variability of species. Thus, in this paper, to understand and compare the mass dependent variability, we investigate the latitudinal and local time variability in the mixing ratios- He/CO_2, N_2/CO_2, and Ar/CO_2, in the thermosphere of Mars. For this purpose, we use density measurements at an altitude of 200 km, derived using the Neutral Gas Ion Mass Spectrometer onboard Mars Atmosphere and Volatile EvolutioN mission. The variability in He/CO_2 follows a trend similar to that of He density, the N_2/CO_2 and Ar/CO_2 trend opposite to their individual densities. While the observation about He and N_2 (and their mixing ratios) are consistent with previous studies, the present study reports for the first time, a comparison of mixing ratios of varying masses. In addition, we investigate the impact of dust storms (dust storm season (Ls = 180°-360°) of MY 33 and MY 34 (PEDE-2018) on mixing ratios. We found that during PEDE – 2018, there is a decrease in mixing ratios compared with the ratios during dust storm season of MY 33. The factor of depletion of mixing ratios varies with their masses. In addition, the seasonal trend in mixing ratios exhibits an opposing trend to dust activity. The mixing ratios peak when the

dust activity is low and not at its peak. During the low dust activity period, while Ar/CO_2 shows maximum enhancement, He/CO_2 is least enhanced. The results of this study show that in general, the variability in mixing ratios is controlled by the seasonal variation in CO_2 density. On the dayside, the variability in mixing ratios seems to be driven by the seasonal changes in the homopause altitude, whereas the variability on the night side points toward the possibility of additional processes playing a role. Change in the thermospheric circulation during dust storms coupled with a mass-dependent response of thermospheric gases to gravity waves is proposed as an important mechanism contributing to the depletion of the mixing ratio.

6.2 Background

In the studies presented in chapter 3 and 4, we observed that the heavy mass species (Ar and CO_2), due to their small scale-heights, are controlled by the changes in the dynamical heating/cooling in the thermosphere [223, 5] and are strongly influenced by the global dust storms [90]. Whereas, in chapter 6, we found that the distribution of light mass species (He) is mostly influenced by the large-scale circulation (zonal and meridional winds) and related vertical advection (upwelling and downwelling). This leads to their accumulation at specific locations and local times [131, 198, 227, 5, 228, 229, 134, 230]. Thus, the previous investigations imply that the species have a mass dependent response to the dynamical processes in the thermosphere of Mars and needs further investigation.

To understand the distribution of the atmospheric species, we investigate the variability of mixing ratios (with respect to the dominant species-CO_2). [131] and [198] investigated the spatial and temporal variations in He density using He/CO_2. The global circulation of the winds combined with the vertical advection and molecular diffusion leads to strong seasonal and latitudinal variations in the He/CO_2 [5, 131, 198]. In addition, [67] observed a strong seasonal trend in N_2/CO_2 using the measurements from Infrared Ultraviolet Visible Spectrometer (IUVS) onboard Mars Atmosphere Volatile Evolution MissioN (MAVEN). They found that N_2/CO_2 reaches a maximum of 0.20 during aphelion time and a minimum of 0.02 during perihelion time. The observed variations are associated with the variations in CO_2 density and are strongly driven by the seasonal changes in homopause altitudes, as also observed by [105, 141]. Particularly the dayside variability of N_2/CO_2 is well correlated with the observed trend in homopause altitudes [67]. However, due to observational limitations of IUVS, the nightside trend in N_2/CO_2 and its relation with the seasonal changes in homopause altitude could not be investigated.

Thus, previous studies investigating the mixing ratios have shown their variability reasonably well, yet a complete understanding of the behavior of mixing ratios, particularly during the dust storm season remains unknown. In the present study, we investigate the mixing ratios - He/CO_2, N_2/CO_2, and Ar/CO_2 using the measurements from NGIMS/ MAVEN. The data sets used in this study offer more spatial and temporal coverage compared with the ones used in previous studies. Due to this, a complete latitudinal and diurnal variability is studied. In addition, NGIMS data sets from the dust storm season in MY 33 and 34 (PEDE-2018) will help to investigate and compare the response of mixing ratios to dust storms in both MYs. Further, in the present study, we show a combined picture of the mixing ratios of the species of various masses (He/CO_2,N_2/CO_2, and Ar/CO_2), thus, giving an insight into the mass-dependent nature of the thermosphere of Mars.

6.3 Results

6.3.1 Seasonal Vs Local time variability

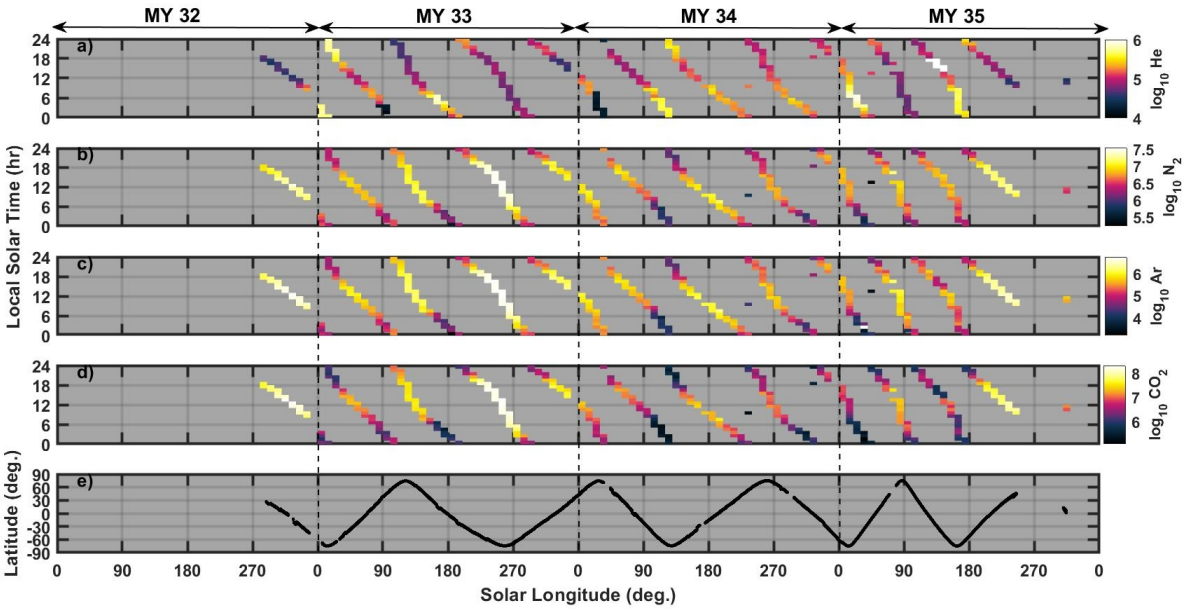

Figure 6.1: Local solar time (LST) versus solar longitude (Ls) variability of densities of a) He, b) N_2, c) Ar, d) CO_2, and e) latitude coverage of MAVEN spacecraft. The data are averaged over a grid of 1 hr in LST and 10° in Ls.

Figure 6.1 (a-d) represents the Local Solar Time (LST) versus Solar Longitude (Ls) variation of He, N_2, Ar and CO_2 densities, respectively for an altitude of 200 km. Irre-

spective of season and latitude, the He densities show a consistent diurnal variability with enhancement on the nightside and early morning hours (0–6 h and 22-24 h) and depletion on the dayside centred on 12–14 h in all the Martian years. The maxima in densities are at mid-high latitudes (between 45°S and 80°S) during equinoxes (Ls = 0° and Ls =180°) and at high latitudes (>60°S) during southern winter solstice (Ls = 90°). The enhancements in He density are consistent with the results of the study by [131, 198]. However, the variability of N_2, Ar and CO_2 clearly show an opposite variation as compared to He. The N_2, Ar and CO_2 abundances are larger on the dayside as compared with the nightside regions of Mars. The N_2, Ar and CO_2 densities attain their respective maxima in MY 33 between 10°S and 50°S latitudes during southern summer solstice (Ls = 270°) and minima at the mid-high latitudes (between 45°S and 80°S) during equinoxes and high latitudes (>60°S) during southern winter. Comparing MY 33 with MY 34, during Ls = 180° to Ls = 270°, one can see that the He densities during MY 34 are smaller, and N_2, Ar and CO_2 densities are larger than those observed during MY 33. Note that, during MY 34, Ls = 180° to Ls = 270°, a Planet Encircling Dust Event (PEDE) also known as PEDE-2018, occurred on Mars. The NGIMS measurements from the period of PEDE-2018 show an enhancement in the heavy mass species (e.g., Ar and CO_2) [31, 90]. In addition, [31, 234] observed a decrease in light mass species (He and O) during PEDE-2018. Thus, the observations of the present study related to the densities of heavy and light mass species, during PEDE-2018, are consistent with the previously reported results [90, 31, 234]. To bring out the distribution of heavy and light mass species clearly, it is important to study their variabilities relative to the CO_2 density and hence their mixing ratios (as discussed in section 1).

The variability of mixing ratios He/CO_2, N_2/CO_2 and Ar/CO_2 is investigated in Figure 6.2 (a-c), respectively. From Figure 6.1a and 6.2a, it is apparent that the spatial and temporal variability of He/CO_2 is similar to variations observed in He density and consistent with the previous studies on He bulges [131, 234] in the upper atmosphere of Mars. However, the Local-time variation of N_2/CO_2 and Ar/CO_2 show a clear opposite behaviour when compared with their individual densities (N_2 and Ar) (as shown in Figure 6.1b, 1c, 1d, 2b, and 2c). The mixing ratios N_2/CO_2 and Ar/CO_2, in contrast to the day time enhancement of N_2, Ar and CO_2 densities, are maximum on the night side and minimum on the day side of Mars. Similarly, the latitudinal variability of the mixing ratios shows an opposite behaviour as compared with the latitudinal variability observed in their individual densities. The N_2/CO_2 and Ar/CO_2 are enhanced at mid-high latitudes (between 45° and 80°S) during equinoxes (Ls = 0° and Ls = 180°) and high latitudes (>60°S) during southern winter (Ls = 90°). This behaviour is more in line with the He and He/CO_2 variabilities. The seasonal

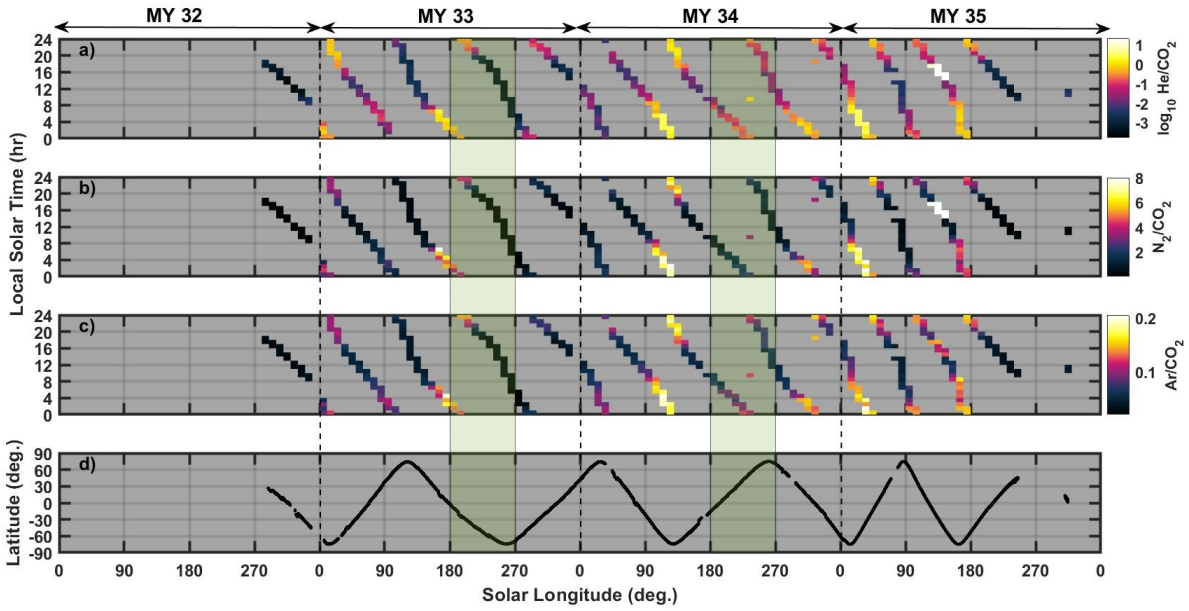

Figure 6.2: Similar to Figure 1, but color coded with mixing ratios- a) He/CO_2, b) N_2/CO_2, and c) Ar/CO_2. Panel d) represents the latitude coverage by MAVEN spacecraft. Here, green shaded boxes are used to highlight the dust storm season (Ls 180°-270°) in MY 33 and MY 34

variability of the mixing ratios is further investigated in Figure 6.3

6.3.2 Local time Vs latitude variability

In NGIMS, N_2 densities are derived from mass channel number 28 that collects detector counts for CO density as well. Further, a CO_2 molecule can get fragmented into C, CO, O_2 and O within the instrument. Thus, channel number 12, 16, 28, 32 and 44 have to be considered while deriving CO_2 abundance. Thus, deriving N_2 density from N_2+CO counts and CO_2 density by accounting for its fragmented species leads to higher uncertainty in the data retrieval process. Ar, on the other hand is a more reliable specie since it is chemically non-reactive and does not fractionate. Thus, we study the variability in the mixing ratios using Ar/CO_2 (as shown in Figure 6.3). Figure 6.3 includes data from all MYs (32-35) and averaged over a 5°x1 h grid. Here each season is defined in the ± 45° range which is centred at cardinal points Ls = 0°, Ls = 90°, Ls = 180° and Ls = 270°. For example, Ls = 90°, includes data from Ls = 45° to Ls = 135°. Note that the observations corresponding Ar/CO_2 are also applicable to He/CO_2 and N_2/CO_2. During Ls = 0°, the Ar/CO_2 approaches maximum on the southern polar nightside (between 45° and 80°S; 3–8 LST) of the Mars.

Ar/CO_2 is also relatively higher on the northern polar nightside during (70°N; 0–4 hr) and southern polar nightside (60° - 80°S; 19–24 hr), but is lowest in the daytime (10-14 hr) at most of the latitudes. In the northern summer solstice (Ls = 90°), Ar/CO_2 approaches maximum in the southern high latitude nightside (50°–80°S, 0–7hr), and are minimum in the northern high-latitudes except at 50°–70°N, 0–4 hr at which time there is slight enhancement in Ar/CO_2. For Ls = 180°, Ar/CO_2 approaches maximum in the northern equatorial to mid-latitudes on the nightside (10°–30°N; 4–7 hr). Ar/CO_2 is also relatively higher on the southern high latitude nightside (60°–80°S; 1–8 hr). During Ls = 270°, Ar/CO_2 is maximum on mid-latitude region of the nightside (10-20° N; 3-5 hr) of Mars and minimum in southern high latitudes. Note that the enhancement in Ar/CO_2 during southern winter (Ls = 90°) is stronger than in the northern winter (Ls = 270°). Thus, the variability observed in Ar/CO_2 is similar to the one observed for He density and He/CO_2 ratio by [131, 234, 198] and for N_2/CO_2 by [67].

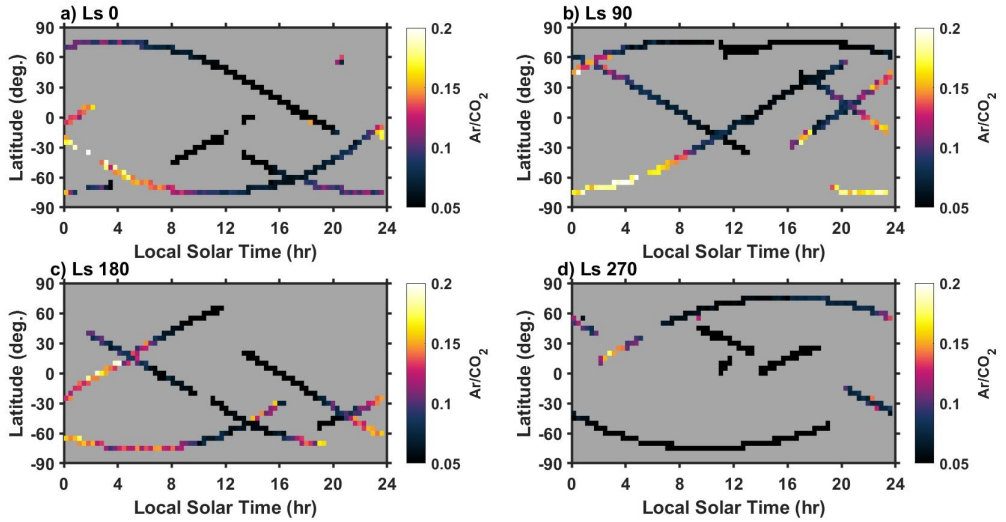

Figure 6.3: Latitude versus local solar time variation of Ar/CO_2 for (a–d) Ls=0°, Ls=90°, Ls=180°, and Ls=270° for 200 km. The data are averaged over a latitude and local time grid of 5° × 0.33 hr.

6.3.3 Dust Storm induced variability

In this section we discuss the observations related to the dust storm seasons of MY 33 and 34. In Figure 6.2, on comparing Ls=180° - 270° in MY 33 with 34 (as shown by shaded boxes) one can note a reduction in He/CO_2 by 1-2 orders of magnitude during MY 34. Interestingly, during PEDE-2018, N_2/CO_2 and Ar/CO_2 also show a decrease in their

ratios as compared with ratios in the dust storm season of MY 33. The value of N_2/CO_2 decreases from ˜4.5 in MY to ˜3 during PEDE-2018. Similarly, Ar/CO_2 decreases from ˜0.18 to ˜0.09. Thus, the factor by which the mixing ratios deplete is maximum for He/CO_2 and minimum for Ar/CO_2. Although the comparison of dust storm season of MY 33 and 34 is at slightly different local times and latitudes, the depletion in mixing ratios show a significant influence of dust storm on the mixing ratios. Dust storms occur more frequently during Ls=180° – 270°, where the peak phase of dust activity lasts for 5-20 days. The data in this Figure, is grided for every 10° Ls. This averages out the Ls dependent variability of the mixing ratios. Thus, Ls-to-Ls of mixing ratios during the dust storm season (Ls = 180° to Ls = 270°) is investigated in Figure 6.4.

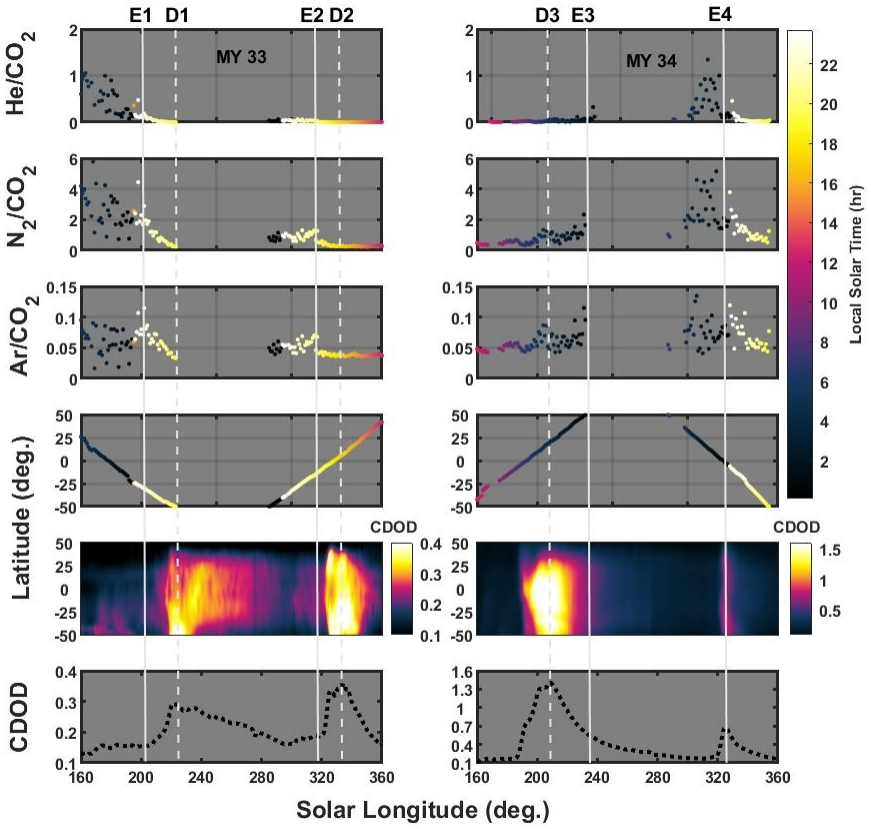

Figure 6.4: Temporal (as a function of solar longitude (Ls)) variation of, during MY 33 (left column) and MY 34 (right column) (a) He/CO_2 ratios, (b) N_2/CO_2 ratios (c) Ar/CO_2 ratios, (d) MAVEN latitude, for 200 km e) latitude versus Ls variation of CDOD values, and f) CDOD values averages over latitudes 50N to 50S. The solid vertical lines are drawn to highlight the enhancements in the mixing ratios- He/CO_2 ratios. Dashed vertical lines are drawn to highlight dust storm peaks

From Figure 6.4 d), one can see that during MY 33, MAVEN spacecraft was moving from northern mid-latitudes towards the southern high latitudes of Mars and in MY 34 the spacecraft was moving the southern-mid latitudes to northern high latitudes of. During MY 33, MAVEN covered mostly nightside region of Mars, whereas during MY 34, in addition to nightside, the dayside of the Mars was also observed. While, during MY 34 PEDE-2018 engulfed 80-95% of the globe of Mars, during MY 33, a regional dust storm swirled through the planet that covered a latitude region between 50°N to 50°S of Mars. This provided an opportunity to study the behaviour of mixing ratios in the nightside mid-latitude region during the dust storm season on Mars. The Column Dust Optical Depth (CDOD) shown in Figure 6.4e and 4f is an indicator of the dust opacity in the atmosphere of Mars. Higher the CDOD, higher the amount of dust lifted in the atmosphere. While Figure 6.4e shows the latitude versus solar longitude variation in CDOD values, in Figure 6.4f the CDOD values are averaged over the latitude region between 50°N and 50°S.

In Figure 6.4, the dashed lines D1, D2 and D3 represents the strong dust activity at Ls = 220° – 240° and Ls = 320° – 340° in MY 33, and Ls = 190° – 210° in MY 34, respectively. The solid lines E1, E2, E3, and E4 show the enhancements in mixing ratios between Ls = 160° - 200° and Ls = 280° - 330° in MY 33 and Ls = 225° - 245° and Ls = 300° - 330° in MY 34, respectively. The maximum dust activity occurred at D3 (CDOD = 1.5). However, the maximum enhancement in the mixing ratios is attained at E4. The He/CO_2, N_2/CO_2 and Ar/CO_2 during E4 are by a factor of 90, 3.33, 1.5, respectively, larger than those during D3. Similarly, In MY 33, the peak of the dust storm is at D2. However, the peak in the mixing ratios is observed at E1. Thus, it is apparent that the mixing ratio increases with the decrease in dust activity and suggest an anti-correlated with the CDOD trend. In addition, during MY 34, the latitude region between 10°S - 50°S, was observed during 12 hr – 14 hr LT (Ls = 160 ° to Ls = 190°) and during 20 hr – 23 hr LT (Ls = 330° to Ls = 360°). On comparing, one can clearly see that the mixing ratios on the nightside are larger than those on the dayside. Although no such conclusion can be drawn from MY 33, the observed local time variability during the dust storm season is consistent with the non-dust seasons.

6.4 Discussion

Latitudinal and local time variabilities in the mixing ratios - He/CO_2, N_2/CO_2 and Ar/CO_2 are investigated in the upper atmosphere of Mars, at an altitude of 200 km. The study is carried out using the He, N_2, Ar and CO_2 measurements by MAVEN NGIMS for MY 32, MY 33, MY 34 and MY 35. The density of heavy mass species (N_2, Ar and CO_2)

on the dayside are larger than those on the nightside, while the light mass species (He) is enhanced on the nightside of the Mars. The density of heavy mass species is maximum in the summer hemisphere and minimum in the winter hemisphere of Mars. However, He is enhanced over mid-high latitudes during equinoxes (Ls = 0° and Ls 180°) and at high latitudes during southern winter solstice (Ls = 90°). Further, during PEDE-2018 (Ls = 160° to Ls = 360°, MY 34), N_2, Ar and CO_2 densities are increased with respect to MY 33, due to the radiative heating in the lower atmosphere and subsequent expansion of the upper atmosphere of Mars. However, He densities during PEDE – 2018 were found to be decreased. The depletion of light mass species, is associated with the changes in upper atmospheric circulation. In contrast, the results of the present study show that the mixing ratios – He/CO_2, N_2/CO_2, and Ar/CO_2 are enhanced on the nightside and depleted on the dayside of the Mars. During solstices, the mixing ratios are maximum at the high-latitude regions of winter hemisphere of Mars. The mixing ratios are larger during southern winter (Ls = 90°) than those during the northern winter (Ls = 270°). During the dust storm season, the mixing ratios on the nightside mid-latitude regions, show an opposite behavior as compared with the CDOD. Particularly, during MY 34, with an increase in CDOD value from 0.6 to 1.6, the He/CO_2, N_2/CO_2 and Ar/CO_2 decreases by a factor of 90, 3.33 and 1.5 times, respectively.

The local time and latitudinal variability of the Martian upper atmospheric heavy and light mass species is consistent with previous NGIMS observations [125, 223, 198, 67, 131, 234, 90] and Mars Global Ionosphere-Thermosphere Model (M-GITM) simulations [5]. Also, the variability of the mixing ratio- He/CO_2 and N_2/CO_2 is in accordance with the result of the previous studies. The variability in He/CO_2 was investigated using measurements from NGIMS/MAVEN. The upwelling of winds on the dayside and their downwelling on the nightside, combined with large-scale circulation, is the primary driver of the variability in He/CO_2 [131, 234, 198]. The investigation of N_2/CO_2 using IUVS/MAVEN observations by [67] showed that trend in N_2/CO_2 is mostly driven by the seasonal changes in the homopause altitude due to seasonal fluctuation in the atmospheric CO_2 density. Particularly on the dayside, the trend in N_2/CO_2 is anti-correlated with the homopause altitude and a direct dependence on the variation in CO_2 density at 140 km was shown. However, due to limited observations from the nightside, a complete picture of the local time variability of the mixing ratio, particularly during nightside, could not be investigated. Further, the observations reported in the study were up to May, 2018 which is before the start of PEDE-2018. Therefore, no inference was drawn with respect to the response of mixing ratio during dust storm season. In addition, the present study shows that the trend in mixing

ratios during Ls = 160° to Ls = 360°, dust storm season, of MY 33 and 34, are anticorrelated with the CDOD values. During PEDE-2018 (MY 34), on the nightside, as the dust storm progresses, the maximum decrease is observed in Ar/CO_2 and minimum decrease is observed in He/CO_2. Previously, [235] studied the variability of O and H airglow using Hisaki Space Telescope Observations. They reported a strong dependence of atmospheric O on solar flux and no correlation with CDOD values. In addition, they observed an enhancement in H from non-dusty to dusty season and a strong correlation between H and CDOD values. However, the correlation becomes weaker for CDOD > 0.2. The present study, however, brings out a complete picture of the variability in the mixing ratios of varying mass species. The response of mixing ratios toward dust activity is now clear. During the dust storm season, in addition to light mass species, heavy mass species also have anticorrelation with the CDOD values. With the increase in dust activity, the factor by which the mixing ratio decreases varies with the varying mass.

To understand the observed variability in the mixing ratios, it is important to examine the possible mechanisms that lead to the enhancement in mixing ratios during nightside winter polar regions. [67] listed three possible mechanisms. Seasonal variation in a) thermospheric temperature, b) N_2/CO_2 at the surface and c) homopause altitudes. However, they ruled out the possibility of the effect of a) and b). They found that on the dayside, the seasonal change in homopause altitude is the dominant driver of the variability in mixing ratios. We re-investigated the correlation between the variability of the mixing ratio, the homopause altitude and atmospheric CO_2 density, using Ar/CO_2 measurements at an altitude = 200 km in Figure 6.5a. Methodology to derive the homopause altitudes is discussed in section 2.5. On the dayside the homopause altitude ranges from ˜100 – 140 km and on the nightside it ranges from ˜90 – 120 km. Thus, the ˜30 km diurnal variation in homopause altitude is consistent with [67]. On the dayside (8 – 20 hr LT), the trend in the Ar/CO_2 is opposite to the trend in the homopause altitudes and there is a slow decrease in Ar/CO_2 mixing ratio with an increase in homopause altitude. However, on the nightside (0 – 8 hr LT and 20 – 24 hr LT) the trend in Ar/CO_2 shows a slight positive correlation with the trend in homopause altitude. Further, on the dayside, the trend in homopause altitudes show a direct correlation with CO_2 density variation (as shown in Figure 6.5b). This shows that the dayside variability in mixing ratio is dependent on the seasonal variation in the CO_2 density. However, on the nightside an opposite variation between the mixing ratio and CO_2 is apparent. Thus, the coherence of the mixing ratio with the homopause altitudes, on the dayside of Mars is consistent with those observed by [67]. However, the variability of the mixing ratios on the nightside of Mars upper atmosphere is a new observation. The result of

the present study shows that the variability on the nightside of the Mars upper atmosphere is independent of the variability of homopause altitude. Thus, in addition to the variations in CO_2 density, there are additional processes contributing to the distribution of the species.

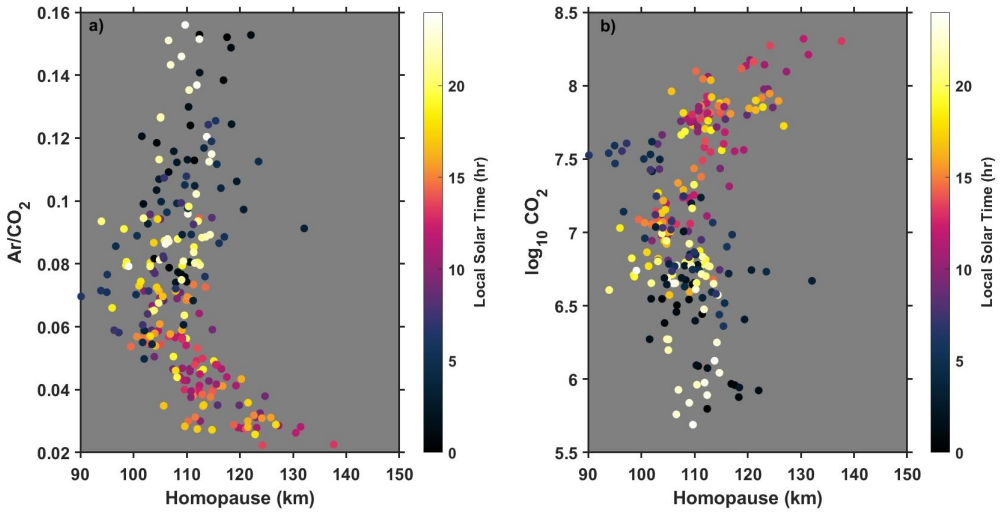

Figure 6.5: a) Variability (as a function of homopause altitudes) in Ar/CO_2 ratios, and b) CO_2 density. The data points are color coded with the Local Solar Time.

Recently, studies simulated the effect of gravity waves on the global circulation using Mars Global Ionosphere Thermosphere Model (MGIT-M) code and reported that gravity waves induce a reversal/ reduction in the large-scale circulation. [91] reported a strong enhancement in gravity waves amplitudes during PEDE-2018. Thus, during the dust storm season, when dust activity approaches its peak phase, GW amplitude also increases, which in turn slows down the wind circulation. Reduced circulation means reduced day-to-night transfer of the atmospheric species. As the dust activity enters its declining phase, wind fields try to restore their previous day-night flow, resulting in an increase in the mixing ratios during low dust activity period. Further, [119] demonstrated that the gravity waves derived from Ar and CO_2 were out of phase with those derived from N_2. This shows that the varying depletion factors for varying mass species could be due to the mass-dependent response of the thermosphere.

Thus, we propose that a combination of the changes in the atmospheric circulation during dust storm season and mass dependent behavior of thermospheric species is responsible for the observed variability in mixing ratios. This requires further investigation in future studies based upon the continuous monitoring of the temporal evolution of dust storms and corresponding response of the mixing ratios. Finally, the result of the present study has sig-

nificant implication in estimation of the escape rates of the gases of varying masses during the dust storm season, as the variations in mixing ratios in the vicinity of exobase altitude (˜200 km) where species can easily escape from, can cause variations in the escape rates as well.

Chapter 7

Summary, Conclusions and Implications

In this dissertation, a comprehensive picture of the spatial (latitudinal and altitudinal) and temporal (diurnal and seasonal) variability of the thermospheric region is presented. Each research work (Chapters 3 – 6) undertaken in this dissertation stands on its own with a major result, but intrinsically all the works aim to address the central theme of Mars thermosphere variability. This research work has answered a diverse set of questions about the thermosphere of Mars and has improved our understanding of the region. The following paragraphs summarise the salient outcomes and conclusions of all the works presented in Chapters 3-6 and present the major implications of this thesis.

We analysed the upper atmospheric species of varied masses using satellite enabled in-situ measurements of densities, scale heights, and horizontal winds. For this, we used the mass spectrometer measurements from Neutral Gas Ion Mass Spectrometer onboard Mars Atmosphere Volatile Evolution Mission spacecraft and Mars Exosphere Neutral Composition Analyser onboard Mars orbiter Mission spacecraft. The results of the study show that the thermosphere of Mars exhibits a consistent asymmetry with respect to the temporal distribution of heavier species like Ar and CO_2. While the Ar densities are found to be higher in dusk terminator, they are found to be depleted in the dawn terminator region. The simultaneous measurements during Ls = 188° to Ls = 205° (MY 34) of both the terminator regions, not only confirms the presence of dawn-dusk asymmetry in densities, scale heights and temperatures, but also brings out the effect of PEDE-2018 on the asymmetry. We found that during PEDE-2018, the dusk densities are further enhanced making the dawn-dusk asymmetry much more prominent than during nominal times. This investigation is further extended by tracing the lighter species such as He. An accumulation of He densities in night time winter polar regions during solstice (Ls = 90°) and southern high latitudes during equinoxes (Ls = 0° and Ls = 180°) is observed. A comparison with MGITM simulations of He density and winds with corresponding measurements

from NGIMS shows that the model is not able to predict the equinoctial bulges. Moreover, the observed enhancements are found to be consistent with the observed wind directions. We also studied the latitudinal and local time variations in the mixing ratios – He/CO_2, N_2/CO_2 and Ar/CO_2. This study not only confirms the previously reported spatial and temporal variability of the mixing ratios, but also provide a comparative view of the variability of varying masses. In addition, this study clearly shows that during dust storm season, a combination of the changes in the atmospheric circulation and mass dependent behavior of thermospheric species significantly alter variability of mixing ratios. Thus, this study clearly shows that the compositional structure of the thermosphere of Mars is not only governed by solar activity but also significantly influenced by the dynamical processes.

This dissertation serves as a platform to extend existing studies to further our understanding of the thermosphere of Mars and to begin new studies. Since the upper atmosphere is the reservoir volatiles that escape from Mars, and it is also home to tracer species that reflect lower atmospheric processes such as dust storms and gravity waves, the implication of this thesis can be broadly said to propagate both upward and downward.

On the atmospheric escape front, decoding the evolution and escape of the Martian atmosphere requires an understanding of the atmosphere below the exobase, and how it connects to the lower atmosphere. The processes that replenish, drive and remove species from the topmost region of Mars have not been fully revealed. In addition, variability of atmospheric species (molecules) near the surface is not reflected in the upper atmospheric regions where atoms dissociated from these species escape. To illustrate the multi-variate approach required to tackle this problem, let us consider the challenge of understanding water loss. The properties of water reservoirs in the subsurface, in polar caps, and in the near-surface atmosphere vary significantly with Martian season. The water that is lifted upwards by circulation is affected by ice, water clouds and dust. Insolation and atmospheric chemistry contribute to ionizing and dissociating water molecules into its constituent ions and atoms, thus forcing the entry of electric and magnetic fields into the problem and altering the physical drivers that affect water dynamics and further propagation to higher altitudes. In addition, gravity waves, dust storms and space weather events also tend to modify atmospheric properties. The results reported in this thesis are carried out in the altitude region between 150 – 220 km. Previous studies have shown that the exobase altitude, above which species are more likely to escape the atmosphere of Mars, exhibits large spatial and temporal variations between 140-220 km. This points towards the possibility of propagation of the observed asymmetries (in the vicinity of exobase) to the various escape processes. Since the upper atmosphere is after all the source for the escape, this thesis

finds its importance in terms of understanding the asymmetric behaviour of various loss processes. Thus, to understand and answer problems as complex as the one highlighted earlier, this thesis provides useful tools and insights.

Another interesting tangent that can develop from this dissertation include the study of isotopic ratios and their variability in the upper atmosphere of Mars. This study has strongly brought out the mass dependent aspect of the thermosphere of Mars. The atmospheric species- Ar and CO_2, that have only 10% mass difference show mass dependent variability. Isotopes are the elements that have same atomic number but different mass number. Several studies have shown that with increase in altitude isotopic ratios increases. For example, a factor of 6 enrichment in the D/H ratio in water vapor, as compared to the terrestrial ratio [236] was one of the first clues to the discovery that mars almost certainly was episodically wet and atmospherically dense in the past. Similarly, $^{18}O/^{16}O$ ratio in water vapor was reported by [237] using Curiosity lander measurements and by [238] using ExoMars Trace Gas Orbitor (TGO). This happens due to loss of lighter mass isotope to space. The linkage between the isotopic fractionation and photochemical escape has also been reported using model simulations. [143]. However, the results of this dissertation clearly suggest that the present understanding of Isotopic fractionation, a strong indicator of atmospheric escape, needs to be updated by investigating the mass dependent response of the isotopes to various atmospheric drivers. Several years of MAVEN observations and vast improvements in models presents a unique opportunity to work on these problems.

Also, this study clearly shows that the observed asymmetries are largely the result of the effect of dynamical processes such as heating/cooling by gravity waves and global circulation in the upper atmosphere of Mars. However, the general circulation models that are developed (till date) for Mars are predominantly based on the solar radiations related processes. Thus, the result of this study will help in developing/improving the GCMs by refining the effect of non-solar processes. In addition, the distribution of heavy and light mass species observed in this research work clearly shows that the mass of the species plays an important role in understanding their spatial and temporal variability. This in turn implies that the mass of the species is an important parameter to be taken into consideration while investigating any dynamical process and hence escape processes. Thus, this thesis lays a ground for improvising the methods to quantify various escape, dynamical and solar processes by considering the mass dependence nature of the thermosphere of Mars.

Finally, due to slow precession trajectory of MAVEN and MOM, the measurements from NGIMS and MENCA are sparse in space and time, yet sufficient to bring out meaningful scientific results. However, the scanty data sets restrained us from bringing out few

details and globalizing our results. For example, while the observed winds during Ls = 180° are well correlated with the presence of anomalous He bulges (in Chapter 5), we could not comment about the discrepancies observed in other seasons due to insufficient wind observations. Thus, a global coverage of wind observations will help in understanding such discrepancies in all the seasons. Thus, larger, high resolution and continuously monitored (in time) data sets combined with more robust GCMs will aid in better understanding the thermosphere of Mars.

Bibliography

[1] G. Martínez, C. Newman, A. De Vicente-Retortillo, and et al, "The modern near-surface martian climate: A review of in-situ meteorological data from viking to curiosity," *Space Science Review*, vol. 212, p. 295–338, 2017. [Online]. Available: https://doi.org/10.1007/s11214-017-0360-x

[2] R. Haberle, R. Clancy, F. Forget, M. Smith, and R. Zurek, Eds., *The Atmosphere and Climate of Mars*, ser. Cambridge Planetary Science. Cambridge University Press, 2017. [Online]. Available: https://doi.org/10.1017/9781139060172

[3] S. Bougher, B. Jakosky, J. Halekas, J. Grebowsky, J. Luhmann, P. Mahaffy, J. Connerney, F. Eparvier, R. Ergun, D. Larson, J. McFadden, D. Mitchell, N. Schneider, R. Zurek, C. Mazelle, L. Andersson, D. Andrews, D. N. Baird, D. Baker, and R. Yelle, "Early maven deep dip campaign reveals thermosphere and ionosphere variability," *Science*, 2015. [Online]. Available: https://doi.org/10.1126/science.aad0459

[4] P. R. Mahaffy, M. Benna, M. Elrod, R. V. Yelle, S. W. Bougher, S. W. Stone, and B. M. Jakosky, "Structure and composition of the neutral upper atmosphere of mars from the maven ngims investigation," *Geophysical Research Letters*, vol. 42, no. 21, pp. 8951–8957, 2015. [Online]. Available: https://doi.org/10.1002/2015GL065329

[5] S. W. Bougher, D. Pawlowski, J. M. Bell, S. Nelli, T. McDunn, J. R. Murphy, M. Chizek, and A. Ridley, "Mars global ionosphere-thermosphere model: Solar cycle, seasonal, and diurnal variations of the mars upper atmosphere," *Journal of Geophysical Research: Planets*, vol. 120, no. 2, pp. 311–342, 2015. [Online]. Available: https://doi.org/10.1002/2014JE004715

[6] B. Jakosky, R. Lin, J. Grebowsky, J. Luhmann, D. Mitchell, G. Beutelschies, T. Priser, M. Acuna, L. Andersson, Baird, and et al., "The Mars Atmosphere

and Volatile Evolution (MAVEN) Mission," *Space Science Reviews*, vol. 195, no. 1-4, pp. 3–48, Dec. 2015. [Online]. Available: https://doi.org/10.1007/s11214-015-0139-x

[7] P. R. Mahaffy, M. Benna, T. King, D. N. Harpold, R. Arvey, and M. e. a. Barciniak, "The neutral gas and ion mass spectrometer on the mars atmosphere and volatile evolution mission," *Space Science Reviews*, vol. 195, p. 49–73, 2014. [Online]. Available: https://doi.org/10.1007/s11214-014-0091-1

[8] B. Jakosky and R. Phillips, "Mars' volatile and climate history," *Nature*, vol. 12,412(6843),237-44, 2001. [Online]. Available: https://doi.org/10.1038/35084184

[9] H. H. Kieffer, B. M. Jakosky, C. W. Snyder, and M. S. Matthews, Eds., *Mars*. Tuscon, AZ, USA: Arizona University Press, 1992. [Online]. Available: https://doi.org/10.1029/2006JE002816

[10] R. M. Haberle, *MARS: ATMOSPHERE*. Dordrecht: Springer Netherlands, 1997, pp. 432–441. [Online]. Available: https://doi.org/10.1007/1-4020-4520-4_238

[11] P. L. Read and S. R. Lewis, *The Martian climate revisited: atmosphere and environment of a desert planet*, ser. Springer Praxis Books: Geophysical Sciences. Springer, 2004, vol. 26.

[12] H. H. Kieffer, "Soil and surface temperatures at the viking landing sites," *Science*, vol. 194, no. 4271, pp. 1344–1346, 1976. [Online]. Available: https://www.science.org/doi/abs/10.1126/science.194.4271.1344

[13] V. Baker, R. Strom, V. Gulick, J. Kargel, G. Komatsu, and V. Kale, "Ancient oceans, ice sheets and the hydrological cycle on mars," *Nature*, vol. 352, no. 6336, pp. 589–594, 1991.

[14] L. Ojha, M. B. Wilhelm, S. L. Murchie, A. S. McEwen, J. J. Wray, J. Hanley, M. Massé, and M. Chojnacki, "Spectral evidence for hydrated salts in recurring slope lineae on mars," *Nature Geoscience*, vol. 8, no. 11, pp. 829–832, 2015.

[15] P. H. Smith, L. Tamppari, R. Arvidson, D. Bass, D. Blaney, W. V. Boynton, A. Carswell, D. Catling, B. Clark, T. Duck *et al.*, "H2o at the phoenix landing site," *Science*, vol. 325, no. 5936, pp. 58–61, 2009.

[16] M. Acuna, J. Connerney, P. a. Wasilewski, R. Lin, K. Anderson, C. Carlson, J. McFadden, D. Curtis, D. Mitchell, H. Reme *et al.*, "Magnetic field and plasma observations at mars: Initial results of the mars global surveyor mission," *Science*, vol. 279, no. 5357, pp. 1676–1680, 1998.

[17] H. Melosh and A. Vickery, "Impact erosion of the primordial atmosphere of Mars," *nature*, vol. 338, no. 6215, pp. 487–489, Apr. 1989.

[18] S. L. Hess, J. A. Ryan, J. E. Tillman, R. M. Henry, and C. B. Leovy, "The annual cycle of pressure on mars measured by viking landers 1 and 2," *Geophysical Research Letters*, vol. 7, no. 3, pp. 197–200, 1980. [Online]. Available: https://doi.org/10.1029/GL007i003p00197

[19] P. B. James, H. H. Kieffer, and D. A. Paige, "The seasonal cycle of carbon dioxide on Mars." in *Mars*, M. George, Ed., 1992, pp. 934–968.

[20] P. M. Woiceshyn, "Global seasonal atmospheric fluctuations on mars," *Icarus*, vol. 22, no. 3, pp. 325–344, 1974. [Online]. Available: https://doi.org/10.1016/0019-1035(74)90181-X

[21] F. Hourdin, P. L. Van, F. Forget, and O. Talagrand, "Meteorological variability and the annual surface pressure cycle on mars," *Journal of Atmospheric Sciences*, vol. 50, no. 21, 1993. [Online]. Available: https://journals.ametsoc.org/view/journals/atsc/50/21/1520-0469_1993_050_3625_mvatas_2_0_co_2.xml

[22] J. E. Tillman, N. C. Johnson, P. Guttorp, and D. B. Percival, "The martian annual atmospheric pressure cycle: Years without great dust storms," *Journal of Geophysical Research: Planets*, vol. 98, no. E6, pp. 10 963–10 971, 1993.

[23] N. J. Kelly, W. V. Boynton, K. Kerry, D. Hamara, D. Janes, R. C. Reedy, K. J. Kim, and R. M. Haberle, "Seasonal polar carbon dioxide frost on mars: Co2 mass and columnar thickness distribution," *Journal of Geophysical Research: Planets*, vol. 111, no. E3, 2006. [Online]. Available: https://doi.org/10.1029/2006JE002678

[24] D. Hinson, R. Simpson, J. Twicken, G. Tyler, and F. Flasar, "Erratum: "initial results from radio occultation measurements with mars global surveyor"," *Journal of Geophysical Research*, vol. 105, 01 2000. [Online]. Available: https://doi.org/10.1029/1999JE900045

[25] A. S. Medvedev and E. Yiğit, "Thermal effects of internal gravity waves in the martian upper atmosphere," *Geophysical Research Letters*, vol. 39, no. 5, 2012. [Online]. Available: https://doi.org/10.1029/2012GL050852

[26] R. J. Wilson, "Evidence for nonmigrating thermal tides in the mars upper atmosphere from the mars global surveyor accelerometer experiment," *Geophysical Research Letters*, vol. 29, no. 7, pp. 24–1–24–4, 2002. [Online]. Available: https://doi.org/10.1029/2001GL013975

[27] D. P. Hinson, R. J. Wilson, M. D. Smith, and B. J. Conrath, "Stationary planetary waves in the atmosphere of mars during southern winter," *Journal of Geophysical Research: Planets*, vol. 108, no. E1, 2003. [Online]. Available: https://doi.org/10.1029/2002JE001949

[28] F. G. lez Galindo, M. A. Lopez-Valverde, F. Forget, M. Garcia-Comas, E. Millour, and L. Montabone, "Variability of the martian thermosphere during eight martian years as simulated by a ground to exosphere global circulation model," *Journal of Geophysical Research*, vol. 120, pp. 2020–2035, 2015.

[29] E. M. B. Thiemann, F. G. Eparvier, L. A. Andersson, C. M. Fowler, W. K. Peterson, P. R. Mahaffy, S. L. England, D. E. Larson, D. Y. Lo, N. M. Schneider, J. I. Deighan, W. E. McClintock, and B. M. Jakosky, "Neutral density response to solar flares at mars," *Geophysical Research Letters*, vol. 42, no. 21, pp. 8986–8992, 2015.

[30] S. Bougher, S. Rafkin, and P. Drossart, "Dynamics of the venus upper atmosphere: Outstanding problems and new constraints expected from venus express," *Planetary and Space Science*, vol. 54, no. 13, pp. 1371–1380, 2006, the Planet Venus and the Venus Express Mission. [Online]. Available: https://doi.org/10.1016/j.pss.2006.04.023

[31] M. K. Elrod, S. W. Bougher, K. Roeten, R. Sharrar, and J. Murphy, "Structural and compositional changes in the upper atmosphere related to the pede-2018 dust event on mars as observed by maven ngims," *Geophysical Research Letters*, vol. 47, no. 4, p. e2019GL084378, 2020. [Online]. Available: https://agupubs.onlinelibrary.wiley.com/doi/abs/10.1029/2019GL084378

[32] S. K. Jain, S. W. Bougher, J. Deighan, N. M. Schneider, F. González Galindo, A. I. F. Stewart, R. Sharrar, D. Kass, J. Murphy, and D. Pawlowski, "Martian

thermospheric warming associated with the planet encircling dust event of 2018," *Geophysical Research Letters*, vol. 47, no. 3, p. e2019GL085302, 2020. [Online]. Available: https://doi.org/10.1029/2019GL085302

[33] J. S. Evans, M. H. Stevens, J. D. Lumpe, N. M. Schneider, A. I. F. Stewart, J. Deighan, S. K. Jain, M. S. Chaffin, M. Crismani, A. Stiepen, W. E. McClintock, G. M. Holsclaw, F. Lefèvre, D. Y. Lo, J. T. Clarke, F. G. Eparvier, E. M. B. Thiemann, P. C. Chamberlin, S. W. Bougher, J. M. Bell, and B. M. Jakosky, "Retrieval of co2 and n2 in the martian thermosphere using dayglow observations by iuvs on maven," *Geophysical Research Letters*, vol. 42, no. 21, pp. 9040–9049, 2015.

[34] D. C. Fritts and M. J. Alexander, "Gravity wave dynamics and effects in the middle atmosphere," *Reviews of Geophysics*, vol. 41, no. 1, 2003. [Online]. Available: https://doi.org/10.1029/2001RG000106

[35] G. Gilli, F. Forget, A. Spiga, T. Navarro, E. Millour, L. Montabone, A. Kleinböhl, D. M. Kass, D. J. McCleese, and J. T. Schofield, "Impact of gravity waves on the middle atmosphere of mars: A non-orographic gravity wave parameterization based on global climate modeling and mcs observations," *Journal of Geophysical Research: Planets*, vol. 125, no. 3, p. e2018JE005873, 2020. [Online]. Available: https://agupubs.onlinelibrary.wiley.com/doi/abs/10.1029/2018JE005873

[36] J. E. Creasey, J. M. Forbes, and D. P. Hinson, "Global and seasonal distribution of gravity wave activity in mars' lower atmosphere derived from mgs radio occultation data," *Geophysical Research Letters*, vol. 33, no. 1, 2006. [Online]. Available: https://doi.org/10.1029/2005GL024037

[37] D. P. Hinson and R. J. Wilson, "Temperature inversions, thermal tides, and water ice clouds in the martian tropics," *Journal of Geophysical Research: Planets*, vol. 109, no. E1, 2004. [Online]. Available: https://doi.org/10.1029/2003JE002129

[38] S. Tellmann, M. Pätzold, B. Häusler, D. P. Hinson, and G. L. Tyler, "The structure of mars lower atmosphere from mars express radio science (mars) occultation measurements," *Journal of Geophysical Research: Planets*, vol. 118, no. 2, pp. 306–320, 2013. [Online]. Available: https://doi.org/10.1002/jgre.20058

[39] L. Wang, D. C. Fritts, and R. H. Tolson, "Nonmigrating tides inferred from the mars odyssey and mars global surveyor aerobraking data," *Geophysical Research Letters*, vol. 33, no. 23, 2006. [Online]. Available: https://doi.org/10.1029/2006GL027753

[40] J. E. Creasey, J. M. Forbes, and G. M. Keating, "Density variability at scales typical of gravity waves observed in mars' thermosphere by the mgs accelerometer," *Geophysical Research Letters*, vol. 33, no. 22, 2006. [Online]. Available: https://doi.org/10.1029/2006GL027583

[41] D. C. Fritts, L. Wang, and R. H. Tolson, "Mean and gravity wave structures and variability in the mars upper atmosphere inferred from mars global surveyor and mars odyssey aerobraking densities," *Journal of Geophysical Research: Space Physics*, vol. 111, no. A12, 2006. [Online]. Available: https://doi.org/10.1029/2006JA011897

[42] A. S. Medvedev, E. Yiğit, and P. Hartogh, "Estimates of gravity wave drag on mars: Indication of a possible lower thermospheric wind reversal," *Icarus*, vol. 211, no. 1, pp. 909–912, 2011. [Online]. Available: https://doi.org/10.1016/j.icarus.2010.10.013

[43] E. Yiğit, S. L. England, G. Liu, A. S. Medvedev, P. R. Mahaffy, T. Kuroda, and B. M. Jakosky, "High-altitude gravity waves in the martian thermosphere observed by maven/ngims and modeled by a gravity wave scheme," *Geophysical Research Letters*, vol. 42, no. 21, pp. 8993–9000, 2015. [Online]. Available: https://doi.org/10.1002/2015GL065307

[44] E. Yiğit, A. S. Medvedev, A. D. Aylward, P. Hartogh, and M. J. Harris, "Modeling the effects of gravity wave momentum deposition on the general circulation above the turbopause," *Journal of Geophysical Research: Atmospheres*, vol. 114, no. D7, 2009. [Online]. Available: https://doi.org/10.1029/2008JD011132

[45] "The solsticial pause on mars: 1. a planetary wave reanalysis," *Icarus*, vol. 264, pp. 456–464, 2016. [Online]. Available: https://doi.org/10.1016/j.icarus.2015.08.039

[46] S. D. Guzewich, E. R. Talaat, and D. W. Waugh, "Observations of planetary waves and nonmigrating tides by the mars climate sounder," *Journal of Geophysical Research: Planets*, vol. 117, no. E3, 2012. [Online]. Available: https://doi.org/10.1029/2011JE003924

[47] D. Banfield, B. Conrath, M. Smith, P. Christensen, and R. Wilson, "Forced waves in the martian atmosphere from mgs tes nadir data," *Icarus*, vol. 161, no. 2, pp. 319–345, 2003. [Online]. Available: https://doi.org/10.1016/S0019-1035(02)00044-1

[48] K. L. Cahoy, D. P. Hinson, and G. L. Tyler, "Radio science measurements of atmospheric refractivity with mars global surveyor," *Journal of Geophysical Research: Planets*, vol. 111, no. E5, 2006. [Online]. Available: https://doi.org/10.1029/2005JE002634

[49] G. M. Keating, S. W. Bougher, R. W. Zurek, R. H. Tolson, G. J. Cancro, S. N. Noll, J. S. Parker, T. J. Schellenberg, R. W. Shane, B. L. Wilkerson, J. R. Murphy, J. L. Hollingsworth, R. M. Haberle, M. Joshi, J. C. Pearl, B. J. Conrath, M. D. Smith, R. T. Clancy, R. C. Blanchard, R. G. Wilmoth, D. F. Rault, T. Z. Martin, D. T. Lyons, P. B. Esposito, M. D. Johnston, C. W. Whetzel, C. G. Justus, and J. M. Babicke, "The structure of the upper atmosphere of mars: In situ accelerometer measurements from mars global surveyor," *Science*, vol. 279, no. 5357, pp. 1672–1676, 1998. [Online]. Available: https://www.science.org/doi/abs/10.1126/science.279.5357.1672

[50] T. Beer, "Supersonic generation of atmospheric waves," *Nature*, vol. 242, no. 34, 1973.

[51] J. M. Forbes and Y. Moudden, "Solar terminator wave in a mars general circulation model," *Geophysical Research Letters*, vol. 36, no. 17, 2009. [Online]. Available: https://doi.org/10.1029/2009GL039528

[52] J. M. Forbes, S. L. Bruinsma, Y. Miyoshi, and H. Fujiwara, "A solar terminator wave in thermosphere neutral densities measured by the champ satellite," *Geophysical Research Letters*, vol. 35, no. 14, 2008. [Online]. Available: https://doi.org/10.1029/2008GL034075

[53] T. Beer, "Martian terminator waves," *Nature*, vol. 252, no. 672, 1974. [Online]. Available: https://doi.org/10.1038/252672a0

[54] N. Heavens, D. Kass, A. Kleinböhl, and J. Schofield, "A multiannual record of gravity wave activity in mars's lower atmosphere from on-planet observations by the mars climate sounder," *Icarus*, p. 113630, 05 2020. [Online]. Available: https://doi.org/10.1016/j.icarus.2020.113630

[55] S. D. Guzewich, R. J. Wilson, T. H. McConnochie, A. D. Toigo, D. J. Banfield, and M. D. Smith, "Thermal tides during the 2001 martian global-scale dust storm," *Journal of Geophysical Research: Planets*, vol. 119, no. 3, pp. 506–519, 2014. [Online]. Available: https://doi.org/10.1002/2013JE004502

[56] A. Kleinböhl, R. John Wilson, D. Kass, J. T. Schofield, and D. J. McCleese, "The semidiurnal tide in the middle atmosphere of mars," *Geophysical Research Letters*, vol. 40, no. 10, pp. 1952–1959, 2013. [Online]. Available: https://doi.org/10.1002/grl.50497

[57] R. J. Wilson and S. D. Guzewich, "Influence of water ice clouds on nighttime tropical temperature structure as seen by the mars climate sounder," *Geophysical Research Letters*, vol. 41, no. 10, pp. 3375–3381, 2014. [Online]. Available: https://doi.org/10.1002/2014GL060086

[58] R. Wilson, E. Millour, T. Navarro, F. Forget, and M. Kahre, "Gcm simulations of aphelion season tropical cloud and temperature structure," *Mars Atmosphere: Modelling and Observation, 5th International Workshop*, 12 2013.

[59] D. McCleese, J. Schofield, F. Taylor, S. Calcutt, M. Foote, D. Kass, C. Leovy, D. Paige, P. Read, and R. Zurek, "Mars climate sounder: An investigation of thermal and water vapor structure, dust and condensate distributions in the atmosphere, and energy balance of the polar regions," *Journal of Geophysical Research: Planets*, vol. 112, no. E5, 2007.

[60] P. Withers, R. Pratt, J.-L. Bertaux, and F. Montmessin, "Observations of thermal tides in the middle atmosphere of mars by the spicam instrument," *Journal of Geophysical Research: Planets*, vol. 116, no. E11, 2011. [Online]. Available: https://agupubs.onlinelibrary.wiley.com/doi/abs/10.1029/2011JE003847

[61] J. M. Forbes, X. Zhang, F. Forget, E. Millour, and A. Kleinböhl, "Solar tides in the middle and upper atmosphere of mars," *Journal of Geophysical Research: Space Physics*, vol. 125, no. 9, p. e2020JA028140, 2020. [Online]. Available: https://agupubs.onlinelibrary.wiley.com/doi/abs/10.1029/2020JA028140

[62] Y. Miyoshi and H. Fujiwara, "Gravity waves in the equatorial thermosphere and their relation to lower atmospheric variability," *Earth Planets and Space*, vol. 61, pp. 471–478, 04 2009. [Online]. Available: https://doi.org/10.1186/BF03353164

[63] J. R. Barnes, R. M. Haberle, R. J. Wilson, S. R. Lewis, J. R. Murphy, and P. L. Read, *The Global Circulation*, ser. Cambridge Planetary Science. Cambridge University Press, 2017, p. 229–294. [Online]. Available: https://doi.org/10.1017/9781139060172.009

[64] C. B. Leovy, "The general circulation of mars: Models and observations," in *Issues in Atmospheric and Oceanic Modeling*, ser. Advances in Geophysics, B. Saltzman, Ed. Elsevier, 1985, vol. 28, pp. 327–346. [Online]. Available: https://doi.org/10.1016/S0065-2687(08)60229-0

[65] T. N. Titus, S. Byrne, A. Colaprete, F. Forget, T. I. Michaels, and T. H. Prettyman, *The CO2 Cycle*, ser. Cambridge Planetary Science. Cambridge University Press, 2017, p. 374–404. [Online]. Available: https://doi.org/10.1017/9781139060172.012

[66] M. G. Trainer, M. H. Wong, T. H. McConnochie, H. B. Franz, S. K. Atreya, P. G. Conrad, F. Lefevre, P. R. Mahaffy, C. A. Malespin, H. L. Manning, J. Martin-Torres, G. M. Martinez, C. P. McKay, R. Navarro-Gonzalez, A. Vicente-Retortillo, C. R. Webster, and M.-P. Zorzano, "Seasonal variations in atmospheric composition as measured in gale crater, mars," *Journal of Geophysical Research: Planets*, vol. 124, no. 11, pp. 3000–3024, 2019. [Online]. Available: https://agupubs.onlinelibrary.wiley.com/doi/abs/10.1029/2019JE006175

[67] N. Yoshida, H. Nakagawa, N. Terada, J. S. Evans, N. M. Schneider, S. K. Jain, T. Imamura, J.-Y. Chaufray, H. Fujiwara, J. Deighan, and B. M. Jakosky, "Seasonal and latitudinal variations of dayside n2/co2 ratio in the martian thermosphere derived from maven iuvs observations," *Journal of Geophysical Research: Planets*, vol. 125, no. 12, p. e2020JE006378, 2020. [Online]. Available: https://doi.org/10.1029/2020JE006378

[68] A. L. Sprague, W. V. Boynton, K. E. Kerry, D. M. Janes, D. M. Hunten, K. J. Kim, R. C. Reedy, and A. E. Metzger, "Mars' south polar ar enhancement: A tracer for south polar seasonal meridional mixing," *Science*, vol. 306, no. 5700, pp. 1364–1367, 2004.

[69] A. L. Sprague, W. V. Boynton, K. E. Kerry, D. M. Janes, N. J. Kelly, M. K. Crombie, S. M. Nelli, J. R. Murphy, R. C. Reedy, and A. E. Metzger, "Mars' atmospheric argon: Tracer for understanding martian atmospheric circulation and dynamics," *Journal of Geophysical Research: Planets*, vol. 112, no. E3, 2007.

[70] M. Richardson and R. Wilson, "A topographically forced asymmetry in the martian circulation and climate," *Nature*, vol. 416, pp. 298–301, 03 2002. [Online]. Available: https://doi.org/10.1038/416298a

[71] S. Cull, R. E. Arvidson, M. Mellon, S. Wiseman, R. Clark, T. Titus, R. V. Morris, and P. McGuire, "Seasonal h2o and co2 ice cycles at the mars phoenix landing site: 1. prelanding crism and hirise observations," *Journal of Geophysical Research: Planets*, vol. 115, no. E4, 2010. [Online]. Available: https://doi.org/10.1029/2009JE003340

[72] O. Aharonson, "Sublimation at the Base of a Seasonal CO2 Slab on Mars," in *Lunar and Planetary Science Conference*, ser. Lunar and Planetary Science Conference, S. Mackwell and E. Stansbery, Eds., Mar. 2004, p. 1918.

[73] H. H. Kieffer, "Cold jets in the martian polar caps," *Journal of Geophysical Research: Planets*, vol. 112, no. E8, 2007. [Online]. Available: https://doi.org/10.1029/2006JE002816

[74] R. M. Haberle, F. Forget, A. Colaprete, J. Schaeffer, W. V. Boynton, N. J. Kelly, and M. A. Chamberlain, "The effect of ground ice on the martian seasonal co2 cycle," *Planetary and Space Science*, vol. 56, no. 2, pp. 251–255, 2008, mars Polar Processes: Atmosphere-Surface Interactions. [Online]. Available: https://doi.org/10.1016/j.pss.2007.08.006

[75] M. A. Kahre, J. R. Murphy, C. E. Newman, R. J. Wilson, B. A. Cantor, M. T. Lemmon, and M. J. Wolff, *The Mars Dust Cycle*, ser. Cambridge Planetary Science. Cambridge University Press, 2017, p. 295–337. [Online]. Available: https://doi.org/10.1017/9781139060172.010

[76] M. Balme and R. Greeley, "Dust devils on earth and mars," *Reviews of Geophysics*, vol. 44, no. 3, 2006. [Online]. Available: https://doi.org/10.1029/2005RG000188

[77] B. Cantor, M. Malin, and K. S. Edgett, "Multiyear mars orbiter camera (moc) observations of repeated martian weather phenomena during the northern summer season," *Journal of Geophysical Research: Planets*, vol. 107, no. E3, pp. 3–1–3–8, 2002. [Online]. Available: https://doi.org/10.1029/2001JE001588

[78] R. T. Clancy, M. J. Wolff, and P. R. Christensen, "Mars aerosol studies with the mgs tes emission phase function observations: Optical depths, particle sizes, and ice cloud types versus latitude and solar longitude," *Journal of Geophysical Research: Planets*, vol. 108, no. E9, 2003. [Online]. Available: https://doi.org/10.1029/2003JE002058

[79] S. D. Fuerstenau, "Solar heating of suspended particles and the dynamics of martian dust devils," *Geophysical Research Letters*, vol. 33, no. 19, 2006.

[80] J. Pollack, M. Ockert-Bell, and M. Shepard, "Viking lander image analysis of martian atmospheric dust," *Journal of Geophysical Research*, vol. 100, 04 1995. [Online]. Available: 10.1029/94JE02640

[81] H. Chen-Chen, S. Pérez-Hoyos, and A. Sánchez-Lavega, "Dust particle size and optical depth on mars retrieved by the msl navigation cameras," *Icarus*, vol. 319, pp. 43–57, 2019. [Online]. Available: https://www.sciencedirect.com/science/article/pii/S001910351830201X

[82] J. Liu, M. I. Richardson, and R. J. Wilson, "An assessment of the global, seasonal, and interannual spacecraft record of martian climate in the thermal infrared," *Journal of Geophysical Research: Planets*, vol. 108, no. E8, 2003. [Online]. Available: https://doi.org/10.1029/2002JE001921

[83] P. J. Gierasch and R. M. Goody, "The effect of dust on the temperature of the martian atmosphere," *Journal of Atmospheric Sciences*, vol. 29, no. 2, pp. 400 – 402, 1972. [Online]. Available: https://journals.ametsoc.org/view/journals/atsc/29/2/1520-0469_1972_029_0400_teodot_2_0_co_2.xml

[84] M. A. Gurwell, E. A. Bergin, G. J. Melnick, and V. Tolls, "Mars surface and atmospheric temperature during the 2001 global dust storm," *Icarus*, vol. 175, no. 1, pp. 23–31, 2005. [Online]. Available: https://www.sciencedirect.com/science/article/pii/S0019103504003756

[85] E. Anderson and C. Leovy, "Mariner 9 television limb observations of dust and ice hazes on mars," *Journal of Atmospheric Sciences*, vol. 35, no. 4, pp. 723 – 734, 1978. [Online]. Available: https://doi.org/10.1175/1520-0469(1978)035<0723:MTLOOD>2.0.CO;2

[86] F. Jaquin, P. Gierasch, and R. Kahn, "The vertical structure of limb hazes in the martian atmosphere," *Icarus*, vol. 68, no. 3, pp. 442–461, 1986. [Online]. Available: https://www.sciencedirect.com/science/article/pii/0019103586900503

[87] M. D. Smith, "TES Limb-Geometry Observations of Aerosols," in *Sixth International Conference on Mars*, A. L. Albee and H. H. Kieffer, Eds., Jul. 2003, p. 3174.

[88] A. Kleinböhl, J. T. Schofield, D. M. Kass, W. A. Abdou, C. R. Backus, B. Sen, J. H. Shirley, W. G. Lawson, M. I. Richardson, F. W. Taylor, N. A. Teanby, and D. J. McCleese, "Mars climate sounder limb profile retrieval of atmospheric temperature, pressure, and dust and water ice opacity," *Journal of Geophysical Research: Planets*, vol. 114, no. E10, 2009. [Online]. Available: https://doi.org/10.1029/2009JE003358

[89] G. Liu, S. L. England, R. J. Lillis, P. Withers, P. R. Mahaffy, D. E. Rowland, M. Elrod, M. Benna, D. M. Kass, D. Janches, and B. Jakosky, "Thermospheric expansion associated with dust increase in the lower atmosphere on mars observed by maven/ngims," *Geophysical Research Letters*, vol. 45, no. 7, pp. 2901–2910, 2018. [Online]. Available: https://doi.org/10.1002/2018GL077525

[90] N. Venkateswara Rao, N. Gupta, and U. R. Kadhane, "Enhanced densities in the martian thermosphere associated with the 2018 planet-encircling dust event: Results from menca/mom and ngims/maven," *Journal of Geophysical Research: Planets*, vol. 125, no. 10, p. e2020JE006430, 2020. [Online]. Available: https://doi.org/10.1029/2020JE006430

[91] V. Leelavathi, N. Venkateswara Rao, and S. V. B. Rao, "Interannual variability of atmospheric gravity waves in the martian thermosphere: Effects of the 2018 planet-encircling dust event," *Journal of Geophysical Research: Planets*, vol. 125, no. 12, p. e2020JE006649, 2020. [Online]. Available: https://doi.org/10.1029/2020JE006649

[92] S. W. Stone, R. V. Yelle, M. Benna, D. Y. Lo, M. K. Elrod, and P. R. Mahaffy, "Hydrogen escape from mars is driven by seasonal and dust storm transport of water," *Science*, vol. 370, (6518), pp. 824–831, 2020. [Online]. Available: https://doi.org/10.1029/2006JE002816

[93] Y. Lee, X. Fang, M. Gacesa, Y. Ma, V. Tenishev, P. Mahaffy, C. Dong, M. Combi, S. Bougher, and B. Jakosky, "Effects of global and regional dust storms on the martian hot o corona and photochemical loss," *Journal of Geophysical Research: Space Physics*, vol. 125, no. 4, p. e2019JA027115, 2020. [Online]. Available: https://doi.org/10.1029/2019JA027115

[94] M. D. Smith, "Interannual variability in tes atmospheric observations of mars during 1999–2003," *Icarus*, vol. 167, no. 1, pp. 148–165, 2004, special Issue on DS1/Comet Borrelly.

[95] M. D. Smith, "Themis observations of mars aerosol optical depth from 2002–2008," *Icarus*, vol. 202, no. 2, pp. 444–452, 2009.

[96] L. Martin and R. Zurek, "An analysis of the history of dust activity on Mars," *Journal of Geophysical Research*, vol. 98, no. E2, pp. 3221–3246, Feb. 1993. [Online]. Available: https://doi.org/10.1029/92JE02937

[97] R. Zurek and L. Martin, "Interannual variability of planet-encircling dust storms on Mars," *Journal of Geophysical Research*, vol. 98, no. E2, pp. 3247–3259, Feb. 1993. [Online]. Available: https://doi.org/10.1029/92JE02936

[98] R. T. Clancy, B. J. Sandor, M. J. Wolff, P. R. Christensen, M. D. Smith, J. C. Pearl, B. J. Conrath, and R. J. Wilson, "An intercomparison of ground-based millimeter, mgs tes, and viking atmospheric temperature measurements: Seasonal and interannual variability of temperatures and dust loading in the global mars atmosphere," *Journal of Geophysical Research: Planets*, vol. 105, no. E4, pp. 9553–9571, 2000. [Online]. Available: https://doi.org/10.1029/1999JE001089

[99] B. A. Cantor, P. B. James, M. Caplinger, and M. J. Wolff, "Martian dust storms: 1999 mars orbiter camera observations," *Journal of Geophysical Research: Planets*, vol. 106, no. E10, pp. 23 653–23 687, 2001. [Online]. Available: https://doi.org/10.1029/2000JE001310

[100] L. Montabone., F. Forget., E. Millour., R. Wilson., S. Lewis., B. Cantor., D. Kass., A. Kleinbohl., M. Lemmon., M. Smith, and M. Wolff., "Eight year climatology of dust optical depth on mars," *Icarus*, vol. 251, pp. 65–95, 2015. [Online]. Available: https://doi.org/10.1016/j.icarus.2014.12.034

[101] H. Wang and M. I. Richardson, "The origin, evolution, and trajectory of large dust storms on mars during mars years 24–30 (1999–2011)," *Icarus*, vol. 251, pp. 112–127, 2015, dynamic Mars. [Online]. Available: https://doi.org/10.1016/j.icarus.2013.10.033

[102] M. Smith, "The annual cycle of water vapor on mars as observed by the thermal emission spectrometer," *J. Geophys. Res*, vol. 107, 11 2002.

[103] M. J. Strausberg, H. Wang, M. I. Richardson, S. P. Ewald, and A. D. Toigo, "Observations of the initiation and evolution of the 2001 mars global dust storm," *Journal of Geophysical Research: Planets*, vol. 110, no. E2, 2005.

[104] B. A. Cantor, K. M. Kanak, and K. S. Edgett, "Mars orbiter camera observations of martian dust devils and their tracks (september 1997 to january 2006) and evaluation of theoretical vortex models," *Journal of Geophysical Research: Planets*, vol. 111, no. E12, 2006.

[105] B. M. Jakosky, M. Slipski, M. Benna, P. Mahaffy, M. Elrod, R. Yelle, S. Stone, and N. Alsaeed, "Mars' atmospheric history derived from upper-atmosphere measurements of 38ar/36ar," *Science*, vol. 355, no. 6332, pp. 1408–1410, 2017. [Online]. Available: https://doi.org/10.1126/science.aai7721

[106] M. B. McElroy, T. Y. Kong, Y. L. Yung, and A. O. Nier, "Composition and structure of the martian upper atmosphere: Analysis of results from viking," *Science*, vol. 194, no. 4271, pp. 1295–1298, 1976. [Online]. Available: https://doi.org/10.1126/science.194.4271.1295

[107] A. O. Nier and M. B. McElroy, "Structure of the neutral upper atmosphere of mars: Results from viking 1 and viking 2," *Science*, vol. 194, no. 4271, pp. 1298–1300, 1976. [Online]. Available: https://doi.org/10.1126/science.194.4271.1298

[108] W. Mcclintock, N. Schneider, G. Holsclaw, J. Clarke, A. Hoskins, I. Stewart, F. Montmessin, R. Yelle, and J. Deighan, "The imaging ultraviolet spectrograph (iuvs) for the maven mission," *Space Science Reviews*, vol. 195, 09 2014. [Online]. Available: https://doi.org/10.1007/s11214-014-0098-7

[109] A. Bhardwaj, S. V. Thampi, T. P. Das, M. B. Dhanya, N. Naik, D. P. Vajja, P. Pradeepkumar, P. Sreelatha, G. Supriya, A. J. K., S. V. Mohankumar, R. S. Thampi, V. K. Yadav, B. Sundar, A. Nandi, G. P. Padmanabhan, and A. V. Aliyas, "On the evening time exosphere of mars: Result from menca aboard mars orbiter mission," *Geophysical Research Letters*, vol. 43, no. 5, pp. 1862–1867, 2016. [Online]. Available: https://doi.org/10.1002/2016GL067707

[110] A. Bhardwaj, S. V. Thampi, T. P. Das, M. B. Dhanya, N. Naik, D. P. Vajja, P. Pradeepkumar, P. Sreelatha, A. J. K., R. S. Thampi, V. K. Yadav, B. Sundar, A. Nandi, G. P. Padmanabhan, and A. V. Aliyas, "Observation of suprathermal argon in the exosphere of mars," *Geophysical Research Letters*, vol. 44, no. 5, pp. 2088–2095, 2017. [Online]. Available: https://doi.org/10.1002/2016GL072001

[111] C. Dong, S. W. Bougher, Y. Ma, Y. Lee, G. Toth, A. F. Nagy, X. Fang, J. Luhmann, M. W. Liemohn, J. S. Halekas, V. Tenishev, D. J. Pawlowski, and M. R. Combi,

"Solar wind interaction with the martian upper atmosphere: Roles of the cold thermosphere and hot oxygen corona," *Journal of Geophysical Research: Space Physics*, vol. 123, no. 8, pp. 6639–6654, 2018.

[112] J. R. Espley, W. M. Farrell, D. A. Brain, D. D. Morgan, B. Cantor, J. J. Plaut, M. H. Acuña, and G. Picardi, "Absorption of marsis radar signals: Solar energetic particles and the daytime ionosphere," *Geophysical Research Letters*, vol. 34, no. 9, 2007.

[113] S. A. Haider, M. A. Abdu, I. S. Batista, J. H. Sobral, E. Kallio, W. C. Maguire, and M. I. Verigin, "On the responses to solar x-ray flare and coronal mass ejection in the ionospheres of mars and earth," *Geophysical Research Letters*, vol. 36, no. 13, 2009.

[114] M. Mendillo, P. Withers, D. Hinson, H. Rishbeth, and B. Reinisch, "Effects of solar flares on the ionosphere of mars," *Science*, vol. 311, no. 5764, pp. 1135–1138, 2006.

[115] D. D. Morgan, D. A. Gurnett, D. L. Kirchner, R. L. Huff, D. A. Brain, W. V. Boynton, M. H. Acuña, J. J. Plaut, and G. Picardi, "Solar control of radar wave absorption by the martian ionosphere," *Geophysical Research Letters*, vol. 33, no. 13, 2006. [Online]. Available: https://doi.org/10.1029/2006GL026637

[116] F. Němec, D. D. Morgan, C. Diéval, D. A. Gurnett, and Y. Futaana, "Enhanced ionization of the martian nightside ionosphere during solar energetic particle events," *Geophysical Research Letters*, vol. 41, no. 3, pp. 793–798, 2014. [Online]. Available: https://doi.org/10.1002/2013GL058895

[117] V. Sheel, S. A. Haider, P. Withers, K. Kozarev, I. Jun, S. Kang, G. Gronoff, and C. Simon Wedlund, "Numerical simulation of the effects of a solar energetic particle event on the ionosphere of mars," *Journal of Geophysical Research: Space Physics*, vol. 117, no. A5, 2012.

[118] D. Ulusen, D. A. Brain, J. G. Luhmann, and D. L. Mitchell, "Investigation of mars' ionospheric response to solar energetic particle events," *Journal of Geophysical Research: Space Physics*, vol. 117, no. A12, 2012. [Online]. Available: https://doi.org/10.1029/2012JA017671

[119] S. L. England, G. Liu, E. Yiğit, P. R. Mahaffy, M. Elrod, M. Benna, H. Nakagawa, N. Terada, and B. Jakosky, "Maven ngims observations of atmospheric gravity waves in the martian thermosphere," *Journal of Geophysical Research: Space Physics*, vol. 122, no. 2, pp. 2310–2335, 2017.

[120] N. Terada, F. Leblanc, H. Nakagawa, A. S. Medvedev, E. Yiğit, T. Kuroda, T. Hara, S. L. England, H. Fujiwara, K. Terada, K. Seki, P. R. Mahaffy, M. Elrod, M. Benna, J. Grebowsky, and B. M. Jakosky, "Global distribution and parameter dependences of gravity wave activity in the martian upper thermosphere derived from maven/ngims observations," *Journal of Geophysical Research: Space Physics*, vol. 122, no. 2, pp. 2374–2397, 2017.

[121] C. Lee, W. G. Lawson, M. I. Richardson, N. G. Heavens, A. Kleinböhl, D. Banfield, D. J. McCleese, R. Zurek, D. Kass, J. T. Schofield, C. B. Leovy, F. W. Taylor, and A. D. Toigo, "Thermal tides in the martian middle atmosphere as seen by the mars climate sounder," *Journal of Geophysical Research: Planets*, vol. 114, no. E3, 2009. [Online]. Available: https://doi.org/10.1029/2008JE003285

[122] G. Liu, S. England, R. J. Lillis, P. R. Mahaffy, M. Elrod, M. Benna, and B. Jakosky, "Longitudinal structures in mars' upper atmosphere as observed by maven/ngims," *Journal of Geophysical Research: Space Physics*, vol. 122, no. 1, pp. 1258–1268, 2017. [Online]. Available: https://doi.org/10.1002/2016JA023455

[123] Y. Moudden and J. M. Forbes, "Topographic connections with density waves in mars' aerobraking regime," *Journal of Geophysical Research: Planets*, vol. 113, no. E11, 2008. [Online]. Available: https://doi.org/10.1029/2008JE003107

[124] Y. Moudden and J. M. Forbes, "A new interpretation of mars aerobraking variability: Planetary wave-tide interactions," *Journal of Geophysical Research: Planets*, vol. 115, no. E9, 2010. [Online]. Available: https://doi.org/10.1029/2009JE003542

[125] S. W. Stone, R. V. Yelle, M. Benna, M. K. Elrod, and P. R. Mahaffy, "Thermal structure of the martian upper atmosphere from maven ngims," *Journal of Geophysical Research: Planets*, vol. 123, no. 11, pp. 2842–2867, 2018. [Online]. Available: https://doi.org/10.1029/2018JE005559

[126] J. M. Bell, S. W. Bougher, and J. R. Murphy, "Vertical dust mixing and the interannual variations in the mars thermosphere," *Journal of Geophysical Research: Planets*, vol. 112, no. E12, 2007.

[127] J. F. Qin, H. Zou, Y. G. Ye, Z. F. Yin, J. S. Wang, and E. Nielsen, "Effects of local dust storms on the upper atmosphere of mars: Observations and simulations," *Journal of Geophysical Research: Planets*, vol. 124, no. 2, pp. 602–616, 2019. [Online]. Available: https://doi.org/10.1029/2018JE005864

[128] P. Withers and R. Pratt, "An observational study of the response of the upper atmosphere of mars to lower atmospheric dust storms," *Icarus*, vol. 225, no. 1, pp. 378–389, 2013. [Online]. Available: https://doi.org/10.1016/j.icarus.2013.02.032

[129] M. Pilinski, S. Bougher, K. Greer, E. Thiemann, L. Andersson, M. Benna, and M. Elrod, "First evidence of persistent nighttime temperature structures in the neutral thermosphere of mars," *Geophysical Research Letters*, vol. 45, no. 17, pp. 8819–8825, 2018. [Online]. Available: https://doi.org/10.1029/2018GL078761

[130] S. W. Bougher, R. G. Roble, E. C. Ridley, and R. E. Dickinson, "The mars thermosphere: 2. general circulation with coupled dynamics and composition," *Journal of Geophysical Research: Solid Earth*, vol. 95, no. B9, pp. 14 811–14 827, 1990. [Online]. Available: https://doi.org/10.1029/JB095iB09p14811

[131] M. K. Elrod, S. Bougher, J. Bell, P. R. Mahaffy, M. Benna, S. Stone, R. Yelle, and B. Jakosky, "He bulge revealed: He and co2 diurnal and seasonal variations in the upper atmosphere of mars as detected by maven ngims," *Journal of Geophysical Research: Space Physics*, vol. 122, no. 2, pp. 2564–2573, 2017. [Online]. Available: https://doi.org/10.1002/2016JA023482

[132] W. T. Kasprzak, "Evidence for a helium flux in the lower thermosphere," *Journal of Geophysical Research (1896-1977)*, vol. 74, no. 3, pp. 894–896, 1969.

[133] G. Keating and E. Prior, "The winter helium bulge. space research," *Space Research*, 1968.

[134] X. Liu, W. Wang, J. P. Thayer, A. Burns, E. Sutton, S. C. Solomon, L. Qian, and G. Lucas, "The winter helium bulge revisited," *Geophysical Research Letters*, vol. 41, no. 19, pp. 6603–6609, 2014. [Online]. Available: https://doi.org/10.1002/2014GL061471

[135] K. Mauersberger, W. E. Potter, and D. C. Kayser, "A direct measurement of the winter helium bulge," *Geophysical Research Letters*, vol. 3, no. 5, pp. 269–271, 1976. [Online]. Available: https://doi.org/10.1029/GL003i005p00269

[136] J. E. Cooley, D. N. Harpold, and C. A. Reber, "Upper atmosphere neutral atomic h and he composition, measuring number density variations with height and latitude from explorer 32 satellite," *Space Research*, vol. 8, no. 993, 01 1968.

[137] J. P. Thayer, X. Liu, J. Lei, M. Pilinski, and A. G. Burns, "The impact of helium on thermosphere mass density response to geomagnetic activity during the recent solar minimum," *Journal of Geophysical Research: Space Physics*, vol. 117, no. A7, 2012.

[138] W. T. Kasprzak, H. B. Niemann, A. E. Hedin, S. W. Bougher, and D. M. Hunten, "Neutral composition measurements by the pioneer venus neutral mass spectrometer during orbiter re-entry," *Geophysical Research Letters*, vol. 20, no. 23, pp. 2747–2750, 1993. [Online]. Available: https://doi.org/10.1029/93GL02241

[139] V. A. Krasnopolsky and G. R. Gladstone, "Helium on mars and venus: Euve observations and modeling," *Icarus*, vol. 176, no. 2, pp. 395–407, 2005. [Online]. Available: https://doi.org/10.1016/j.icarus.2005.02.005

[140] H. B. Niemann, W. T. Kasprzak, A. E. Hedin, D. M. Hunten, and N. W. Spencer, "Mass spectrometric measurements of the neutral gas composition of the thermosphere and exosphere of venus," *Journal of Geophysical Research: Space Physics*, vol. 85, no. A13, pp. 7817–7827, 1980. [Online]. Available: https://doi.org/10.1029/JA085iA13p07817

[141] M. Slipski, B. M. Jakosky, M. Benna, M. Elrod, P. Mahaffy, D. Kass, S. Stone, and R. Yelle, "Variability of martian turbopause altitudes," *Journal of Geophysical Research: Planets*, vol. 123, no. 11, pp. 2939–2957, 2018.

[142] E. Chassefière and F. Leblanc, "Mars atmospheric escape and evolution; interaction with the solar wind," *Planetary and Space Science*, vol. 52, no. 11, pp. 1039–1058, 2004, planet Mars. Sponsors: Centre National d'Etudes Spatiales (CNES); Centre National de la Recherche Scientifique (CNRS); Observatoire de Paris. [Online]. Available: https://www.sciencedirect.com/science/article/pii/S0032063304000893

[143] B. M. Jakosky, R. O. Pepin, R. E. Johnson, and J. Fox, "Mars atmospheric loss and isotopic fractionation by solar-wind-induced sputtering and photochemical escape," *Icarus*, vol. 111, no. 2, pp. 271–288, 1994.

[144] L. H. and B. S. J. Space Sciences Series of ISSI, pp. 265–276. [Online]. Available: https://doi.org/10.1029/GM066p0265

[145] M. Slipski and B. M. Jakosky, "Argon isotopes as tracers for martian atmospheric loss," *icarus*, vol. 272, pp. 212–227, Jul. 2016.

[146] J.-Y. Chaufray, F. Gonzalez-Galindo, F. Forget, M. Lopez-Valverde, F. Leblanc, R. Modolo, and S. Hess, "Variability of the hydrogen in the martian upper atmosphere as simulated by a 3d atmosphere–exosphere coupling," *Icarus*, vol. 245, pp. 282–294, 2015.

[147] F. Forget, F. Montmessin, J.-L. Bertaux, F. González-Galindo, S. Lebonnois, E. Quémerais, A. Reberac, E. Dimarellis, and M. A. López-Valverde, "Density and temperatures of the upper martian atmosphere measured by stellar occultations with mars express spicam," *Journal of Geophysical Research: Planets*, vol. 114, no. E1, 2009.

[148] F. Montmessin, O. Korablev, F. Lefèvre, J.-L. Bertaux, A. Fedorova, A. Trokhimovskiy, J. Chaufray, G. Lacombe, A. Reberac, L. Maltagliati, Y. Willame, S. Guslyakova, J.-C. Gérard, A. Stiepen, D. Fussen, N. Mateshvili, A. Määttänen, F. Forget, O. Witasse, F. Leblanc, A. Vandaele, E. Marcq, B. Sandel, B. Gondet, N. Schneider, M. Chaffin, and N. Chapron, "Spicam on mars express: A 10 year in-depth survey of the martian atmosphere," *Icarus*, vol. 297, pp. 195–216, 2017. [Online]. Available: https://doi.org/10.1016/j.icarus.2017.06.022

[149] H. Gröller, R. V. Yelle, T. T. Koskinen, F. Montmessin, G. Lacombe, N. M. Schneider, J. Deighan, A. I. F. Stewart, S. K. Jain, M. S. Chaffin, M. M. J. Crismani, A. Stiepen, F. Lefèvre, W. E. McClintock, J. T. Clarke, G. M. Holsclaw, P. R. Mahaffy, S. W. Bougher, and B. M. Jakosky, "Probing the martian atmosphere with maven/iuvs stellar occultations," *Geophysical Research Letters*, vol. 42, no. 21, pp. 9064–9070, 2015.

[150] H. Gröller, F. Montmessin, R. V. Yelle, F. Lefèvre, F. Forget, N. M. Schneider, T. T. Koskinen, J. Deighan, and S. K. Jain, "Maven/iuvs stellar occultation measurements of mars atmospheric structure and composition," *Journal of Geophysical Research: Planets*, vol. 123, no. 6, pp. 1449–1483, 2018.

[151] V. Krasnopolsky, O. Likin, F. Farnik, and B. Valnicek, "Solar occultation observations of the martian atmosphere in the ranges of 2–4 and 4–8 kev measured by phobos 2," *Icarus*, vol. 89, no. 1, pp. 147–151, 1991. [Online]. Available: https://doi.org/10.1016/0019-1035(91)90094-A

[152] D. E. Anderson Jr., "Mariner 6, 7, and 9 ultraviolet spectrometer experiment: Analysis of hydrogen lyman alpha data," *Journal of Geophysical Research*

(1896-1977), vol. 79, no. 10, pp. 1513–1518, 1974. [Online]. Available: https://doi.org/10.1029/JA079i010p01513

[153] V. Krasnopolsky, "On the structure of mars' atmosphere at 120–220 km," *Icarus*, vol. 24, no. 1, pp. 28–35, 1975. [Online]. Available: https://www.sciencedirect.com/science/article/pii/0019103575901554

[154] S. J. Bauer and M. H. Hantsch, "Solar cycle variation of the upper atmosphere temperature of mars," *Geophysical Research Letters*, vol. 16, no. 5, pp. 373–376, 1989.

[155] G. Fjeldbo, A. , and B. Seidel, "The mariner 1969 occultation measurements of the upper atmosphere of mars," *Radio Science*, vol. 5, no. 2, pp. 381–386, 1970.

[156] A. Kliore., *Radio Occultation Observations of the Ionospheres of Mars and Venus*. American Geophysical Union (AGU), pp. 265–276.

[157] A. J. Kliore., G. Fjeldbo., B. L. Seidel., M. J. Sykes., and P. M. Woiceshyn., "S band radio occultation measurements of the atmosphere and topography of mars with mariner 9: Extended mission coverage of polar and intermediate latitudes," *Journal of Geophysical Research (1896-1977)*, vol. 78, no. 20, pp. 4331–4351, 1973. [Online]. Available: https://doi.org/10.1029/JB078i020p04331

[158] G. F. Lindal, H. B. Hotz, D. N. Sweetnam, Z. Shippony, J. P. Brenkle, G. V. Hartsell, R. T. Spear, and W. H. Michael Jr., "Viking radio occultation measurements of the atmosphere and topography of mars: Data acquired during 1 martian year of tracking," *Journal of Geophysical Research: Solid Earth*, vol. 84, no. B14, pp. 8443–8456, 1979. [Online]. Available: https://doi.org/10.1029/JB084iB14p08443

[159] M. Mendillo, C. Narvaez, G. Lawler, W. Kofman, J. Mouginot, D. Morgan, and D. Gurnett, "The equivalent slab thickness of mars' ionosphere: Implications for thermospheric temperature," *Geophysical Research Letters*, vol. 42, no. 9, pp. 3560–3568, 2015. [Online]. Available: https://doi.org/10.1002/2015GL063096

[160] A. Seiff, "The Viking atmosphere structure experiment - techniques, instruments, and expected accuracies." *Space Science Instrumentation*, vol. 2, pp. 381–423, Sep. 1976.

[161] A. Seiff and D. B. Kirk, "Structure of mars' atmosphere up to 100 kilometers from the entry measurements of viking 2," *Science*, vol. 194, no. 4271, pp. 1300–1303,

1976. [Online]. Available: https://www.science.org/doi/abs/10.1126/science.194.4271.1300

[162] A. Seiff and D. B. Kirk, "Structure of the atmosphere of mars in summer at mid-latitudes," *Journal of Geophysical Research (1896-1977)*, vol. 82, no. 28, pp. 4364–4378, 1977. [Online]. Available: https://agupubs.onlinelibrary.wiley.com/doi/abs/10.1029/JS082i028p04364

[163] P. Withers, M. Towner, B. Hathi, and J. Zarnecki, "Analysis of entry accelerometer data: A case study of mars pathfinder," *Planetary and Space Science*, vol. 51, no. 9, pp. 541–561, 2003. [Online]. Available: https://doi.org/10.1016/S0032-0633(03)00077-1

[164] P. Withers, S. Bougher, and G. Keating, "The effects of topographically-controlled thermal tides in the martian upper atmosphere as seen by the mgs accelerometer," *Icarus*, vol. 164, no. 1, pp. 14–32, 2003. [Online]. Available: https://doi.org/10.1016/S0019-1035(03)00135-0

[165] J. A. Magalhaes, J. T. Schofield, and A. Seiff, "Results of the mars pathfinder atmospheric structure investigation," *Journal of Geophysical Research: Planets*, vol. 104, no. E4, pp. 8943–8955, 1999. [Online]. Available: https://doi.org/10.1029/1998JE900041

[166] J. T. Schofield, J. R. Barnes, D. Crisp, R. M. Haberle, S. Larsen, J. A. Magalhães, J. R. Murphy, A. Seiff, and G. Wilson, "The mars pathfinder atmospheric structure investigation/meteorology (asi/met) experiment," *Science*, vol. 278, no. 5344, pp. 1752–1758, 1997.

[167] A. Seiff, J. Tillman, J. Murphy, J. Schofield, D. Crisp, J. Barnes, C. LaBaw, C. Mahoney, J. Mihalov, G. Wilson, and R. Haberle, "The atmosphere structure and meteorology instrument on the mars pathfinder lander," *Journal of Geophysical Research*, vol. 102, 02 1997.

[168] S. Bougher, G. Keating, R. Zurek, J. Murphy, R. Haberle, J. Hollingsworth, and R. Clancy, "Mars global surveyor aerobraking: Atmospheric trends and model interpretation," *Advances in Space Research*, vol. 23, no. 11, pp. 1887–1897, 1999, the Moon and Mars.

[169] P. Withers, "Mars global surveyor and mars odyssey accelerometer observations of the martian upper atmosphere during aerobraking," *Geophysical Research Letters*, vol. 33, no. 2, 2006. [Online]. Available: https://doi.org/10.1029/2005GL024447

[170] R. H. Tolson, A. M. Dwyer, J. L. Hanna, G. M. Keating, B. E. George, P. E. Escalera, and M. R. Werner, "Application of accelerometer data to mars odyssey aerobraking and atmospheric modeling," *Journal of Spacecraft and Rockets*, vol. 42, no. 3, pp. 435–443, 2005. [Online]. Available: https://doi.org/10.2514/1.15173

[171] R. Tolson, E. Bemis, S. Hough, K. Zaleski, G. Keating, J. Shidner, S. Brown, A. Brickler, M. Scher, and P. Thomas, "Atmospheric modeling using accelerometer data during mars reconnaissance orbiter aerobraking operations," *Journal of Spacecraft and Rockets*, vol. 45, no. 3, pp. 511–518, 2008. [Online]. Available: https://doi.org/10.2514/1.34301

[172] R. H. Tolson, G. M. Keating, G. J. Cancro, J. S. Parker, S. N. Noll, and B. L. Wilkerson, "Application of accelerometer data to mars global surveyor aerobraking operations," *Journal of Spacecraft and Rockets*, vol. 36, no. 3, pp. 323–329, 1999. [Online]. Available: https://doi.org/10.2514/2.3474

[173] R. Tolson, G. Keating, S. Noll, D. Baird, and T. Shellenberg, "Utilization of mars global surveyor accelerometer data for atmospheric modeling," *Advances in Astronautical Science*, vol. 103, 01 2000.

[174] R. C. Blanchard and P. N. Desai, "Mars phoenix entry, descent, and landing trajestory and atmosphere reconstruction," *Journal of Spacecraft and Rockets*, vol. 48, no. 5, pp. 809–822, 2011.

[175] P. Withers and D. C. Catling, "Observations of atmospheric tides on mars at the season and latitude of the phoenix atmospheric entry," *Geophysical Research Letters*, vol. 37, no. 24, 2010. [Online]. Available: https://doi.org/10.1029/2010GL045382

[176] P. Withers and M. D. Smith, "Atmospheric entry profiles from the mars exploration rovers spirit and opportunity," *Icarus*, vol. 185, no. 1, pp. 133–142, 2006. [Online]. Available: https://doi.org/10.1016/j.icarus.2006.06.013

[177] L. Montabone, S. R. Lewis, P. L. Read, and P. Withers, "Reconstructing the weather on mars at the time of the mers and beagle 2 landings,"

Geophysical Research Letters, vol. 33, no. 19, 2006. [Online]. Available: https://doi.org/10.1029/2006GL026565

[178] A. Chen, A. Cianciolo, A. R. Vasavada, C. Karlgaard, J. Barnes, B. Cantor, D. Kass, S. Rafkin, and D. Tyler, "Reconstruction of atmospheric properties from mars science laboratory entry, descent, and landing," *Journal of Spacecraft and Rockets*, vol. 51, no. 4, pp. 1062–1075, 2014.

[179] C. Holstein-Rathlou, A. Maue, and P. Withers, "Atmospheric studies from the mars science laboratory entry, descent and landing atmospheric structure reconstruction," *Planetary and Space Science*, vol. 120, pp. 15–23, 2016. [Online]. Available: https://doi.org/10.1016/j.pss.2015.10.015

[180] A. O. Nier and M. B. McElroy, "Composition and structure of mars' upper atmosphere: Results from the neutral mass spectrometers on viking 1 and 2," *Journal of Geophysical Research (1896-1977)*, vol. 82, no. 28, pp. 4341–4349, 1977. [Online]. Available: https://doi.org/10.1029/JS082i028p04341

[181] A. Kumar and P. Chauhan, "Scientific exploration of mars by first indian interplanetary space probe: Mars orbiter mission," vol. 107, pp. 1096–1097, 01 2014.

[182] D. L. Mitchell, C. Mazelle, J.-A. Sauvaud, J.-J. Thocaven, J. Rouzaud, A. Fedorov, P. Rouger, D. Toublanc, E. Taylor, D. Gordon, M. Robinson, S. Heavner, P. Turin, M. Diaz-Aguado, D. W. Curtis, R. P. Lin, and B. M. Jakosky, "The maven solar wind electron analyzer," *Space Science Reviews*, vol. 200, no. 1, pp. 495–528, Apr 2016. [Online]. Available: https://doi.org/10.1007/s11214-015-0232-1

[183] J. Halekas., E. Taylor., G. Dalton., G. Johnson., D. Curtis., D. McFadden., J.P.and Mitchell., and B. Lin., R.P.and Jakosky., "The solar wind ion analyzer for maven," *Space Science Reviews*, vol. 195, no. 1, pp. 125–151, Dec 2015.

[184] D. Larson., R. Lillis., C. Lee., K. Dunn., P.A.and Hatch., M. Robinson., D. Glaser., J. Chen., D. Curtis., C. Tiu., R. Lin., J. Luhmann., and B. Jakosky., "The maven solar energetic particle investigation," *Space Science Reviews*, vol. 195, no. 1, pp. 153–172, Dec 2015. [Online]. Available: https://doi.org/10.1007/s11214-015-0218-z

[185] J. P. McFadden, O. Kortmann, D. Curtis, G. Dalton, G. Johnson, R. Abiad, R. Sterling, K. Hatch, P. Berg, C. Tiu, D. Gordon, S. Heavner, M. Robinson, M. Marckwordt, R. Lin, and B. Jakosky, "Maven suprathermal and thermal ion

compostion (static) instrument," *Space Science Reviews*, vol. 195, no. 1, pp. 199–256, Dec 2015. [Online]. Available: https://doi.org/10.1007/s11214-015-0175-6

[186] L. Andersson, R. E. Ergun, G. T. Delory, A. Eriksson, J. Westfall, H. Reed, J. McCauly, D. Summers, and D. Meyers, "The langmuir probe and waves (lpw) instrument for maven," *Space Science Reviews*, vol. 195, no. 173, 2015.

[187] F. G. Eparvier, P. C. Chamberlin, T. N. Woods, and E. M. B. Thiemann, "The solar extreme ultraviolet monitor for maven," *Space Science Reviews*, vol. 195, no. 293, 2015.

[188] J. Connerney, J. Espley, P. Lawton, and et al, "The maven magnetic field investigation," *Space Science Review*, vol. 195, p. 257–291, 2015.

[189] P. Withers, M. Felici, M. Mendillo, L. Moore, C. Narvaez, M. F. Vogt, K. Oudrhiri, D. Kahan, and B. M. Jakosky, "The maven radio occultation science experiment (rose)," *Geophysical Research Letters*, vol. 216, no. 61, 2020. [Online]. Available: 10.1007/s11214-020-00687-6

[190] F. Leblanc, M. Benna, J. Y. Chaufray, A. Martinez, R. Lillis, S. Curry, M. K. Elrod, P. Mahaffy, R. Modolo, J. G. Luhmann, and B. Jakosky, "First in situ evidence of mars nonthermal exosphere," *Geophysical Research Letters*, vol. 46, no. 8, pp. 4144–4150, 2019. [Online]. Available: https://doi.org/10.1029/2019GL082192

[191] V. S. Raja, M. V. H. Rao, K. Kalyani, K. Bhaskar, A. Chandran, M. Mahajan, A. Manja, G. Gouda, T. Jalluri D P V, P. Amudha, M. Kandpal, K. Pramod, S. Viswanath, P. L V, A. Laxmiprasad, P. Chakraborty, J. Kamalakar, N. G. Dr, and M. Viswanathan, "Lyman alpha photometer: A far-ultraviolet sensor for the study of hydrogen isotope ratio in the martian exosphere," *Current science*, vol. 109, pp. 1114–1120, 10 2015.

[192] K. Mathew, S. Sarkar, A. Srinivas, M. Dutta, M. Rohit, H. Seth, R. Kumaran, K. Pandya, A. Kumar, J. Sharma, J. Desai, A. Patel, V. Patel, P. Shukla, M. M. Subbiah, A. Singh, A. Gupta, J. Rathi, P. Babu, and k. k. Seelin, "Methane sensor for mars," *Current Science*, vol. 109, 09 2015. [Online]. Available: https://doi.org/10.18520/v109/i6/1087-1096

[193] A. Bhardwaj, S. Mohankumar, T. Das, P. Padannayil, S. Pradeep, B. Sundar, A. Nandi, D. Vajja, M. Dhanya, N. Naik, G. Supriya, R. Thampi, G. Padmanabhan,

V. Yadav, and A. Aliyas, "Menca experiment aboard india's mars orbiter mission," *Current science*, vol. 109, p. 1106, 09 2015.

[194] R. Singh, S. Sarkar, M. Kumar, A. Saxena, U. Rao, A. Bhardwaj, J. Desai, J. Sharma, A. Patel, Y. Shinde, H. Arora, A. Srinivas, J. Rathi, H. Patel, M. Sarkar, A. Gajaria, M. M. Subbiah, M. Pandya, A. Gujrati, and k. k. Seelin, "Thermal infrared imaging spectrometer for mars orbiter mission," *Current science*, vol. 109, pp. 25–2015, 09 2015.

[195] A. Arya, S. Sarkar, A. Srinivas, M. M. Subbiah, V. Patel, R. Bhatnagar Singh, P. R. Rudravaram, S. Roy, I. Misra, S. Paul, D. Shah, K. Patel, R. Gambhir, U. Rao, A. Patel, J. Desai, R. Dev, A. Prashar, H. Rambhia, and k. k. Seelin, "Mars colour camera: The payload characterization/calibration and data analysis from earth imaging phase," *Current science*, vol. 109, pp. 1076–1086, 09 2015. [Online]. Available: https://doi.org/10.18520/cs/v109/i6/1076-1086

[196] M. Benna. and M. Elrod., "Ngims pds software interface specification maven-ngims-sis-0001, pds atmospheres node," 2019. [Online]. Available: http://atmos.pds.nasa.gov/data_and_services/atmospheresdata/MAVEN/ngims.html

[197] M. Benna, S. Bougher, Y. Lee, K. Roeten, E. Yiğit, P. Mahaffy, and B. Jakosky, "Global circulation of mars' upper atmosphere," *Science (New York, N.Y.)*, vol. 366, pp. 1363–1366, 12 2019.

[198] N. Gupta, N. V. Rao, S. Bougher, and M. K. Elrod, "Latitudinal and seasonal asymmetries of the helium bulge in the martian upper atmosphere," *Journal of Geophysical Research: Planets*, vol. 126, no. 10, p. e2021JE006976, 2021.

[199] N. R. Lewkow and V. Kharchenko, "PRECIPITATION OF ENERGETIC NEUTRAL ATOMS AND INDUCED NON-THERMAL ESCAPE FLUXES FROM THE MARTIAN ATMOSPHERE," *The Astrophysical Journal*, vol. 790, no. 2, p. 98, jul 2014. [Online]. Available: https://doi.org/10.1088/0004-637x/790/2/98

[200] V. Krasnopolsky and F. Lefèvre, *Chemistry of the Atmospheres of Mars, Venus, and Titan*, 01 2013. [Online]. Available: 10.2458/azu_uapress_9780816530595-ch11

[201] A. Morse, K. Altwegg, D. Andrews, H. Auster, C. Carr, M. Galand, F. Goesmann, S. Gulkis, S. Lee, I. Richter, S. Sheridan, S. Stern, M. A'Hearn, P. Feldman,

J. Parker, K. Retherford, H. Weaver, and I. Wright, "The rosetta campaign to detect an exosphere at lutetia," *Planetary and Space Science*, vol. 66, no. 1, pp. 165–172, 2012, rosetta Fly-by at Asteroid (21) Lutetia. [Online]. Available: https://www.sciencedirect.com/science/article/pii/S0032063312000207

[202] R. M. Haberle, M. M. Joshi, J. R. Murphy, J. R. Barnes, J. T. Schofield, G. Wilson, M. Lopez-Valverde, J. L. Hollingsworth, A. F. C. Bridger, and J. Schaeffer, "General circulation model simulations of the mars pathfinder atmospheric structure investigation/meteorology data," *Journal of Geophysical Research: Planets*, vol. 104, no. E4, pp. 8957–8974, 1999. [Online]. Available: https://doi.org/10.1029/1998JE900040

[203] F. González-Galindo, J.-Y. Chaufray, M. A. López-Valverde, G. Gilli, F. Forget, F. Leblanc, R. Modolo, S. Hess, and M. Yagi, "Three-dimensional martian ionosphere model: I. the photochemical ionosphere below 180 km," *Journal of Geophysical Research: Planets*, vol. 118, no. 10, pp. 2105–2123, 2013. [Online]. Available: https://doi.org/10.1002/jgre.20150

[204] E. M. B. Thiemann, P. C. Chamberlin, F. G. Eparvier, B. Templeman, T. N. Woods, S. W. Bougher, and B. M. Jakosky, "The maven euvm model of solar spectral irradiance variability at mars: Algorithms and results," *Journal of Geophysical Research: Space Physics*, vol. 122, no. 3, pp. 2748–2767, 2017.

[205] S. W. Bougher, K. J. Roeten, K. Olsen, P. R. Mahaffy, M. Benna, M. Elrod, S. K. Jain, N. M. Schneider, J. Deighan, E. Thiemann, F. G. Eparvier, A. Stiepen, and B. M. Jakosky, "The structure and variability of mars dayside thermosphere from maven ngims and iuvs measurements: Seasonal and solar activity trends in scale heights and temperatures," *Journal of Geophysical Research: Space Physics*, vol. 122, no. 1, pp. 1296–1313, 2017. [Online]. Available: https://doi.org/10.1002/2016JA023454

[206] R. W. Zurek, R. A. Tolson, S. W. Bougher, R. A. Lugo, D. T. Baird, J. M. Bell, and B. M. Jakosky, "Mars thermosphere as seen in maven accelerometer data," *Journal of Geophysical Research: Space Physics*, vol. 122, no. 3, pp. 3798–3814, 2017. [Online]. Available: https://doi.org/10.1002/2016JA023641

[207] B. Stephen., "Mars thermospheric helium distributions: M-gitm simulated datasets for comparison to maven/ngims measurements," *University of Michigan*, 2021. [Online]. Available: https://doi.org/10.7302/36zc-y350

[208] X. Fang, Y. Ma, Y. Lee, S. Bougher, G. Liu, M. Benna, P. Mahaffy, L. Montabone, D. Pawlowski, C. Dong, Y. Dong, and B. Jakosky, "Mars dust storm effects in the ionosphere and magnetosphere and implications for atmospheric carbon loss," *Journal of Geophysical Research: Space Physics*, vol. 125, no. 3, 2020.

[209] F. González-Galindo, S. Bougher, M. López-Valverde, F. Forget, and J. Murphy, "Thermal and wind structure of the martian thermosphere as given by two general circulation models," *Planetary and Space Science*, vol. 58, no. 14, pp. 1832–1849, 2010. [Online]. Available: https://doi.org/10.1016/j.pss.2010.08.013

[210] M. J. Alexander, A. I. F. Stewart, S. C. Solomon, and S. W. Boucher, "Local time asymmetries in the venus thermosphere," *Journal of Geophysical Research: Planets*, vol. 98, no. E6, pp. 10 849–10 871, 1993.

[211] S. W. Bougher and W. J. Borucki, "Venus o2 visible and ir nightglow: Implications for lower thermosphere dynamics and chemistry," *Journal of Geophysical Research: Planets*, vol. 99, no. E2, pp. 3759–3776, 1994. [Online]. Available: https://doi.org/10.1029/93JE03431

[212] J. L. Fox and W. T. Kasprzak, "Near-terminator venus ionosphere: Evidence for a dawn/dusk asymmetry in the thermosphere," *Journal of Geophysical Research: Planets*, vol. 112, no. E9, 2007. [Online]. Available: https://agupubs.onlinelibrary.wiley.com/doi/abs/10.1029/2007JE002899

[213] S. Zhang, S. Bougher, and M. Alexander, "The impact of gravity waves on the Venus thermosphere and O2 IR nightglow," *Journal of Geophysical Research*, vol. 101, no. E10, pp. 23 195–23 206, 1996. [Online]. Available: https://doi.org/10.1029/96JE02035

[214] J. M. Forbes, S. Bruinsma, and F. G. Lemoine, "Solar rotation effects on the thermospheres of mars and earth," *Science*, vol. 312, no. 5778, pp. 1366–1368, 2006.

[215] M. P. Hickey, R. L. Walterscheid, and G. Schubert, "Gravity wave heating and cooling of the thermosphere: Sensible heat flux and viscous flux of kinetic energy,"

Journal of Geophysical Research: Space Physics, vol. 116, no. A12, 2011. [Online]. Available: https://doi.org/10.1029/2011JA016792

[216] H. F. Parish, G. Schubert, M. P. Hickey, and R. L. Walterscheid, "Propagation of tropospheric gravity waves into the upper atmosphere of mars," *Icarus*, vol. 203, no. 1, pp. 28–37, 2009. [Online]. Available: https://doi.org/10.1016/j.icarus.2009.04.031

[217] H. Liu, H. Lühr, and S. Watanabe, "A solar terminator wave in thermospheric wind and density simultaneously observed by champ," *Geophysical Research Letters*, vol. 36, no. 10, 2009. [Online]. Available: https://doi.org/10.1029/2009GL038165

[218] A. Kleinböhl, A. Spiga, D. M. Kass, J. H. Shirley, E. Millour, L. Montabone, and F. Forget, "Diurnal variations of dust during the 2018 global dust storm observed by the mars climate sounder," *Journal of Geophysical Research: Planets*, vol. 125, no. 1, p. e2019JE006115, 2020. [Online]. Available: https://doi.org/10.1029/2019JE006115

[219] A. Sanchez-Lavega, T. del Río-Gaztelurrutia, J. Hernández-Bernal, and M. Delcroix, "The onset and growth of the 2018 martian global dust storm," *Geophysical Research Letters*, vol. 46, no. 11, pp. 6101–6108, 2019. [Online]. Available: https://agupubs.onlinelibrary.wiley.com/doi/abs/10.1029/2019GL083207

[220] M. D. Smith, "Themis observations of the 2018 mars global dust storm," *Journal of Geophysical Research: Planets*, vol. 124, no. 11, pp. 2929–2944, 2019.

[221] S. L. England, G. Liu, P. Withers, E. Yiğit, D. Lo, S. Jain, N. M. Schneider, J. Deighan, W. E. McClintock, P. R. Mahaffy, M. Elrod, M. Benna, and B. M. Jakosky, "Simultaneous observations of atmospheric tides from combined in situ and remote observations at mars from the maven spacecraft," *Journal of Geophysical Research: Planets*, vol. 121, no. 4, pp. 594–607, 2016.

[222] L. Montabone, A. Spiga, D. M. Kass, A. Kleinböhl, F. Forget, and E. Millour, "Martian year 34 column dust climatology from mars climate sounder observations: Reconstructed maps and model simulations," *Journal of Geophysical Research: Planets*, vol. 125, no. 8, p. e2019JE006111, 2020.

[223] N. Gupta, N. Venkateswara Rao, and U. R. Kadhane, "Dawn-dusk asymmetries in the martian upper atmosphere," *Journal of Geophysical Research: Planets*, vol. 124, no. 12, pp. 3219–3230, 2019.

[224] D. Kass, J. Schofield, A. Kleinböhl, D. McCleese, N. Heavens, J. Shirley, and L. Steele, "Mars climate sounder observation of mars' 2018 global dust storm," *Geophysical Research Letters*, vol. 47, 12 2020. [Online]. Available: https://doi.org/10.1029/2019GL083931

[225] N. G. Heavens, D. M. Kass, and J. H. Shirley, "Dusty deep convection in the mars year 34 planet-encircling dust event," *Journal of Geophysical Research: Planets*, vol. 124, no. 11, pp. 2863–2892, 2019. [Online]. Available: https://doi.org/10.1029/2019JE006110

[226] J.-S. Wang and E. Nielsen, "Wavelike structures in the martian topside ionosphere observed by mars global surveyor," *Journal of Geophysical Research: Planets*, vol. 108, no. E7, 2003. [Online]. Available: https://doi.org/10.1029/2003JE002078

[227] S. Bougher, P.-L. Blelly, M. Combi, J. Fox, I. Müller-Wodarg, A. Ridley, and R. Roble, "Neutral upper atmosphere and ionosphere modeling," *Space Sci. Rev.*, vol. 139, pp. 107–141, 08 2008.

[228] R. Cageao and R. Kerr, "Global distribution of helium in the upper atmosphere during solar minimum," *Planetary and Space Science*, vol. 32, no. 12, pp. 1523–1529, 1984.

[229] F. S. Johnson and B. Gottlieb, "Eddy mixing and circulation at ionospheric levels," *Planetary and Space Science*, vol. 18, no. 12, pp. 1707–1718, 1970. [Online]. Available: https://doi.org/10.1016/0032-0633(70)90004-8

[230] C. A. Reber and P. B. Hays, "Thermospheric wind effects on the distribution of helium and argon in the earth's upper atmosphere," *Journal of Geophysical Research (1896-1977)*, vol. 78, no. 16, pp. 2977–2991, 1973. [Online]. Available: https://doi.org/10.1029/JA078i016p02977

[231] V. A. Krasnopolsky, S. Bowyer, S. Chakrabarti, G. R. Gladstone, and J. S. McDonald, "First measurement of helium on mars: implications for the problem of radiogenic gases on the terrestrial planets," *Icarus*, vol. 109, no. 2, pp. 337–351, 1994. [Online]. Available: https://doi.org/10.1006/icar.1994.1098

[232] K. Roeten, S. W. Bougher, E. Yiğit, A. S. Medvedev, M. Benna, and Y. Lee, "Modeling the impact of gravity waves on the thermosphere of Mars with a whole atmosphere gravity wave parameterization in the Mars Global Ionosphere-Thermosphere Model," in *AGU Fall Meeting Abstracts*, vol. 2020, Dec. 2020, pp. P080–0006.

[233] E. K. Sutton, J. P. Thayer, W. Wang, S. C. Solomon, X. Liu, and B. T. Foster, "A self-consistent model of helium in the thermosphere," *Journal of Geophysical Research: Space Physics*, vol. 120, no. 8, pp. 6884–6900, 2015.

[234] S. W. Stone, R. V. Yelle, M. Benna, M. K. Elrod, and P. R. Mahaffy, "Neutral composition and horizontal variations of the martian upper atmosphere from maven ngims," *Journal of Geophysical Research: Planets*, vol. 127, no. 6, p. e2021JE007085, 2022. [Online]. Available: https://agupubs.onlinelibrary.wiley.com/doi/abs/10.1029/2021JE007085

[235] K. Masunaga, K. Yoshioka, M. S. Chaffin, J. Deighan, S. K. Jain, N. M. Schneider, T. Kimura, F. Tsuchiya, G. Murakami, A. Yamazaki, N. Terada, and I. Yoshikawa, "Martian oxygen and hydrogen upper atmospheres responding to solar and dust storm drivers: Hisaki space telescope observations," *Journal of Geophysical Research: Planets*, vol. 125, no. 12, p. e2020JE006500, 2020. [Online]. Available: https://doi.org/10.1029/2020JE006500

[236] T. Owen, J. P. Maillard, C. de Bergh, and B. L. Lutz, "Deuterium on mars: The abundance of hdo and the value of d/h," *Science*, vol. 240, no. 4860, pp. 1767–1767, 1988. [Online]. Available: https://www.science.org/doi/abs/10.1126/science.240.4860.1767

[237] C. Webster, P. Mahaffy, G. Flesch, P. Niles, J. Jones, L. Leshin, S. Atreya, J. Stern, L. Christensen, T. Owen, H. Franz, R. Pepin, A. Steele, C. Achilles, C. Agard, J. Verdasca, R. Anderson, R. Anderson, D. Archer, and M.-P. Zorzano, "Isotope ratios of h, c, and o in co2 and h2o of the martian atmosphere," *Science*, vol. 341, pp. 260–263, 07 2013.

[238] J. Alday, C. Wilson, P. Irwin, K. Olsen, L. Baggio, F. Montmessin, A. Trokhimovskiy, O. Korablev, A. Fedorova, D. Belyaev, A. Grigoriev, A. Patrakeev, and A. Shakun, "Oxygen isotopic ratios in Martian water vapour observed by ACS MIR on board the ExoMars Trace Gas Orbiter," *Astronomy & Astrophysics*, vol. 630, p. A91, Oct. 2019.

List of Publications

1. Gupta, N., Venkateswara Rao, N., and Kadhane, U. R. (2019). Dawn-dusk asymmetries in the Martian upper atmosphere Journal of Geophysical Research: Planets, 124. https://doi.org/10.1029/2019JE006151

2. Venkateswara Rao, N., Gupta, N., and Kadhane, U. R. (2020). Enhanced densities in the Martian thermosphere associated with the 2018 planet-encircling dust event: Results from MENCA/MOM and NGIMS/MAVEN. Journal of Geophysical Research: Planets, 125, e2020JE006430. https://doi.org/10.1029/2020JE006430

3. Gupta, N., Rao, N. V., Bougher, S., and Elrod, M. K. (2021). Latitudinal and Seasonal Asymmetries of the Helium Bulge in the Martian Upper Atmosphere. Journal of Geophysical Research: Planets, 126, E2021JE006976. https://doi.org/10.1029/2021J-E006976

4. Gupta, Neha and Venkateswara Rao, N.(2022). Latitudinal, Local time and Dust Storm induced variability of Mixing Ratios in the Thermosphere of Mars, Planetary and Space Science *(under review)*